Large-scale atom manipulation on an ionic surface and its prospects

Kalff, Floris

DOI
10.4233/uuid:3d3eb1f4-c067-44f6-9c42-2acc988f6a63

Publication date
2018

Document Version
Final published version

Citation (APA)
Kalff, F. (2018). *Large-scale atom manipulation on an ionic surface and its prospects*. [Dissertation (TU Delft), Delft University of Technology]. https://doi.org/10.4233/uuid:3d3eb1f4-c067-44f6-9c42-2acc988f6a63

LARGE-SCALE ATOM MANIPULATION ON AN IONIC SURFACE AND ITS PROSPECTS

LARGE-SCALE ATOM MANIPULATION ON AN IONIC SURFACE AND ITS PROSPECTS

Proefschrift

ter verkrijging van de graad van doctor
aan de Technische Universiteit Delft,
op gezag van de Rector Magnificus prof. dr. ir. T.H.J.J. van der Hagen,
voorzitter van het College voor Promoties,
in het openbaar te verdedigen op
woensdag 31 oktober 2018 om 10:00 uur

door

Floris Eduard KALFF

doctorandus in de natuurkunde, Universiteit Leiden, Nederland,
geboren te 's-Gravenhage, Nederland.

Dit proefschrift is goedgekeurd door de promotoren.

Samenstelling promotiecommissie:

Rector Magnificus	voorzitter
Prof. dr. A.F. Otte	Technische Universiteit Delft, promotor
Prof. dr. ir. H.S.J. van der Zant	Technische Universiteit Delft, promotor
Onafhankelijke leden:	
Prof. dr. L. Kuipers	Technische Universiteit Delft
Prof. dr. P. Liljeroth	Aalto-yliopisto, Finland
Prof. dr. J. Repp	Universität Regensburg, Duitsland
Prof. dr. P.M. Koenraad	Technische Universiteit Eindhoven
Dr. I. Swart	Universiteit Utrecht
Prof. dr. Y.V. Nazarov	Technische Universiteit Delft, reservelid

Keywords: Scanning tunnelling microscope, tunnelling spectroscopy, atom manipulation

Printed by: Gildeprint – Enschede

Front & back: An atomic memory with atomic bits, engineered by vacancy manipulation in the chlorinated copper (100) surface by STM, with atomic vacancies representing bits. Design by H.C. Kalff and A.F. Otte.

Casimir PhD series, Delft-Leiden 2018-35

ISBN 978-90-8593-364-9

An electronic version of this dissertation is available at
http://repository.tudelft.nl/.

Aan Mara. Aan mijn ouders.

CONTENTS

1

INTRODUCTION

EVER since the beginning of history, people have been interested in unravelling the inner workings of nature. In ancient times, the four elements fire, air, water, and earth – and sometimes aether – were thought to make up all matter, and remained the building blocks until the Renaissance. At the end of the fifth century BCE, the Greek Democritus first coined the term ατομος, or a-tomos, meaning in-divisible, to denote the smallest particle of a substance with the same properties as the bulk. From Democritus' shapes dependent on the substance's properties (e.g. sharp and pointy for salt atoms, smooth and slippery for water atoms), Plato's geometric shapes (polyhedral shapes for the four elements), and Descartes' vortices of matter, the atomic theories finally reached maturity from the 18^{th} century; from Dalton's proportional model of the atom via Rutherford's planetary and Bohr's energy level model to the current quantum mechanical understanding.

After the invention of the optical microscope in the 1600s and the development of the electron microscope from the 1930s, it was the invention of the scanning tunnelling microscope (STM) that truly opened the door to the direct observation of individual atoms. After Binnig and Rohrer had developed the STM in the early 1980s [1, 2], the benefit was quickly recognised, and it earned them the Nobel prize in physics in 1986, an unusually short time after the discovery [3]. In the three decades since, the field of scanning probe microscopy grew to encompass many tools and techniques, the most commonly known of which is derived from the STM: the atomic force microscope (AFM) [4, 5].

In Feynman's famous 1959 lecture 'There's plenty of room at the bottom' [6], he predicted – or more accurately: put forward a challenge, one that we are more than eager to accept – that at some point, it should be possible to "arrange the atoms the way we want", thus not just observing nature's building blocks, but also designing new materials by engineering the atoms in novel, previously undreamed-of ways.

In our case – solid-state research on the atomic scale – a scanning probe microscope is the method of choice. The common denominator of all scanning probe microscopy techniques is the needle that scans over the surface of the object of interest: the scanning probe. This needle typically feels the profile in some way and constructs a topography

image from it with atomic resolution. In the case of the AFM, it is the atomic forces between sample and tip that cause the needle to deflect, generating a height map [4, 7]. This has been used to measure the bonds in a pentacene molecule, enabling effectively a sub-atomic resolution [8]. The scanning tunnelling microscope – our method of choice – uses a small current that can tunnel through the vacuum between tip and sample, even when they are not in contact. This tunnel current is strongly dependent on the needle height, every 1 Å tip height increase leads to roughly a factor ten decrease in current, making it a very good feedback parameter for maintaining a constant distance from the sample. As the sample needs to conduct current, any topography image is a convolution of the local conductivity and tip-sample distance. There are many more scanning probe techniques that can measure properties of the sample in a local manner, such as the contact potential with Kelvin probe force microscopy [9–11], the magnetic flux density with scanning SQUID microscopy [12], and even single spins with magnetic resonance force microscopy, a technique combining MRI and AFM [13–15].

When it becomes possible to discern individual atoms by probing them with a sharp needle, the next step is to move them, by dragging, pushing, or even picking them up. Atoms have been moved around on surfaces for more than 25 years [16], allowing the study of the single atom in many different ways. A particularly fruitful research direction is that of studying the magnetic properties of atoms [17, 18]. Magnetism originates in the spin magnetic moments of the electrons in the atomic shells. When a magnetic atom is adsorbed on a metal, the orbitals hybridize with the substrate, resulting in very short lifetimes of the magnetic states. Only when a decoupling layer is placed between the metal bulk and the magnetic atom, does the lifetime become long enough to measure with current techniques.

Many groups are working towards techniques at the atomic scale, where using and adjusting the material properties according to their liking at these scales is essential. For this, it is important to understand the physics surrounding single atoms and ensembles of atoms and molecules in varying environments. The insulating Cu_2N/Cu(100) substrate, a monolayer of covalently bound nitrogen atoms, has been used extensively for coupling individual spins into chains, as measured by the magnetic spin excitations [19–22]. Other decoupling layers such as MgO/Ag(100) [23, 24] or a NaCl bilayer on Cu(111) [25] also provide good substrates for the study of individual atoms. Magnetic adatoms, such as iron, manganese and cobalt, have a preferred direction of the magnetic moment – magnetic anisotropy – which is influenced by its surroundings, such as the direct geometry of neighbouring atoms in the lattice, island boundaries, or nearby magnetic adatoms [20, 24, 26–28]. The anisotropy can be applied to construct stable magnetic bits and transistors [29–32], chains with the tunnelling through certain orbitals suppressed [33]; chains where the spins form waves [34], or are about to go through a quantum phase transition [35]. Recently, a single holmium atom on MgO/Ag(100) was found to have magnetic remanance, i.e. it behaves as a classical magnet that can remain magnetised without external field [36], which can then be used as a magnetic bit [37].

Some of these states can be probed by new techniques; with spin-polarised STM, spins in the parallel and anti-parallel directions with respect to the spin-polarised tip can be distinguished, as part of the tunnel current is blocked in the anti-parallel configuration [38]. Another promising new technique is that of electron spin resonance (ESR),

similar to nuclear magnetic resonance (NMR, or MRI when used in hospital scanners), where a radio-frequent wave incites an inelastic excitation in a magnetic atom, thus allowing read-out of the spin state with a spin-polarised tip [39–41].

Feynman's words thus seem to come true: in this time and age, our capabilities of tinkering with materials are growing fast, and by manipulating individual atoms to do our bidding, many new effects and interactions are discovered and studied, leading to new exciting ways of doing physics.

THESIS OUTLINE

This thesis presents a new technique for large-scale atom manipulation, on a chlorine terminated copper substrate that is a promising new playground for novel applications. Chapter 2 introduces the scanning tunnelling microscope (STM), and the sample preparation procedures. The manipulation of vacancies – missing chlorine atoms from the $Cu_2Cl/Cu(100)$ layer – is developed, as well as its automation. We describe the process of scanning tunnelling spectroscopy (STS) in order to measure the local density of states (LDOS). The stability of the Cu_2Cl surface up to higher temperatures is discussed, and we study the vacancy-vacancy interactions.

In Chapter 3, the opportunities for large-scale vacancy manipulation are demonstrated by the autonomous construction of a data storage of a full kilobyte in size. Using a procedure of scanning, image recognition, and guiding the vacancies to their destinations with a path-finding algorithm, blocks of 64 bits are constructed autonomously, with a chlorine-vacancy pair designating each single bit. Three different texts were written in this memory to demonstrate its rewritability.

Chapter 4 details about other structures that can be made using this vacancy manipulation technique. Local scanning tunnelling spectroscopy measurements are done on one- and two-dimensional arrays of varying densities and sizes, revealing the emergence of quasiparticle bands. Standing Bloch waves are found in some structures, where the dispersion can be tuned by the vacancy density.

The tight-binding coupling between individual vacancies is discussed in Chapter 5, where we couple vacancies together in order to simulate polyacene molecules. These molecules made from benzene-rings are predicted to have a band gap that closes and reopens alternately with increasing chain length. We run some tight-binding simulations to predict the gap oscillation with the couplings in our system, and compare them to STS measurements of our artificial molecules of varying lengths.

Chapter 6 reports a method to measure the local electric field of the sample, by making use of a quantum dot on the STM tip. We compare the response for various local structures that have been built with vacancy manipulation, and correlate them with electric field calculations of these structures.

In Chapter 7, the possibility for using Cu_2Cl as a decoupling layer for magnetic adatoms is explored, and three kinds of transition metals have been evaporated. The expectation is that, like the well-known and much-used Cu_2N substrate, it is also insulating enough to increase the lifetime of magnetic states in adatom structures. Silver, nickel and iron atoms have been deposited on the surface, and their differential conductance spectra are examined for signs of inelastic excitations, at low temperatures and with magnetic fields of up to 2 T in-plane and 9 T out-of-plane.

2

SCANNING TUNNELLING MICROSCOPY ON A CHLORINE RECONSTRUCTED COPPER (100) SURFACE

Since the first demonstration of atom manipulation, more than 25 years ago [16], the preferred approach for assembling atomic arrangements has been the lateral positioning of atoms or molecules evaporated onto a flat metal surface, most notably the (111) crystal surface of copper [29, 44, 45]. Although ideal for experiments comprising up to several hundreds of constituents, the absence of a large-scale defect-free grid on this surface, where adatoms and surface grid are detectable at the same time, prohibits the construction of architectures involving correlated lattice-placement of atoms over larger distances than a few nanometres. Moreover, thermal motion of the adatoms restricts the technique to temperatures below 10 K. As we demonstrate in the following, we find that manipulation of missing atoms in a surface (vacancies) [46–48], as opposed to additional atoms on top, permits a profound advance in our capability to build functional devices on the atomic scale.

We take advantage of the self-assembly of chlorine atoms on the Cu(100) surface [49–55], forming a flat two-dimensional lattice with several convenient properties. First, it provides large areas of a perfect template grid, with a controllable coverage of vacancies. Second, the chlorine lattice remains stable up to a large density of vacancies and up to a relatively high temperature (77 K). Third, we developed a technique to manipulate the precise location of the vacancies by STM with a very high level of control (and without the need to pick up atoms with the tip; i.e. vertical atom manipulation).

Parts of this chapter have been published in Nature Nanotechnology **11**, 926-929 (2016) [42] and SciPost Physics **2**, 020 (2017) [43].

2

In this chapter, we discuss our experimental techniques and the development of the $Cu_2Cl/Cu(100)$ surface. All measurements in this thesis have been performed by the scanning tunnelling microscope. We will expand upon the working principles of the STM, the existing methods of sample preparation, and describe the process of preparing a clean chlorine terminated copper surface. We developed a way to manipulate vacancies in this surface in a controllable, reproducible manner, and investigate their positions on the surface and the interactions between vacancies.

2.1. The Scanning Tunnelling Microscope

The scanning tunnelling microscope (STM), invented in 1981 by Binnig and Rohrer [1, 56, 57], combines the inverse piezoelectric effect with the process of quantum tunnelling to image surfaces down to the atomic level. The inverse piezoelectric effect allows one to control the position of a very sharp needle in a precise way by the deformation a piezoelectric material undergoes when a voltage is applied to it. This brings a metallic tip in the vicinity of a conducting sample, and when it is close enough, less then a nanometre away, the probability for electrons to tunnel from the tip, through the vacuum, and into the sample becomes non-zero. When a bias voltage is applied, a tunnel current is realized over the junction, with an exponential dependence on the tip-sample distance, which can go from several picoamperes to microamperes and more.

Typically, the height of the STM tip is feedback-controlled such that the tunnel current is constant. This means that when the tip is scanned horizontally over the sample, a height map of the surface is generated, with sub-atomic spatial resolution. This topography, however, is a convolution of both the physical height of the surface and the local density of states (LDOS), as that is the number of electron states at a specific spot in the surface at a certain energy. This explains why adatoms or insulating structures on metals (such as Cu_2N on Cu(100)) sometimes appear lower in the topography: their conductance is less than the surrounding metal, and they thus appear as depressions [58, 59].

For the results presented in this thesis, two commercial low-temperature ultra-high vacuum STM set-ups were used: a Unisoku USM-1300S ^{3}He system, and a SPECS JT-SPM system with Tyto SPM-head, both shown in Figure 2.1. Both systems have a number of vacuum chambers: a load lock for loading samples without having to vent the rest of the system, a preparation chamber, the STM chamber, and in case of the Unisoku system, an exchange chamber where the metal is evaporated. The systems are under ultra-high vacuum, with two ion getter pumps operating continually, and an optional turbo pump during sample preparation, so that the base pressure is below $5 \cdot 10^{-10}$ mbar. In the Unisoku system, the microscope is down in the cryostat, which is cooled from liquid helium temperatures down to a stable 1.5 K. The base temperature, 330 mK, can be reached by recondensing 20 ℓ (when at atmospheric conditions) of ^{3}He for a maximum duration of 24 hours. The SPECS system utilizes a Joule-Thomson process with ^{4}He to cool down to 1.2 K, with the microscope head thermally anchored to, but not inside, the liquid helium cryostat.

Tip and sample are vertically aligned, with the tip at the bottom, and the sample looking down from the top. The Unisoku microscope is enclosed in a vertical solenoid that can supply a magnetic field of 9 T in the z-direction perpendicular to the surface

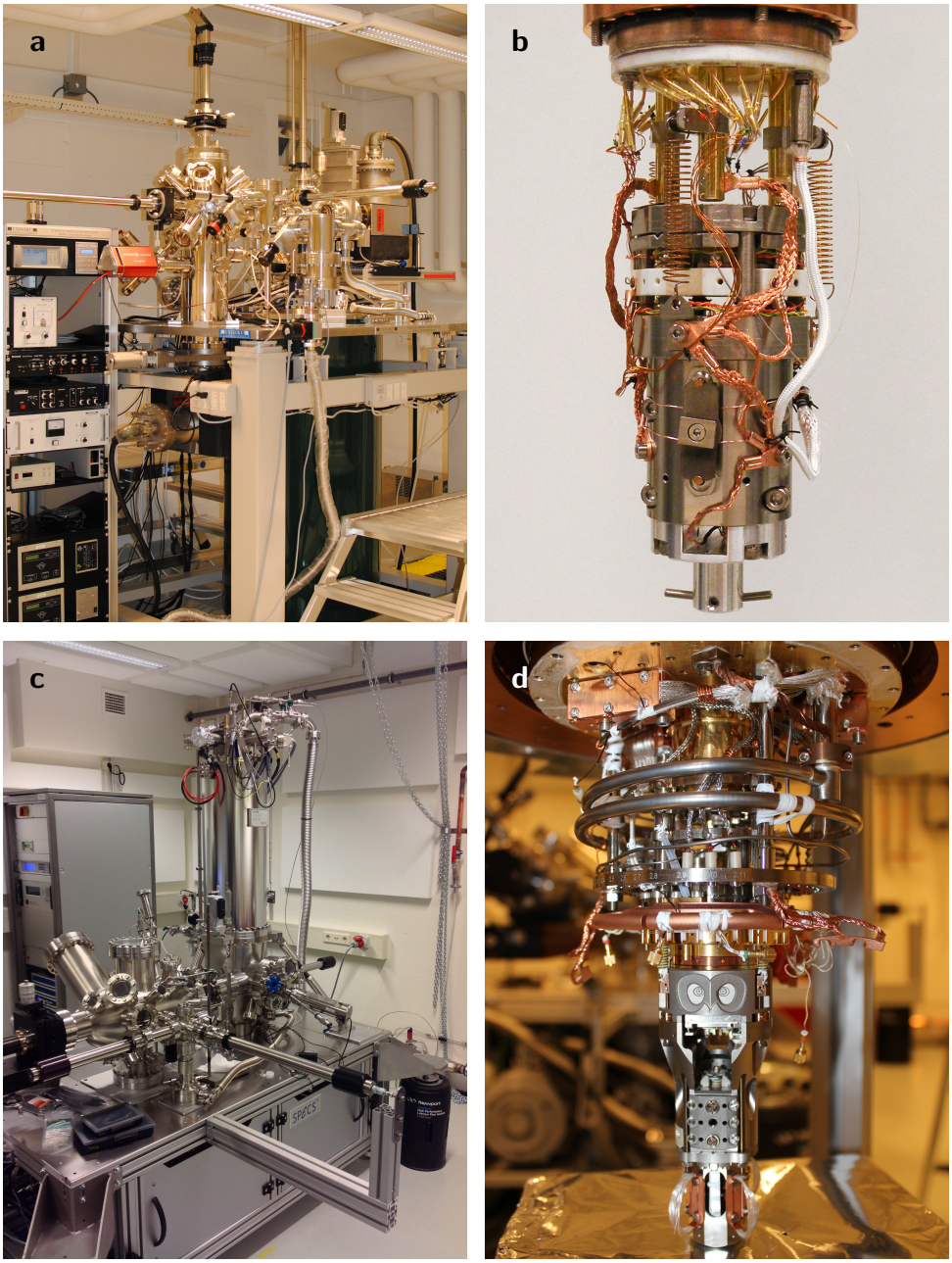

Figure 2.1: **Two low-temperature ultra-high vacuum STM set-ups. a**, Unisoku USM-1300S ^{3}He system, with three ultra-high vacuum chambers above a vibration damping table, and a 130 l liquid ^{4}He dewar; and **b**, its microscope head, located at the bottom of the green cryostat. **c**, SPECS JT-SPM system with three ultra-high vacuum chambers on the table, with a cryostat for 10 ℓ ^{4}He and 20 ℓ N_2; and **d**, the Tyto SPM head, equipped for both AFM and STM tips.

plane; a 2 T split-coil can supply a horizontal field in the x-direction. The maximum field for samples in the SPECS microscope is 3 T, in only the z-direction. The microscope there is enclosed in a split-coil magnet, for optical access and fast sample transfer possibilities.

The preparation chambers and sample holders are designed such that the back of the sample can be heated with e-beam heating by a filament. The chambers are also equipped with a bottle of Ar gas and an ion gun for sputtering, a mass spectrometer to verify the purity of the gases, an evaporator for various metals, and in the case of the Unisoku microscope, a low-energy electron diffraction (LEED) device for verifying the crystalline quality of the sample during and after the preparation.

2.2. SAMPLE PREPARATION

For the research presented in this thesis, we developed a recipe for the preparation of a single layer – or less – of chlorine atoms self-assembled on the surface of a copper crystal. The metal has 6N purity (99.9999 % Cu), is cleaved along the (100) plane with ~0.1° precision, and is polished to a roughness of 0.05 µm. Prior to chlorine evaporation, the surface is cleaned by bombarding it with inert argon ions, removing a few layers of atoms and any contaminants. After the sputtering, the crystal is annealed in order to smooth the surface to atomic flatness. These two steps are then repeated a number of times with varying durations, until the bare copper surface has as few contaminations and steps as possible.

During the sputtering of argon ions, a dose of Ar gas (~$1.3{\cdot}10^{-5}$ mbar) is let into the preparation chamber, where a filament ionizes the atoms. The Ar^+ ions are then accelerated with a high voltage, typically 500 or 1000 V, towards the sample stage, which is kept at ground.

Assuming a beam profile with a Gaussian distribution that is 5 cm wide (at 95 % or 4σ), with the sample ($4.2{\times}5$ mm^2) positioned in the middle of the beam, we can assume the crystal to catch 1/8 of the incident Ar^+ ions, i.e. 1/8 of the ion current. Every µA of ion current corresponds to a flux of $6{\cdot}10^{12}$ Ar^+/s, so every second, $7.5{\cdot}10^{11}$ Ar^+ ions will reach the crystal. With the conventional unit cell of Cu(100) being (~0.36 nm)^2 in size, with two copper atoms per unit cell, there will be one argon ion per copper atom on the surface every 432 seconds. The sputtering yield, i.e. the number of evacuated atoms per incident ion, of Ar^+ ions on Cu surfaces is ~2 for 500 V and ~3 for 1 kV, in normal incidence [60–62]. We normally keep the Ar pressure in the preparation chamber constant, where the ion current typically is 1-2 µA. That means that roughly every 2-3 minutes, an entire layer of Cu atoms gets removed from the surface.

After sputtering, the surface is rough and needs to be annealed in order to regain an atomically flat surface [58, 62–64]. The sample is annealed at 500-700 °C for 5-20 minutes by an electron beam heating filament mounted in the back of the sample holder. The temperature is verified by the e-beam current (~mA at 1 kV) or by a PID feedback loop controlled by a pyrometer.

The Ar sputtering and annealing cycles are repeated a number of times for varying, decreasing times, typically from 20 down to 5 minutes each, in order to get the best results. An example of a clean copper surface can be seen in Figure 2.2a.

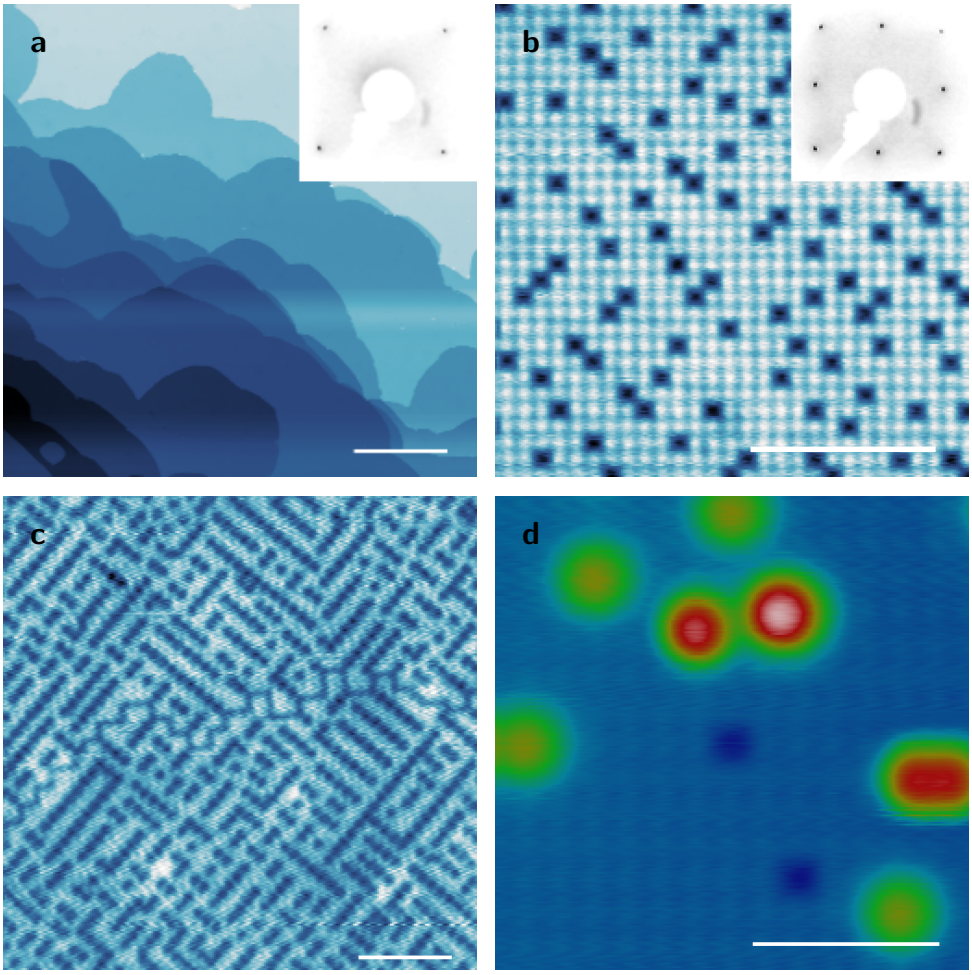

Figure 2.2: Copper surfaces, imaged with STM. **a**, A bare copper surface, scale bar 100 nm. Inset is a LEED image at 85 eV of a Cu(100) surface, with the square symmetry evidenced by the four spots in a square pattern. **b**, Vacancies in a chlorine reconstructed Cu(100) surface, with 89 % Cl coverage, scale bar is 4 nm. Inset is a LEED image at 85 eV of a Cu_2Cl surface in the c(2 × 2)R45° reconstruction, manifesting as the four extra spots at $1/\sqrt{2}$ times the distance of, and rotated 45° with respect to, the four spots of the bare copper. **c**, Labyrinth pattern in surface with 70 % Cl coverage, showing a domain wall, scale bar is 4 nm. **d**, Ag atoms adsorbed on $Cu_2Cl/Cu(100)$, in various positions, scale bar is 2 nm.

2.3. THE SUBSTRATE $Cu_2Cl/Cu(100)$

The chlorinated copper surface was prepared in ultra-high vacuum through thermal evaporation of anhydrous $CuCl_2$ powder from a quartz crucible heated to 300 °C onto a clean Cu(100) crystal surface. The crystal was pre-heated to 100-150 °C before $CuCl_2$ deposition for ~12 min and kept at this temperature during the deposition and the 10 min post-anneal. This resulted in the formation of a square c(2×2) reconstruction of Cl atoms with a lattice constant a of 0.36 nm. We will denote this surface as $Cu_2Cl/Cu(100)$,

because of the ratio between Cu and Cl atoms in the top layer, which form an ionic bond [53]. Note that this stoichiometric description is only valid for the two-dimensional surface layer, as is also common for the similar Cu_2N substrate [33, 34].

The Cl coverage (and therefore the vacancy coverage x) depends on the duration of evaporation. For most of the results presented in Chapters 3 and 4 we used an evaporation time of 210 s, resulting in a vacancy coverage of $x = 0.115 \pm 0.004$, where the error is based on the square root of the total number of vacancies counted. Different sample preparations with the same settings gave $x = 0.039 \pm 0.004$ for $\tau = 210$ s, $x = 0.038 \pm 0.004$ for $\tau = 225$ s and $x = 0.17 \pm 0.05$ for $\tau = 240$ s. To properly study the relation between Cl coverage and evaporation time, one would need a separate means of measuring the evaporation rate (our STM system is not equipped with this). Although annealing the sample during and after the Cl deposition was initially deemed necessary, it was later found that evaporation without pre- and post-annealing also gave clean chlorine reconstructed surfaces.

We verified the coverage with low-energy electron diffraction (LEED), and by counting atoms on the topography images taken by the STM. See Figure 2.2b,c for surfaces with chlorine coverages of 0.89 and 0.7, respectively.

When imaged by STM, missing chlorine atoms – vacancies – are resolved as square depressions ~20–30 pm deep (Figure 2.4). According to density functional theory (DFT) calculations (see Section 2.7), a Cl atom has to overcome an energy barrier of $\Delta = 0.3$ eV in order to swap places with a neighbouring vacancy (Figure 2.4a,b). As a result, the surface is resilient to tunnelling currents of up to 2 μA when imaged at positive sample voltages of ~200 mV or lower.

The Cl-terminated Cu(100) surface seems very inert. The sample used for most of the experiments (with $x = 0.115$) has been in our STM for more than seven months (at a pressure $p < 10^{-10}$ mbar) without any noticeable degeneration, both in surface appearance and reliability of vacancy manipulation. This suggests that less stringent conditions than ultra-high vacuum may be acceptable.

The chlorinated Cu(100) surface has two possible phases, with domain walls running along the Cl c(2×2) unit cell directions, see Figure 2.3. Other copper surfaces can also be chlorinated, where the Cl reconstruction can be more complex. The Cu(111) surface allows several reconstructions [65], of which the $(\sqrt{3} \times \sqrt{3})$R30° reconstruction can also harbour vacancies and act as a substrate for adatoms [66]. Other halogens, such as iodine and bromine, can also be chemisorbed at a copper surface, and other metal crystals, like silver and gold, can be chlorinated as well [50–52, 65, 67–75]; so examples of these might be suitable candidates for the manipulation of vacancies, or used as decoupling layers for magnetic atoms and structures.

2.4. METAL EVAPORATION

For experiments with adatoms, such as described in Chapter 7, metal atoms can be deposited on the surface, after the chlorine has been evaporated onto the copper crystal. This is done by heating a crucible of metal powder to near the melting point and exposing the sample to it. Ideally, this occurs while the sample is at low temperature, to prevent the atoms from clustering. This is not possible in the 330 mK STM, because the microscope with the sample is located down in the bottom of the cryostat, with no

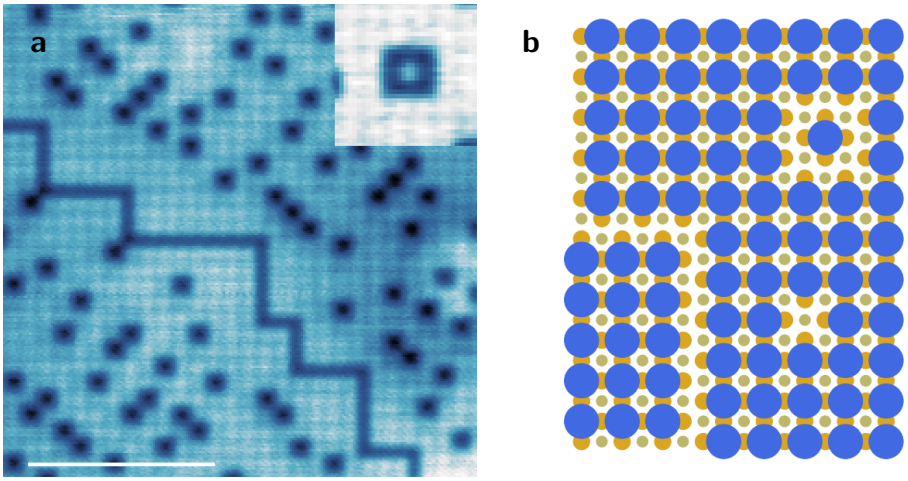

Figure 2.3: **Domain walls in the chlorinated copper surface.** Scale bars are 4 nm. **a**, Topography image of a domain wall with a vacancy density $x = 15$ %; and **b**, a schematic representation of the two possible phases, showing a domain wall, a single vacancy, and a single phase-shifted chlorine atom (inset of (**a**). STM image taken at 500 mV, 1.650 nA. Schematic shows Cl atoms (blue), Cu atoms in the top layer (orange), and Cu atoms in the second layer (khaki).

direct access to the metal evaporator. When the sample is at 1.5 K long enough, we extract it from the STM to the exchange chamber, after pre-cooling the transfer stick on the heat shields, where the sample is exposed to the beam of evaporated metal for ~10 seconds, and reinsert it in the STM. The exchange chamber is at room temperature, with the pressure inside at $\sim 2 \cdot 10^{-10}$ mbar before evaporation. When the sample is reinserted in the STM, the temperature sensor rises to ~30 K, which suggests that, together with pre-cooling the sample transfer stick, the sample remains cold enough that the evaporated atoms can still be individually identified. See Figure 2.2d for an example of silver atoms evaporated on $Cu_2Cl/Cu(100)$.

2.5. ATOM AND VACANCY MANIPULATION

Atoms lying atop surfaces, adatoms, have been manipulated and arranged in all kind of structures, such as characters [16], quantum corrals [44], magnetic bits [31], spin chains [34, 35, 76] and more [20, 21, 26, 27, 29].

The most common way of moving atoms is by lateral atom manipulation, where the atoms lie on a bare metal surface, such as Xe on Ni(110) [16], Fe on Cu(111) [44], and Fe on Pt(111) [77]. The tip is brought close to the atoms, and due to the Van der Waals attraction, the atom falls in the combined potential well of tip and sample, after which the tip can be moved laterally, dragging the atom along.

Another way of moving atoms is not by horizontal, as above, but by vertical atom manipulation, which is the preferred way for adatoms on substrates such as $Cu_2N/Cu(100)$ [19, 26, 78]. In this case, by bringing the tip close to the the charged adsorbate atom and applying a voltage pulse, the atom is transferred from its binding site to the tip [79, 80].

The tip is moved to another location, where the atom is now removed from the apex in a similar procedure, after which it binds to the surface. The atom must be charged, so the voltage pulse overcomes the potential barrier from surface to apex position, thus picking it up. For drop-off, the Van der Waals attraction alone is often enough to transfer the atom to the sample, where only a small (or no) voltage pulse is required. In order to coerce the adatom to its desired position, another voltage pulse in that direction is sometimes needed [58, 81, 82].

It is also possible to move the vacancies in a surface by applying voltage pulses to the substrate [46, 48], or to create these vacancies in a thin salt layer [47, 83, 84].

We developed a different technique, a lateral vacancy manipulation that we believe uses local Joule heating of the surface to enable a neighbouring chlorine atom to move into the vacancy. We found this to be very controllable and reliable, as the entire manipulation procedure is executed with the feedback on.

As shown in Figure 2.4, vacancies (missing chlorine atoms) can be moved by injecting a current of 1.0 ± 0.5 μA (error represents variations from tip to tip in the exact shape of the STM tip apex) at +500 mV sample voltage at a position ~$0.4a$ along the way from the centre of the vacancy to the centre of the neighbouring Cl atom at the desired location. The STM feedback is kept switched on throughout the manipulation procedure. Although several attempts may be required to make a vacancy move, the directional reliability (that is, how often a vacancy moves in the desired direction once it moves) can be in excess of 99 %, depending on the tip shape. Controlled vacancy movement is limited to the (±1,0) and (0,±1) directions on the square Cl grid. Diagonal moves (for example, in the (1,1) direction) were found to occur sporadically, but could not be induced controllably. Any move larger than a single lattice spacing would consist of multiple chlorine atoms moving sequentially: each hopping only a single step, but the vacancy would appear to have moved a larger distance.

Occasionally, when using substantially larger set-point current and/or bias voltage during manipulation, multiple vacancies are found to be rearranged several nanometres away from the tip position. The distance travelled by a vacancy can in those instances also be larger than a single unit cell. However, it is easy to stay well below these values so that only the intended vacancy moves.

Vertical manipulation of Cl atoms is on occasion possible, by using a slightly larger set-point current than for lateral manipulation. Picking up an atom leaves a vacancy behind, thus fashioning a sharper tip apex, which greatly enhances the resolution of the topographies. Dropping off the Cl atom was possible by repeating the manipulation procedure at the higher set-point. Although we could not perform this with very high reliability, this is the best way of obtaining the most distinctive topography images, see e.g. Figure 3.3.

We believe that the vacancy manipulation is primarily due to current-induced heating, or Joule heating, which provides sufficient energy for the Cl atom to leave its potential well, as shown in Figure 2.5. Since the success rate of the manipulation is much larger than 50 %, there must be a tip-induced mechanism that breaks the symmetry between the original location of the Cl atom and its destination, causing the latter to be favoured. We do not know the exact nature of this mechanism, but we speculate that it could be electrostatic or Van der Waals interaction, or a combination thereof. The polarity of the

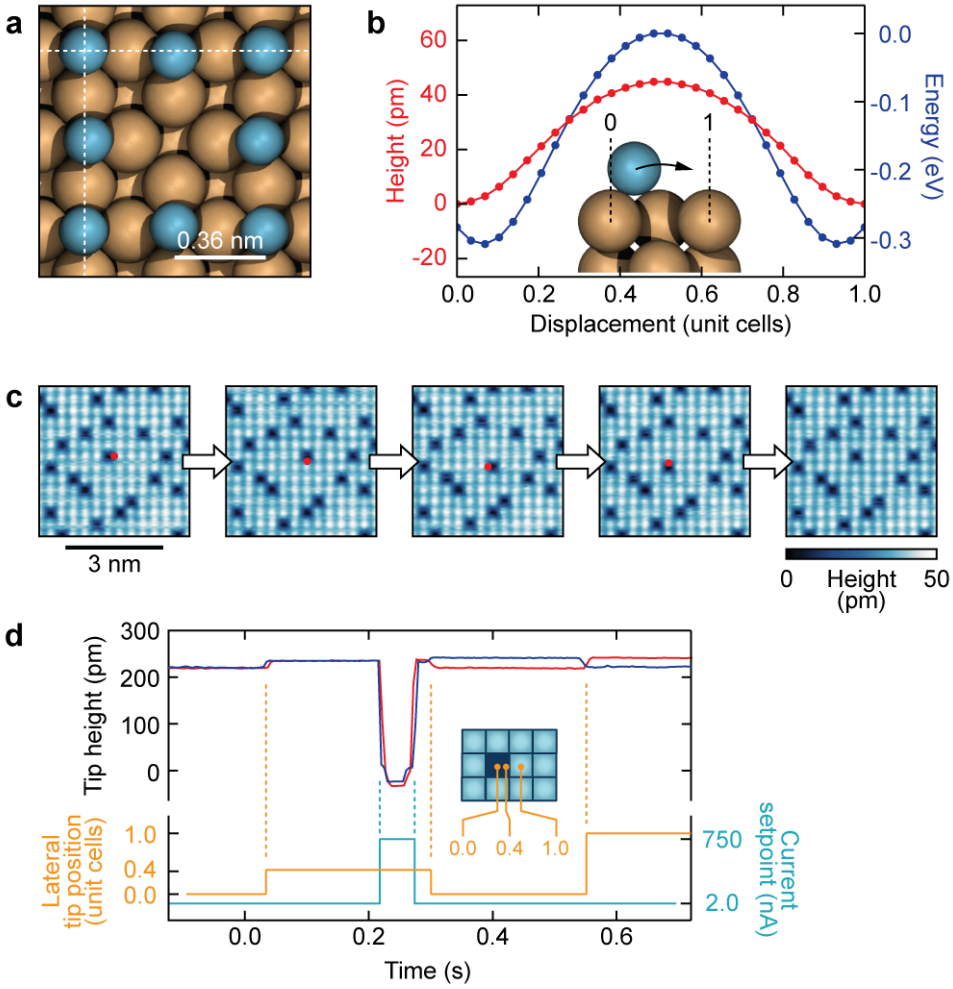

Figure 2.4: **Hopping mechanism of a Cl vacancy on chlorinated Cu(100). a**, Atomic structure around a vacancy, calculated by DFT. Cl atoms (blue) are found to relax slightly towards the centre of the vacancy with respect to their original locations (dashed lines). **b**, DFT calculations provide the height profile and the corresponding potential energy of a Cl atom during a switch. **c**, Consecutive STM images (tunnelling current $I = +2.00$ nA, sample bias voltage $V = +500$ mV, temperature $T = +1.5$ K) of a vacancy being hopped in all four directions. The tip position for each manipulation is designated by a red dot. **d**, Measured tip height during a successful (blue) and an unsuccessful (red) manipulation. Yellow and cyan curves show the lateral tip position (see inset) and applied tunnelling current set-point, respectively. $V = +500$ mV throughout the manipulation. After the manipulation, the tip visits the original location of the Cl atom and the target position. Variations in the tip height between these two positions indicate whether the manipulation has been successful.

voltage used during manipulation (positive on the sample, negative on the tip) excludes an explanation based on a simple Coulomb attraction of the negatively charged Cl atom.

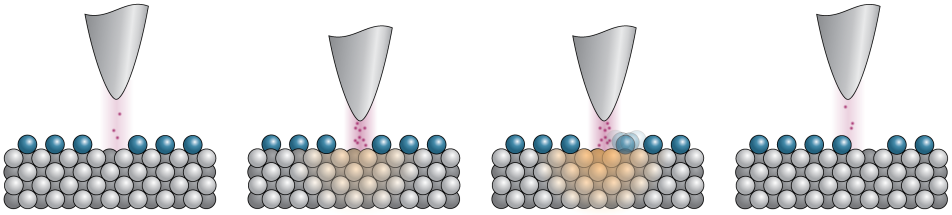

Figure 2.5: **The proposed mechanism for vacancy manipulation: Joule heating.** Left to right: at first, the center of the vacancy is located, and the tip is positioned $0.4a$ in the intended direction; the set-point current is then ramped from 2 nA to 1.0 ± 0.5 μA, at 500 mV, thus bringing the tip closer; this higher current locally heats up the atoms surrounding the tip apex, raising the switching rate; because the tip is not located exactly halfway between vacancy and neighbouring atom, an asymmetric interaction with it causes the atom to jump to the vacancy, thus moving the vacancy in the opposite direction. Afterwards, the current is restored to the initial values.

We point out that we have also observed successful manipulation with a negative sample voltage (using the same tip location), although this was much less reliable.

A possible reason for the large variance in manipulation current between different tips (1.0 ± 0.5 μA), could be the existence of parallel tunnelling paths from the tip apex to other Cl atoms. It is well possible that for a given separation between apex atom and the Cl atom being manipulated, variations in the tip shape will give considerable contributions to the tunnel current from the apex atom to the other three Cl atoms nearby.

2.6. SCANNING TUNNELLING SPECTROSCOPY

Aside from imaging atoms, another powerful technique we employ is scanning tunnelling spectroscopy (STS). While keeping the height of our tip constant, we sweep the bias voltage, and record the current so that we obtain the IV characteristics of our junction. The differential conductance is also recorded, by modulating the bias voltage with a small amplitude, e.g. 10 mV at 916.1 Hz, while the resulting oscillation in the current is demodulated with a lock-in device. This gives the slope of the current as a function of the bias voltage, i.e. the differential conductance $\mathrm{d}I/\mathrm{d}V$, which is a measure for the local density of states (LDOS) [85].

A monolayer of chlorine atoms on Cu(100) exhibits a surface band gap E_g of about 7 eV (see Figure 2.6) as well as a shift in the substrate's work function by 1.25 eV [55], suggesting a significant charge transfer between the substrate and chlorine atoms and formation of the interface dipole moment [86]. Theoretical calculations predict a charge of 0.5 electron accumulated on chlorine atoms and depletion of the density of states (DOS) at the top-most layer of the copper substrate [51]. Other materials with a similarly large surface band gap, e.g. Cu_2N on Cu(100) ($E_g \sim 4$ eV) [87], NaCl bilayers on copper substrates ($E_g \sim 8.5$ eV) [84], and non-polar MgO films on Ag(100) ($E_g \sim 6$ eV) [23], have found applications in studies of elementary excitations in individual molecules and/or adatoms [24, 25, 29, 84]. The insulating monolayers formed on the metal substrates have been shown to have little effect on the valence band maximum, but significantly affect the conduction band minimum, which was found as high as ~4 eV for NaCl bi- and tri-

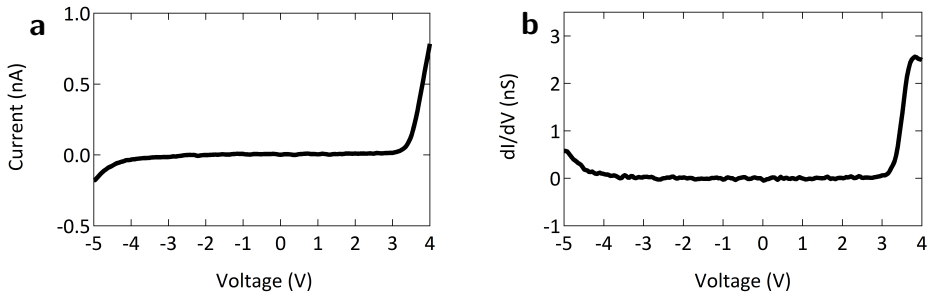

Figure 2.6: **Bandgap of copper chloride.** **a**, The $I(V)$ and **b**, $dI/dV(V)$ curves taken on top of the $Cu_2Cl/Cu(100)$ surface. The band gap is about 7 eV in size.

layers on copper [84]. In our case, a sharp step in the differential conductance at ~3.5 V denotes the conduction band minimum (Figure 2.6). The precise onset of the band was determined as the maximum in the normalized differential conductance $\mathrm{d}I/\mathrm{d}V \times V/I$. As we will show in Chapter 4, chlorine vacancies have a state that lies just within the bandgap. This feature is used to observe a band shift in vacancy structures, and to construct 'artificial molecules' in Chapter 5.

During measurements, keeping the tip feedback on keeps the tunnel current constant – instead of the height – and therefore this is much safer for taking spectra at some structures: currents exceeding $I > 1$ nA frequently caused unintended displacement of the atoms in e.g. the checkerboard lattices in Chapter 4. If the z-V curve recorded in this way is numerically derived, a $\mathrm{d}z/\mathrm{d}V$ measurement can be extracted. The technique of using the difference between topography images to make $\Delta z/\Delta V$ DOS maps is developed in Section 4.4.

2.7. VACANCY-VACANCY INTERACTIONS

In order to understand the stability of a single vacancy and the interaction between vacancies, we collaborated with theoreticians José Lado and Joaquín Fernández-Rossier[1], who performed the DFT calculations and Monte Carlo simulations presented here.

Density functional theory (DFT) calculations permit an order of magnitude estimate of the single-vacancy switching rates. The estimated attempt frequency for a Cl atom to overcome the energy barrier $\Delta = 0.3$ eV, obtained for the small oscillation analysis around the equilibrium position, yields $\Gamma_0 = 48$ THz. Thus, we can estimate the thermally activated switching rate $\Gamma_0 \exp(-\Delta/k_B T)$, where k_B is the Boltzmann constant, to be in the range of $1 \cdot 10^{-5}$ Hz (several hours lifetime) at a temperature $T = 77$ K, although large error bars have to be assigned due to the exponential dependence on Δ. As shown in Figure 2.7a,b, taken 44 h apart at 77.5 K, the manipulated vacancies are found experimentally to be stable for at least that amount of time, provided they are properly positioned. Vacancies arranged within two unit cells of each other are found to settle into a lower energy state – a 'bow-tie'-like shape – within tens of minutes at this temperature,

[1] International Iberian Nanotechnology Laboratory (INL) in Braga, Portugal [42]

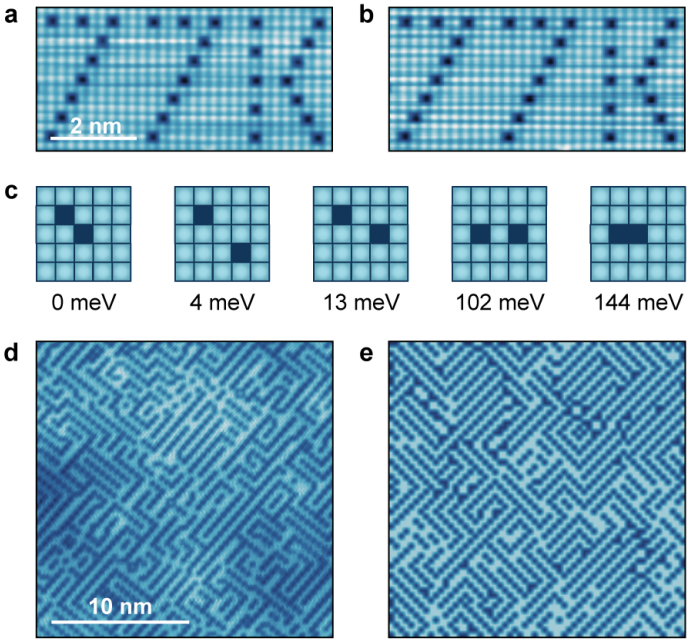

Figure 2.7: **Thermal stability and vacancy–vacancy interactions. a**, STM image (I = 300 pA, V = +200 mV) of arranged vacancies measured at 77.5 K. **b**, As in **(a)**, but taken 44 h later. **c**, DFT calculations on the energetics of pairs of vacancies, indicating that orientations along the (1,1) direction are strongly favoured over orientations along the (1,0) direction. **d**, STM image (I = 500 pA, V = +500 mV, T = 1.5 K) taken at a vacancy coverage of x = 0.309, showing a stripe pattern. **e**, Monte Carlo simulation for T = 100 K of a two-dimensional vacancy gas with $x = 1/3$ and vacancy–vacancy interactions as shown in **(c)**. The cell size is 60 × 60, and the result is shown after 400,000 steps starting from a random distribution.

see Figure 2.8.

To understand the vacancy–vacancy interaction, we computed several configurations with two vacancies (Figure 2.7c) in a supercell of up to 5 × 5 Cl atoms. We find that the minimal energy configuration for a pair is the diagonal dimer, that is, two consecutive vacancies along the (1,±1) direction, which explains the observed high natural abundance of these configurations. This finding goes a long way to account for the formation of a stripe phase with coexisting domains along the (1,±1) directions, observed near $x = 1/3$ (Figure 2.7d). Monte Carlo simulations (see below), using the vacancy–vacancy interactions discussed above (Figure 2.7e), are in very good agreement with the experiment and show that this system provides an ideal physical realization of a lattice gas model, for which stripe phases are expected [88].

The 'bow-tie'-shaped objects, displayed in Figure 2.8, seem to be formed from two vacancies that have collapsed to a lower energy state with a temperature increase. While they are mostly formed from {2,0} configurations, which have the highest energy for two-vacancy arrangements closer than $2a$, we can also see them forming from {1,±1} spac-

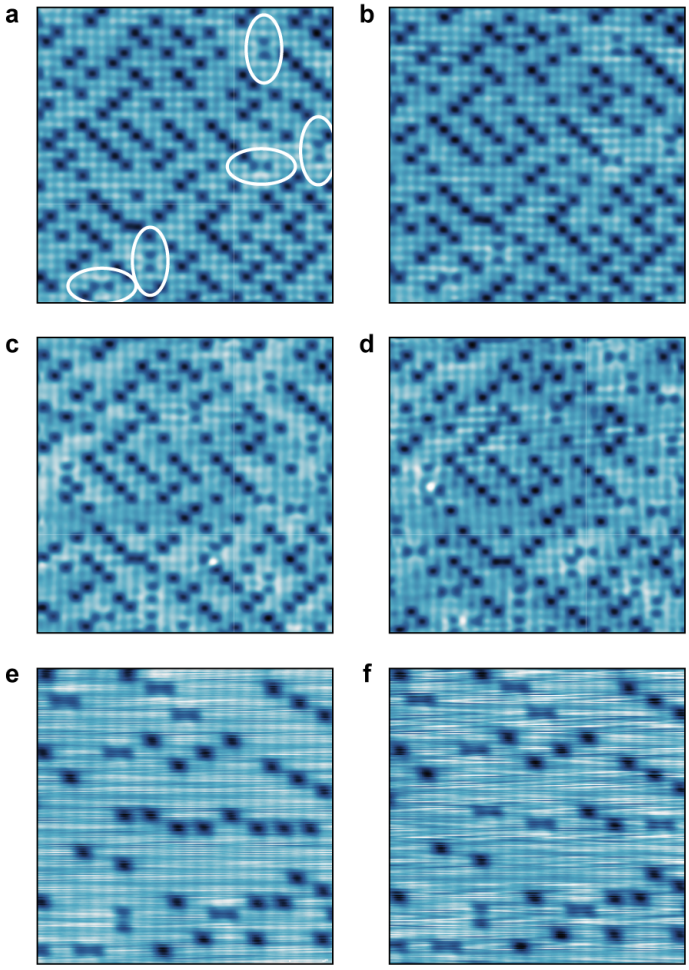

Figure 2.8: **Thermal and temporal stability above liquid nitrogen temperatures. a**, STM image of vacancies in a natural configuration, measured at 77.3 K. The image shows five 'bow-tie'-shaped objects (marked), the exact atomic structure of which is unknown. **b**, Same as (**a**), but measured 19 hours later. No vacancy has moved. **c**,**d**, STM images of the same area as (**a**) and (**b**), but measured at 78.2 K and 78.4 K, respectively, taken only minutes after (**b**). The number of bow-tie objects is found to increase with increasing temperature. **e**, STM image of vacancies arranged to form a byte, measured at 77.5 K. **f**, Same as (**e**), but measured 50 minutes later. Several vacancies positioned in the (2,0) configuration have changed into bow-tie objects.

ings with higher temperatures.

A single phase-shifted chlorine atom occurs sporadically, but only in the middle of 2×2 empty positions, thus being equivalent to three vacancies. Because the total number of vacancies should be conserved when below the temperature for chlorine desorp-

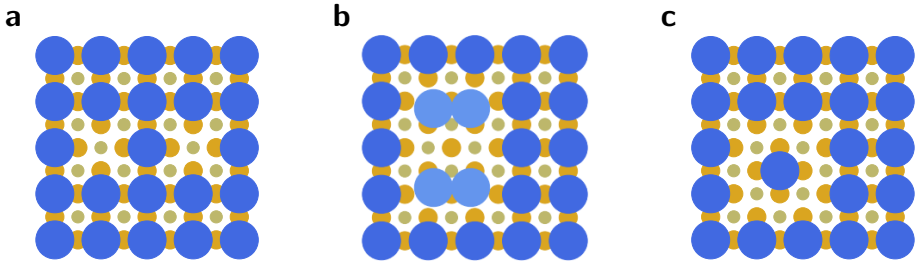

Figure 2.9: **Schematic of various vacancy structures.** Orange circles are Cu atoms in the top layer, khaki the Cu atoms in the second layer, blue the Cl atoms. **a**, A {2,0} dimer, **b**, a possible configuration for the bow-tie, and **c**, a phase-shifted Cl atom. At elevated temperatures, we see {2,0} dimers (**a**) collapse into bow-tie structures, as in Figure 2.8. They look different from regular {1,0} dimers, so we speculate that although the two vacancies move together, the two bordering Cl atoms on either side look brighter, as if they are shifted inwards and up (**b**). Not to be confused with a single phase-shifted chlorine atom (**c**), because the number of vacancies should be conserved.

tion, which is < 200 °C, this is a different configuration, and our bow-tie structures are probably not just phase-shifted atoms.

The bow-tie consists of a pair of vacancies, but occupies only two lattice sites. The chlorine atoms on either side of the bow-tie appear a bit brighter than the other chlorine atoms in the surface, which suggest that the configuration is still equivalent to a {1,0} dimer, but with the surrounding atoms slightly elevated, and/or pushed inwards, to create the optical effect of resembling a bow-tie, see Figure 2.9.

We almost never find a naturally occurring {2,0} or {1,0} dimer when the system is at low (< 4 K) temperatures, but we do sometimes see a bow-tie. The {2,0} and {1,0} dimers that we have built, are stable at low temperatures, but collapse to bow-ties when exposed to higher temperatures. This might indicate that these are equivalent, even though they are both much less likely to occur than the {2,1} and {1,1} dimers, because the latter are much lower in energy, see Figure 2.7c.

2.7.1. DFT AND MONTE CARLO CALCULATIONS

Density functional theory (DFT) calculations and Monte Carlo simulations[2] were done with the Quantum Espresso package [89], using the PBE exchange correlation functional and PAW pseudopotentials. Relaxation of a unit cell with one Cl and four Cu layers showed that the top layer does not suffer strong deformations. This result did not show an important dependence on the number of Cu layers, remaining unchanged even with only two Cu layers. The structural changes in the presence of a Cl vacancy were calculated in a 3×3 super-cell, allowing full relaxation of the system. The main changes appeared in the position of the Cl atoms, which were pushed towards the site with the missing Cl atom. In comparison, the positions of the Cu atoms barely changed.

The lowest-energy path for a vacancy, shown in Figure 2.4b, was calculated in the 3×3

[2] Performed by José Lado and Joaquín Fernández-Rossier from the International Iberian Nanotechnology Laboratory (INL) in Braga, Portugal [42].

unit cell, moving the position of one of the Cl atoms towards the vacancy, and calculating its energy in every step. In this calculation we constrained the position of all the Cl atoms except the mobile one. The mobile atom had the position in the direction of the vacancy fixed, whereas the other two coordinates were allowed to relax. The path followed by the Cl atom was above the Cu atom, avoiding becoming closer to other Cl atoms. The energetics of the path did not depend strongly on whether the other atoms were allowed to fully relax or not.

For calculation of the vacancy–vacancy interaction, 5×5 super-cells with two Cl vacancies were chosen. The different arrangements of vacancies were calculated, allowing all the Cl atoms to relax. We find that the vacancies have a first-neighbour repulsive interaction, preferring a diagonal arrangement. Qualitative results do not depend on whether the Cu atoms are also allowed to relax. The same calculation with a 4×4 unit cell gave similar results.

From the energetics of the DFT calculation for the vacancy–vacancy interaction, we can build a classical lattice gas model defined on the square lattice S. In this model, each site can be either full or empty. For a given configuration, the energy of the system is

$$\mathscr{U} = \sum_{\mathbf{r},\mathbf{r}'\in S} f(\mathbf{r}-\mathbf{r}')\, n_{\mathbf{r}} n_{\mathbf{r}'} \tag{2.1}$$

where $n_{\mathbf{r}}$ is the occupation of site $\mathbf{r}$ (1 for a vacancy, 0 for a filled Cl site). The interaction $f(\mathbf{r},\mathbf{r}')$ affects every pair of vacancies and its value is taken from the energetics obtained by DFT:

$$f(\mathbf{r}-\mathbf{r}') = \begin{cases} 0.144 & \text{if} \quad \mathbf{r}-\mathbf{r}' \in \{(1,0),(0,1),(-1,0),(0,-1)\} \\ 0.102 & \text{if} \quad \mathbf{r}-\mathbf{r}' \in \{(2,0),(0,2),(-2,0),(0,-2)\} \\ 0.013 & \text{if} \quad \mathbf{r}-\mathbf{r}' \in \{(2,1),(1,2),(-2,1),(1,-2),(2,-1), \\ & \qquad\qquad (-1,2),(-2,-1),(-1,-2)\} \\ 0.004 & \text{if} \quad \mathbf{r}-\mathbf{r}' \in \{(2,2),(2,-2),(-2,2),(-2,-2)\} \\ 0 & \text{otherwise} \end{cases} \tag{2.2}$$

where the energies are in eV. Using the standard Metropolis update algorithm, we carry out Monte Carlo simulations within the canonical ensemble, that is, with a fixed total number of vacancies, at a given temperature T. The temperature enters in the Metropolis update as the tolerance for accepting a new configuration with higher energy. Starting from an initial random configuration, at every step the update algorithm attempts to move a random vacancy to a random neighbouring filled site. For $T \to 0$, only new configurations that lower the energy are accepted, so a local energy minimum is finally reached. For $T \to \infty$, any new configuration is accepted, leading to a fluctuating and disordered state.

Starting from a randomly generated configuration, the Monte Carlo evolution drives the system towards a local free energy minimum. The system develops different domains with stripes in different directions, as observed in the experiment. For the calculations in the main text, a relaxation of 400,000 steps was carried out. Finally, it is worth noting

that the results do not change qualitatively if a simpler interaction is assumed:

$$f(\mathbf{r}-\mathbf{r}') = \begin{cases} 0.144 & \text{if} \quad \mathbf{r}-\mathbf{r}' \in \{(1,0),(0,1),(-1,0),(0,-1)\} \\ 0 & \text{otherwise} \end{cases} \tag{2.3}$$

2.8. CONCLUSIONS AND OUTLOOK

We have prepared chlorine terminated copper (100) surfaces with variable vacancy densities, for imaging and manipulation by scanning tunnelling microscopy. The non-saturated Cu_2Cl surface is characterised by single vacancy defects in large unobstructed terraces, unlike the island formation, typically only tens of nanometers large, that form in the Cu_2N surface [58]. This means that if the surface is used as a decoupling layer, it is only limited by the crystal terrace size, which can be hundreds of nanometres wide. Together with the slightly larger work function compared to similar substrates, this might lead to better opportunities of studying magnetism and other phenomena at the atomic scale, such as single atoms [36], chains [35], or more complex designs that might be assembled at the nanoscale. In Chapter 7, we will discuss the properties of various atoms adsorbed on the Cu_2Cl surface.

We developed a vacancy manipulation technique, where the STM can controllably exchange a vacancy with one of the neighbouring atoms, with sometimes more than 99 % directional reliability. This manipulation was improved to be fast (~1 manipulation per second), so large-scale structures can be built, as demonstrated in Chapter 3. Furthermore, any vacancy structure can be built with high precision and relatively fast, as can be seen in Chapters 4, 5 and 6.

As shown in Figure 2.8, the vacancies in the Cu_2Cl surface are stable below 77 K, the temperature of liquid nitrogen. This means that the investigation of denser structures where the individual vacancies are closer than three lattice spacings ($3a$) apart, must be conducted at 77 K at the highest. Kept at low temperature in ultra-high vacuum for more than seven months, no significant contamination issues arose. This suggests that the surface is sufficiently chemically stable under these conditions, possibly allowing us to lift some of the stringent requirements without losing surface quality.

The Cu_2Cl surface is stable, can be prepared with reliable vacancy coverages, such that large-scale automated vacancy manipulation is possible. Since the heavier halogens Br and I have similar reconstructions on copper, they might be very viable alternatives to Cl, using the techniques developed in this chapter. Finally, new venues might be found when combining the insulating properties of the substrate with the possibility of large-scale atom manipulation, creating hybrid designs where atoms or molecules are placed on custom-designed vacancy structures with locally varying material properties.

3

A KILOBYTE REWRITABLE ATOMIC MEMORY

The advent of devices based on single dopants, such as the single-atom transistor [90], the single-spin magnetometer [91, 92] and the single-atom memory [93], has motivated the quest for strategies that permit the control of matter with atomic precision. Manipulation of individual atoms by low-temperature scanning tunnelling microscopy [16] provides ways to store data in atoms, encoded either into their charge state [25, 94], magnetization state [31, 32, 76] or lattice position [95]. A clear challenge now is the controlled integration of these individual functional atoms into extended, scalable atomic circuits. Here, we present a robust digital atomic-scale memory of up to 1 kilobyte (8,000 bits) using an array of individual surface vacancies in a chlorine-terminated Cu(100) surface. The memory can be read and rewritten automatically by means of atomic-scale markers and offers an areal density of 502 terabits per square inch, outperforming state-of-the-art hard disk drives by three orders of magnitude.

Parts of this chapter have been published in Nature Nanotechnology **11**, 926-929 (2016) [42].

THE chlorine terminated copper surface, $Cu_2Cl/Cu(100)$, introduced in Chapter 2, exhibits vacancies that can be manipulated with a very high directional reliability. In this chapter, we demonstrate the extent to which the vacancies can be manipulated, by constructing a data storage device of a full kilobyte in size (1,024 bytes), where every bit is described by the position of just one vacancy. Comparably large atomic-scale data storage has been demonstrated earlier using individual Si atoms on top of a Si–Au surface [95], but, in contrast to the current work, the memory could be written only once, and the entire surface had to be regenerated to change a single bit.

3.1. BIT DESIGN

In our structure, we define a pair consisting of a chlorine atom (Cl) and a vacancy (V) as a bit, where the V–Cl configuration (as read from top to bottom in the STM scans) represents the '0' and Cl–V the '1'. To avoid vacancies directly neighbouring each other, which would render automated locking of the STM tip on individual vacancies impossible, we implemented a row of Cl atoms to separate bits in both the horizontal and vertical directions. For this reason, six lattice sites are needed for a bit, or 48 lattice sites for a byte (Figure 3.1a), resulting in an optimal vacancy coverage of $x = 1/6 = 0.167$ when the surface consists only of bits.

We have not been able to controllably create or destroy vacancies without altering the tip apex. As a result, the vacancy coverage can be controlled only during sample preparation and cannot be changed afterwards. The bit arrays presented here were all made on a surface with $x = 0.115$. To compensate for the vacancy deficiency in comparison to the optimal coverage, the memory is organized into blocks of 8 bytes (64 bits) as shown in Figure 3.1b-d, separated by a margin of four unit cells. Constructing this block configuration requires a vacancy coverage of $x = 0.118$, which is within 3% of the actual coverage. These blocks form a convenient way to organize the data. A readout and a rewrite of a block take ~1 and 2 min, respectively.

3.2. AUTOMATION

We make use of an autonomous manipulation method [96] that permits the construction of large memories. A marker at the top left of each block defines the scan frame and the lattice for the complete block. After scanning the area, the positions of all vacancies are determined via image recognition. Next, a path-finding algorithm is used to calculate the building sequence, guiding the vacancies to their respective final positions. The markers for adjacent blocks are built automatically as part of the construction, and leftover vacancies are swept to the side to be used in future blocks. Automated construction of a complete block takes on the order of 10 min.

The scalability of the technique is demonstrated in Figures 3.3, 3.4, and 3.5 which show a complete memory consisting of 1,016 bytes (8,128 atomic bits) written to three different texts. Owing to local defects or contaminants, some areas are not suitable for building switchable bits. Such local imperfections do not necessarily affect the functionality of the memory. By properly defining markers consisting of several vacancies (Figure 3.2) blocks can be designated as broken and will be skipped in the reading and writing sequences. Additional markers denoting, for example, the start or end of a line,

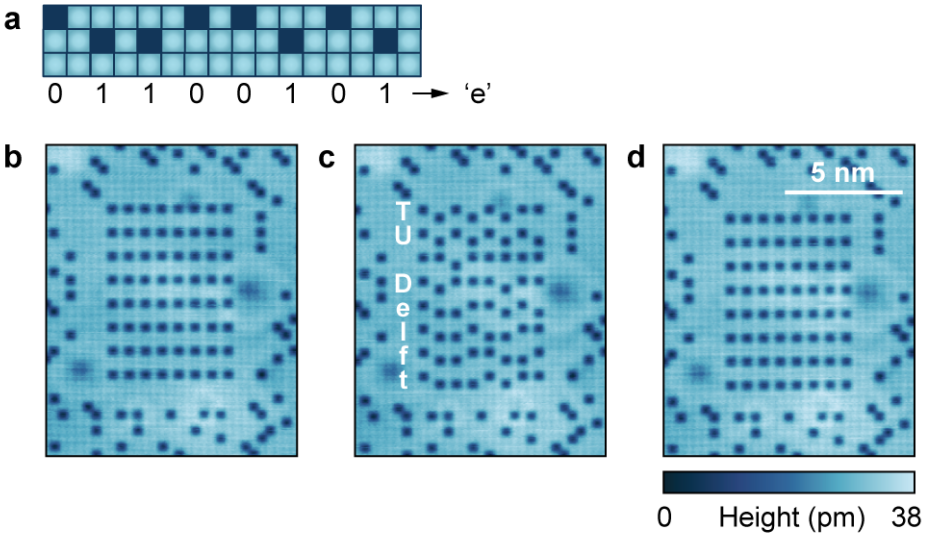

Figure 3.1: **Data-encoding principle. a**, Diagram showing the smallest possible byte, provided that vacancies are not direct neighbours. The byte is set to represent the binary ASCII code for the character 'e'. **b–d**, STM images (I = 2.00 nA, V = +500 mV, T = 1.5 K) of a 64-bit block, written as (**b**) all 0s, (**c**) a text and (**d**) all 1s.

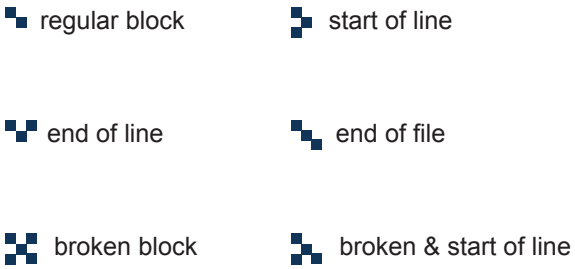

Figure 3.2: **Markers defining the functionality of each 64-bit block.** Vacancies are placed in six easily recognisable configurations in an area of 3 × 3 positions. Each marker is placed to the top-left side of a 64-bit block, and is interpreted by the automated reading and writing sequence.

allow for fully automated navigation of the STM tip through the memory. More complex markers may be designed to allow travel of the STM tip over longer distances and in arbitrary directions. Because 12% of blocks are not suitable for data storage, the actual areal density of the complete memory decreases to 0.778 bits/nm^2, or 502 terabits per square inch (Tbpsi).

PATH-FINDING ALGORITHM AND ITS LIMITS

The procedure for the automatic assembly of vacancy arrays is as follows. First, a marker is built at the top left of the area designated for a 64-bit data block. To define the scan frame, the STM tip locks onto one of the vacancies in the marker, using an atom tracker sequence. Provided that the scan angle and piezo calibrations are fixed, only one marker is needed to fully define the scan frame. In practice, our tip piezo elements are well calibrated, so no rhombic distortion occurs for which all four markers would be needed. After moving the scan frame, however, we frequently needed to correct the scan angle and frame size, in order to exactly fit the integer number of lattice positions (22×30, plus any margin rows on the outside of the markers). As the scan angle is a crucial ingredient for successful vacancy manipulation, frequent recalibration by using two markers is necessary.

After completing a scan, image recognition is used to identify the positions of all the vacancies in the scan. The initial configuration is compared to the desired final configuration and each vacancy is assigned to a final position by means of the Munkres algorithm [97, 98], attempting to minimize the total distance to be traversed. Vacancies are guided to their destinations using an A* path-finding algorithm [99], which prevents vacancies from running into each other or forming dimers.

The computer program keeps a list of assignments that still need to be completed and sends commands to the STM accordingly. Commands include *'move tip to vacancy at <location>'* and *'move vacancy into <direction>'*. The assignments are based on the current configuration of vacancies as tracked by the program. The STM sends the outcome of each task back to the program. If the STM reports that a vacancy moved in the wrong direction, assignments are recalculated based on the new configuration.

A particular difficulty in the guiding process is to prevent vacancies from blocking each other so that their final position cannot be reached. For this situation, we first identify the vacancies that form a blockage to a specific final position and sort these in order of increasing distance to this position. Next, we move the first vacancy on the list to the final position, the second vacancy to the former position of the first vacancy and so on.

Unfortunately, when the vacancies are required in a denser arrangement, for instance in a 2×2 arrangement as built in Chapter 4, the program has more difficulty to solve the path-finding problem. As it is not possible to track a vacancy's location when it is directly adjacent to another vacancy, this is a situation that needs to be avoided in automated vacancy manipulation. Frequently, the moving vacancy is blocked from its destination by the surrounding vacancies, and because moving directly past other vacancies is not allowed, the autonomous manipulation program does not work for coverages $\geq 25\%$.

In our data storage, the vacancy coverage is $x = 0.115$, where each bit has an area of 2×3 unit cells. To increase the overall information density, reducing the bit area to 2×2 will not be an option for automatic writing of the memory, but reducing the number of margin rows in between blocks still gives space for improvement. In the current memory, four rows separate the blocks from each other in all directions, where the markers are placed at the top left corner of each 8-byte block. Reducing the margin to two rows still allows the use of 3×3 markers, by occupying the unused lattice sites of the 64^{th} bit of the block above. This would bring the required vacancy coverage to $x = 0.141$ and the

resulting information density to 1.085 bits/nm^2, or 700 Tbpsi. Reducing the margins even further, to only one row, would mean that the markers of each block need to be redefined, as they have less space to occupy. The optimal coverage is then $x = 0.155$, resulting in an areal density of 1.195 bits/nm^2, or 771 Tbpsi.

A supplementary movie of the autonomous assembly of one 64-bit block can be viewed at `http://ottelab.tudelft.nl/vacancy-manipulation`. It shows a real-time screen capture taken during automated vacancy manipulation without human interaction. At the beginning of the movie, all shown windows are briefly introduced. The movie starts at the moment a scan of the area has been taken and interpreted by the image recognition program. Three atomic markers, which were built as part of previous blocks, are already in place. The movie shows 264 manipulations, one of which is in an unintended direction.

3.3. REWRITABILITY

Starting with an area that is large enough ($\sim 100 \times 100$ nm^2), with relatively few defects, the data storage is constructed in ten days time. The text we wrote in our atomic memory was two inspiring paragraphs from Feynman's lecture *There's plenty of room at the bottom* [6, p. 34], as can be seen in Figure 3.3:

> But I am not afraid to consider the final question as to whether, ultimately - in the great future - we can arrange the atoms the way we want; the very atoms, all the way down! What would happen if we could arrange the atoms one by one the way we want them (within reason, of course; you can't put them so that they are chemically unstable, for example).
>
> Up to now, we have been content to dig in the ground to find minerals. We heat them and we do things on a large scale with them, and we hope to get a pure substance with just so much impurity, and so on. But we must always accept some atomic arrangement that nature gives us. We haven't got anything, say, with a "checkerboard" arrangement, with the impurity atoms exactly arranged 1,000 angstroms apart, or in some other particular pattern.
>
> There's plenty of room at the bottom, R. P. Feynman, December 29th 1959.

Reading or rewriting the entire kilobyte was done with a LabView program that compares the heights of the '0' and '1' positions of each bit, and from this infers the value. It reads all the bits one-by-one, starting with the first byte in the first block. After the first block, it moves the tip to the marker of the next block, re-setting its relative coordinates and checking the status of that block. After the first row of blocks, it moves to the first block in the next row by tracking for a second at each of the intermediate markers, to correct for any inaccuracies due to the large movement. The approximate reading speed is 1 bit per second. A total read-out of the memory takes in the order of 30 min.

A rewrite sequence goes through the bits in the same way, but compares the value of each bit to the new value, and switches the bit if needed. This takes more time, typically 2-4 hours. The two other texts written to this memory can be seen in Figures 3.4 and 3.5.

We optimised our reading and rewriting sequences to be reliable, not for speed. As a consequence, a large part of the time is spent tracking markers and bits, to ensure

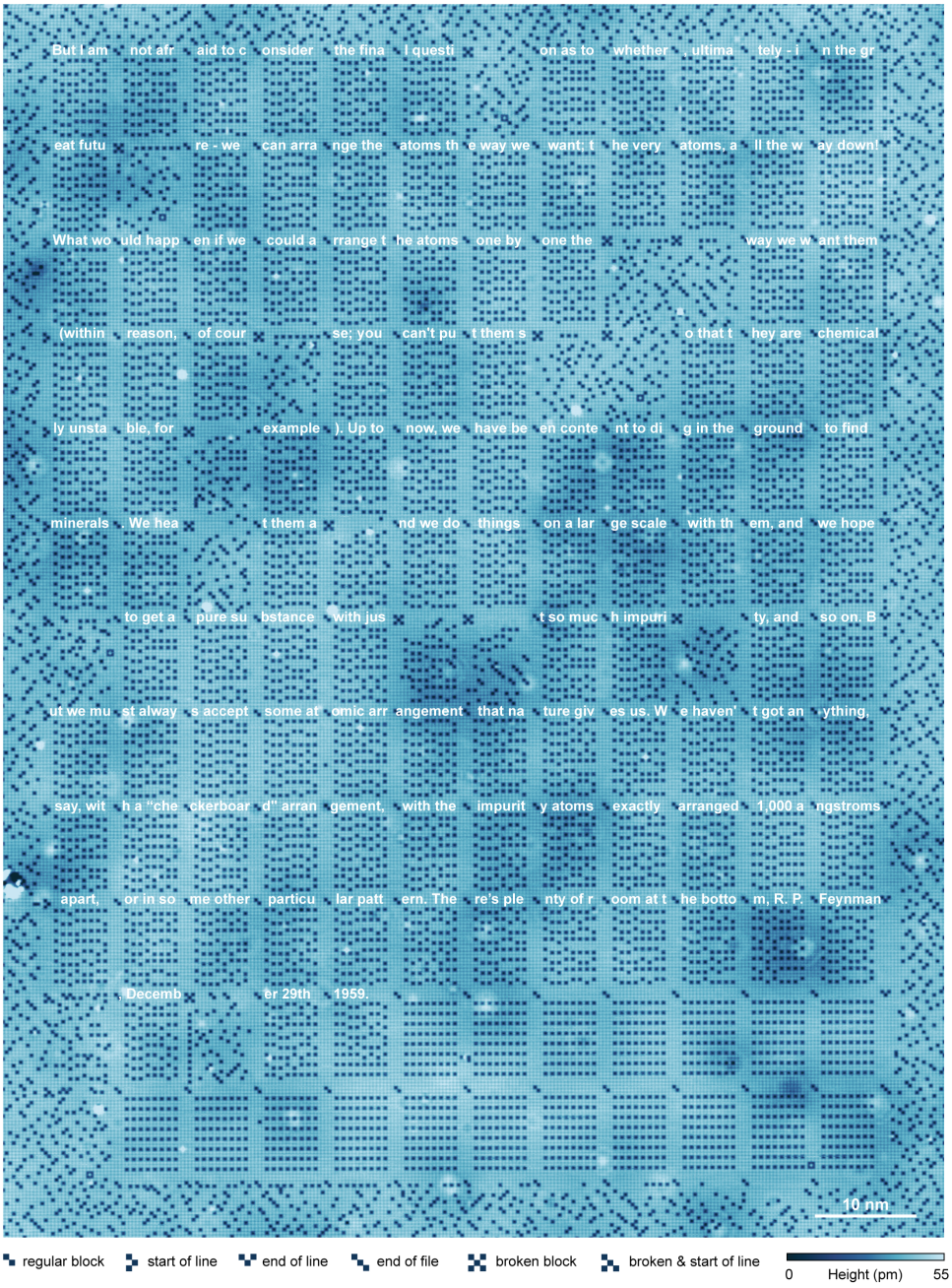

Figure 3.3: **Kilobyte atomic memory.** STM image (96×126 nm, $I = 2.00$ nA, $V = +500$ mV, $T = 1.5$ K) of a 1,016-byte atomic memory, written to a passage from Feynman's lecture *There's plenty of room at the bottom* [6]. The various markers used are explained in the legend below the images. The memory consists of 127 functional blocks and 17 broken blocks, resulting in an overall areal density of 0.778 bits/nm^2.

the correct navigation of our tip. The reading time can be brought down by adopting different strategies, such as by checking only the height of the '0' position of each bit.

3.4. CONCLUSIONS AND OUTLOOK

Having several thousands of single-atom bits represents a significant step forward in the field of atomic-scale electronics. An important improvement still to be made is an orders of magnitude increase in the readout speed. To this end, the memory would have to be scanned in constant height mode rather than constant current mode. At constant tip height, using settings similar to those presented here, the current difference between a Cl atom and a vacancy is on the order of 1 nA. Demonstrated high-frequency STM electronics [100] allow a 1 nA signal to be measured at a bandwidth of 1 MHz, suggesting that readout speeds on the order of 1 Mb/s should be attainable. The required scan speed of 0.36 mm/s can be achieved by using video-rate STM [100]. There is no physical limitation that prevents the fabrication of much larger in-plane atomic memories.

Going to higher temperatures, such as 77 K, can be very advantageous in order to make this data storage technique more accessible. Liquid nitrogen is much cheaper and easier to handle than liquid helium, and the STM can be designed in a much simpler way, due to the reduced necessary cooling power and thermal insulation. As no spectroscopy is needed on the atomic memory, only the ability to manipulate atoms reliably, the only constraint is the stability of the surface itself.

As shown in Figure 2.8, the Cu_2Cl substrate is stable up to 77 K; however, the bytes as we designed them, two unit cells apart, are not. Apparently, the two unit-cell vacancy spacing configuration is too eager to collapse into a lower energy state, but a spacing of three unit cells as in Figure 2.7 is still stable at high temperatures. This means that the bit design has to be adapted, e.g. each bit now in a 3×3 area, so the information density will go down by at least a third from 502 Tbit/inch^2 at 4 K to ~335 Tbit/inch^2 at 77 K.

When going to memories that are much larger than our kilobyte, locating a block when the tip is far away becomes a big issue. Large and fast movements cause the piezo actuators of the tip to lag behind, a process called piezo 'creep', and the tip position will only be stable after enough waiting time. This can be solved with intermediate 'stepping stones' every ten to twenty nanometres, where the tip can track and recalibrate its position on a marker, before moving to the next marker. We already used this method in our kilobyte-sized memory when moving from one row to the next. Tracking on a marker typically takes in the order of a second, because shorter tracking times hamper the accuracy. For larger memories, this means that the moving time will go up, because of the increased number of stepping stones.

Knowing where the tip currently is located, and where it needs to go, is also very important here. The markers developed here are simple prototypes in a 5×5 space that can still be deciphered by the human eye. For larger memories, however, it might be more desirable to develop bigger markers with encoded coordinates, like the increasingly used QR-codes.

When the memory size grows, it eventually becomes larger than the scan range of a normal scanning tunnelling microscope, which is in the order of a few micrometers at low temperatures. Scaling up to higher temperatures would be advantageous here, because the piezoelectric materials that determine the scan range result in larger exten-

sions with higher temperatures, while at the same applied voltage. At some point, it becomes necessary to involve multiple STM tips, as proposed in IBM's 'Millipede' project [101]. One of the main difficulties here would be to control them independently from each other. Maybe it is not necessary to completely decouple the movements of the tip, but each tip would still have to be aligned with respect to the other tips, before starting a simultaneous readout of each section's n^{th} bit. A scheme like this would greatly improve the speeds for writing and read-out.

Finally, it might be the case that there are substrates where it is equally possible to manipulate vacancies, but with a higher melting temperature, such that a memory can remain stable above 77 K and for longer time periods. Similar substrates such as the heavier halogens – bromine and iodine – on copper (100) come to mind, which form similar surface reconstructions [49, 50, 67–69]. Furthermore, with the recent advancements in assembling stacked structures from 2D-materials such as graphene, h-BN, MoS_2, and many more, it becomes tempting to fantasize about an expansion in 3D space. Translating the two-dimensional storage density presented here to three dimensions, would – assuming a modest vertical pitch of 5 nm – allow the storage of the entire US Library of Congress in a cube 100 µm wide.

From a physical perspective, the fact that we can manipulate thousands of atoms per day, and create structures where more than sixty thousand atoms lie exactly in their intended positions, really does ring true on Feynman's words, we can now "arrange the atoms one by one the way we want them".

3.5. SUPPLEMENTARY FIGURES

Aside from the paragraphs from Feynman's lecture shown in Figure 3.3, two other texts were written in the atomic data storage. Two paragraphs from the preface and introduction of Charles Darwin's *On the Origin of Species* [102] were written in Figure 3.4. Note that the topographical area is identical in both images, as the broken blocks and impurities are the same in both.

To further demonstrate the rewritability of our memory, a third text was written, see Figure 3.5. Here, one of the broken 8-byte blocks was repaired – seventh row from the top, sixth column from the left – as the impurity there was mistakenly believed to prevent the bit from functioning. With this repaired block, the total number of blocks equals 128, which means the total storage holds 1 KiB = 1,024 bytes (8,192 bits), and the total areal density now rises to 506 terabits per square inch.

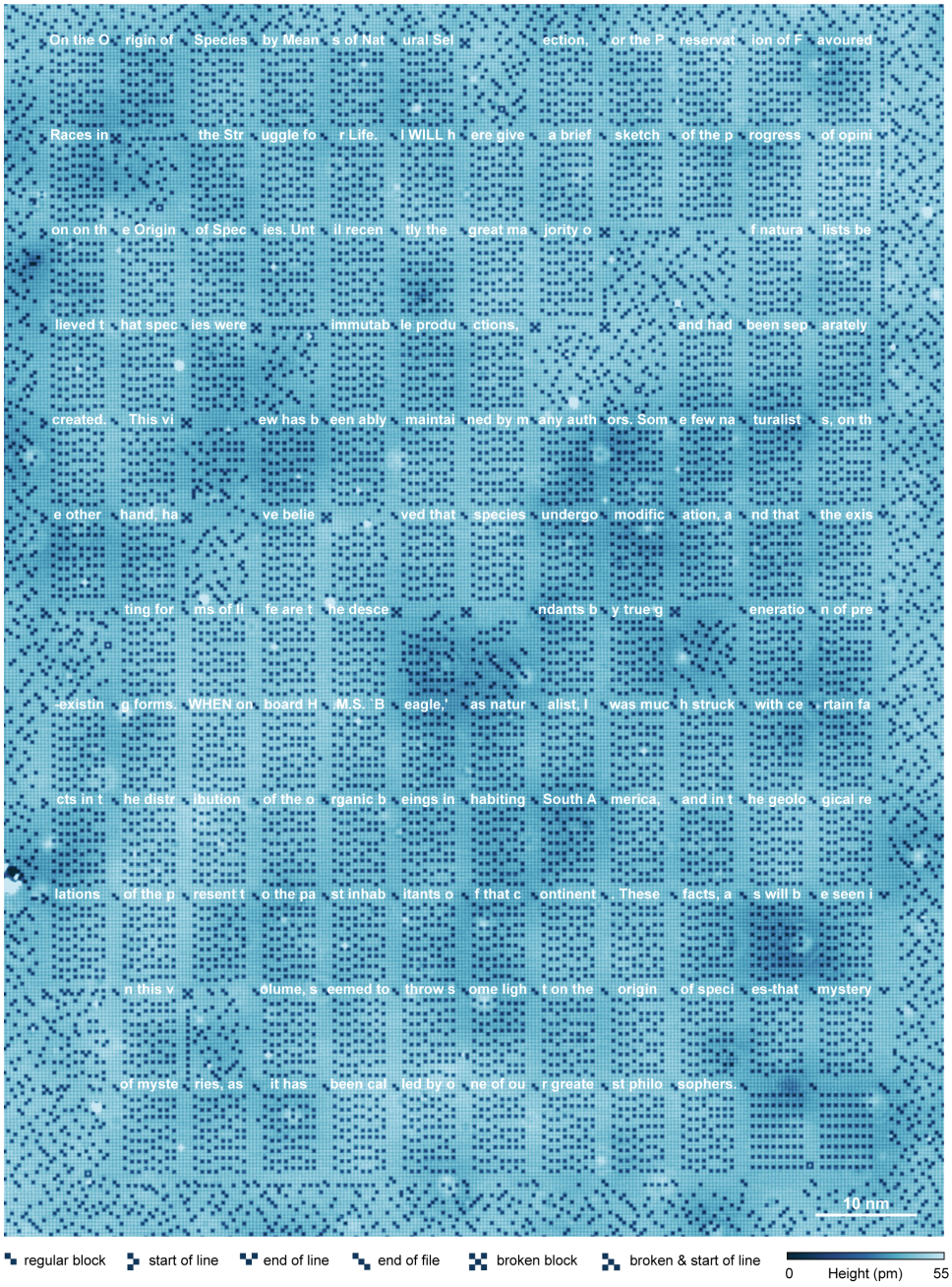

Figure 3.4: **Kilobyte atomic memory.** STM image (96×126 nm, I = 2.00 nA, V = +500 mV, T = 1.5 K) of the same 1016 byte memory as shown in Figure 3.3, written to a different text. The presented text is an excerpt from the preface (*An Historical Sketch*, page xv) and the introduction (page 1) of *On the Origin of Species*, by Charles Darwin (slightly adapted to fit the memory) [102].

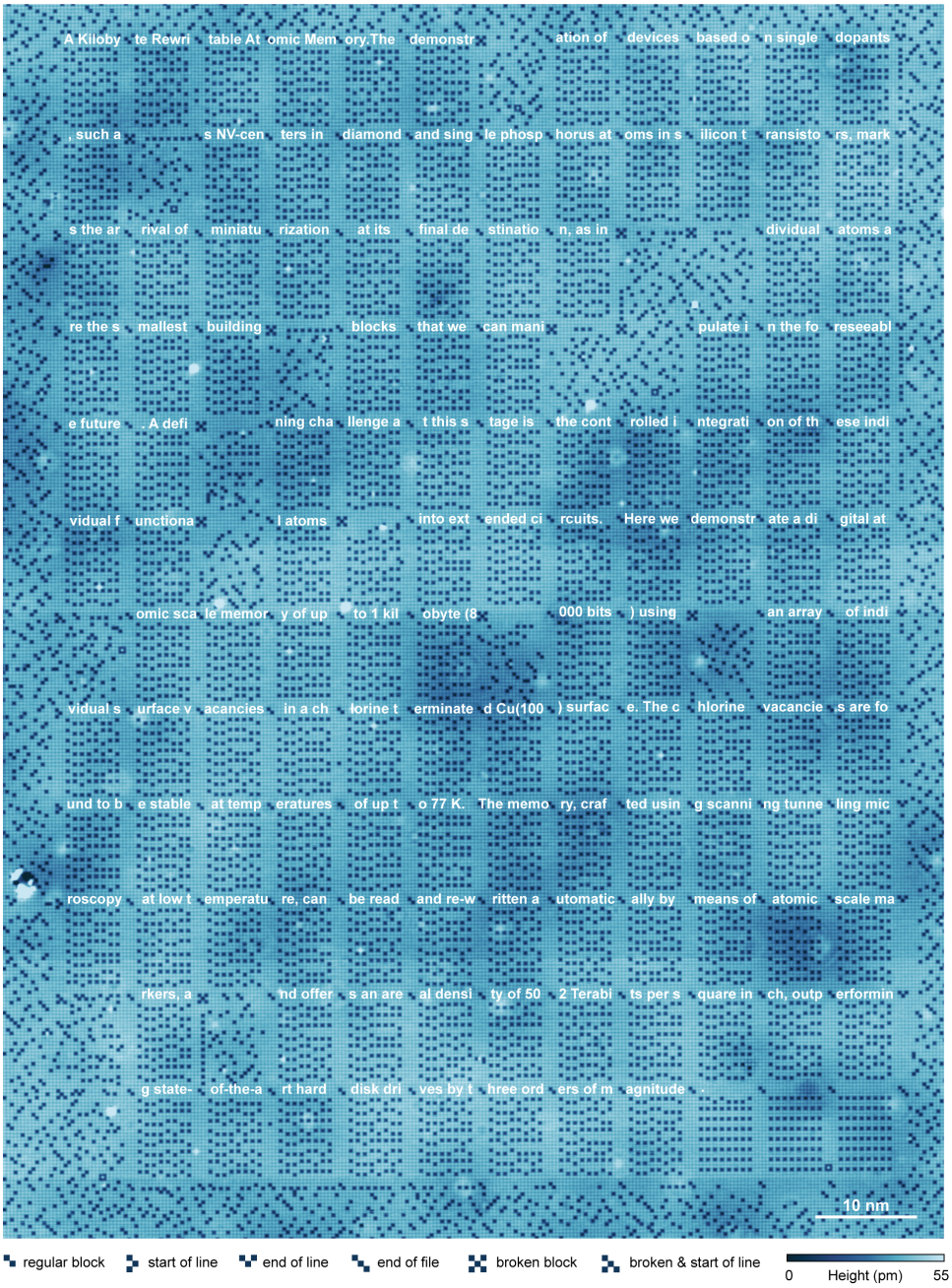

Figure 3.5: **Kilobyte atomic memory.** STM image (96×126 nm, I = 2.00 nA, V = +500 mV, T = 1.5 K) of the memory shown in Figure 3.3, extended to 1,024 bytes (8,192 bits), written to the abstract of an early version of [42]. The areal density of this modified memory is 506 terabits per square inch.

4

EMERGENCE OF QUASIPARTICLE BLOCH STATES IN ARTIFICIAL CRYSTALS

The interaction of electrons with a periodic potential of atoms in crystalline solids gives rise to band structure. The band structure of existing materials can be measured by photoemission spectroscopy and accurately understood in terms of the tight-binding model, however not many experimental approaches exist that allow to tailor artificial crystal lattices using a bottom-up approach. The ability to engineer and study atomically crafted designer materials by scanning tunnelling microscopy and spectroscopy (STM/STS) helps to understand the emergence of material properties. Here, we use atom manipulation of individual vacancies in a chlorine monolayer on Cu(100) to construct one- and two-dimensional structures of various densities and sizes. Local STS measurements reveal the emergence of quasiparticle bands, evidenced by standing Bloch waves, with tuneable dispersion. The experimental data are understood in terms of a tight-binding model combined with an additional broadening term that allows an estimation of the coupling to the underlying substrate.

Parts of this chapter have been published in SciPost Physics **2**, 020 (2017) [43].

ATOM manipulation by means of STM is a viable way of constructing atomically precise artificial structures [103]. Among others, the technique can be used to engineer atomic scale logic devices [29, 45], low dimensional magnetic systems [19, 35, 76] or atomic data storages [31, 32, 42]. As our abilities to manipulate atoms on a large scale are improving, the formation of atomically designed artificial crystals becomes of particular interest driven by a demand for new materials where the properties are defined by emerging quasiparticle states [104]. Common approaches to build low-dimensional artificial materials by STM include confinement of electronic surface states through precise assembly of individual atoms and/or molecules [105–108], self-assembly of molecular networks [109, 110] and manipulation of dangling bonds [111] or surface vacancies [47]. The recent development of large-scale fully automated placement of atomic vacancies on a chlorinated copper crystal surface [42] provides an excellent platform to explore various lattice compositions. These vacancies were found to host a localized vacancy state in the surface band gap, similar to dopants in semiconductors, allowing their combined electronic states to be modelled by means of tight-binding approximation [112].

Here, we present a study of artificial one- and two-dimensional structures built from Cl vacancies in an otherwise perfect monolayer square lattice formed by chlorine atoms on a Cu(100) surface. Using local electron tunnelling spectroscopy, we demonstrate that we are able to reach system scales where the spectral properties no longer depend on size and which we therefore consider to be in the limit of infinite lattice size. For structures with a sufficiently large vacancy density, we observe quasiparticle Bloch waves that can be simulated by using a tight-binding model. Similar wave patterns were reported previously in assembled chains of Au atoms [108], which were best described in terms of a free electron model. Analysis of the Bloch wave dispersion allows us to extract quasiparticle effective masses, which are found to depend strongly on the chosen lattice structure.

4.1. VACANCY STATES

As reported in Chapter 2, a monolayer of chlorine atoms on Cu(100) exhibits a surface band gap of about 7 eV (see inset of Figure 4.1a) as well as a shift in the substrate's work function by 1.25 eV [55], suggesting a significant charge transfer between the substrate and chlorine atoms and formation of the interface dipole moment [86].

As previously reported by Drost et al. [112], when the Cu_2Cl/Cu(100) interface possesses defects in the form of missing chlorine atoms (*vacancies*, dark square in the inset of Figure 4.1a), a localised electronic vacancy state is resolved at lower voltages ~3.4 V (green curve Figure 4.1a). The vacancy state exhibits similarities to localized states observed on gold atoms adsorbed on NiAl(110) [108], in the gap region of hydrogen-doped Si(100) surface [111], and on chlorine vacancies in NaCl/Cu(111) [84]. When two vacancies are brought close to each other by means of atom manipulation [42], the spatial overlap of the wave functions leads to the formation of bonding and anti-bonding orbitals [84, 108, 111]. These molecular orbitals can be effectively described within the tight-binding model with their energy depending on the hopping term t – a measure of the overlap of the two vacancy states through the underlying potential.

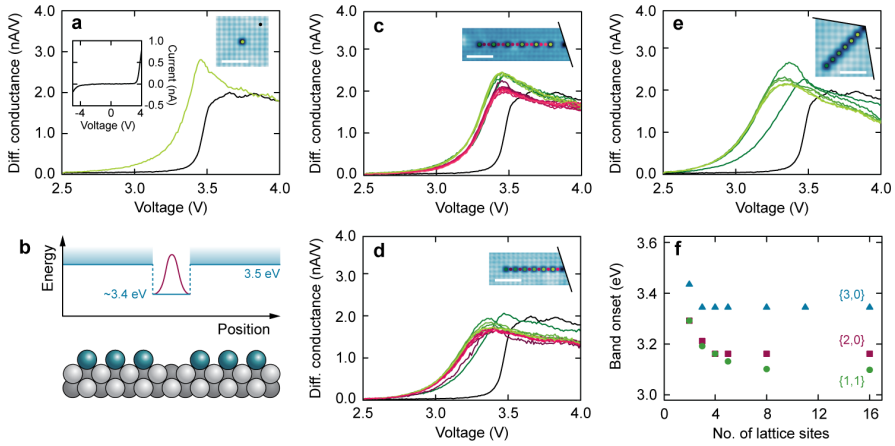

Figure 4.1: **Differential conductance spectra acquired on a chlorine vacancy in the Cl/Cu(100) substrate and in artificial 1D lattices crafted from the vacancies.** **a**, $\mathrm{d}I/\mathrm{d}V$ measurement taken inside a chlorine vacancy (green) and on the bare Cl/Cu(100) substrate (black). Dots depict positions where spectra were taken. The inset shows an I-V curve acquired from -4.5 to 4.0 V where the surface band gap of E_g ~7 eV is clearly visible. **b**, Sketch denoting the energy level of the vacancy state with respect to the band continuum. **c**, **d**, **e**, $\mathrm{d}I/\mathrm{d}V$ spectra taken on vacancy sites and/or chlorine interstices (locations indicated by coloured dots in the insets) on lattices with 16 vacancy sites for spacing configurations $\{3,0\}$ (**c**), $\{2,0\}$ (**d**) and $\{1,1\}$ (**e**). **f**, Evolution of the band onset as a function of lattice spacing and lattice size. Data points indicate the position of the band onset extracted from spectra taken on the middle vacancy of each lattice. In the case of an even-length chain, the averaged value measured on the two centre vacancies is shown. STM images were acquired in constant current mode, $I = 2$ nA and $V = 500$ mV. All scale bars are 2 nm.

4.2. ONE-DIMENSIONAL LATTICES

We built one-dimensional lattices of the Cl/Cu(100) vacancies of various lengths and lattice spacing ($\{3,0\}$, $\{2,0\}$ and $\{1,1\}$) as shown in Figure 4.1. The notation $\{x, y\}$ used here describes spacing between adjacent vacancies in the horizontal and vertical directions, respectively, in multiplies of the lattice constant $a = 0.355$ nm. Differential conductance ($\mathrm{d}I/\mathrm{d}V$) spectra, presented in Figure 4.1, were acquired along chains of length 16, for all three spacing parameters. The spectra reveal a shift of the band onset towards lower voltages and broadening of the spectral features for the lattice of denser spacing. Both the shift and the band broadening result from the increased overlap between neighbouring sites. The observed spectral features show a correlation with the position within the chains, i.e. the band minimum measured on outer vacancies is found at higher energies compared to that resolved on inner ones. The correlation of the band minimum with the position within the chain is related to the broken translational symmetry at the outer positions and leads to the appearance of zero-dimensional states [108]. This dependence is further corroborated for edge vacancies within denser lattices where the effect is more pronounced (e.g. Figure 4.1e). Spectra acquired on the chlorine atoms within the chains show a similar spatial dependence of the band onset.

In Figure 4.1f, we plot the dependence of the band onset as a function of the chain length, measured at the centre of each chain. For each lattice spacing, the band onset

is found to saturate, however at different lengths: the {3,0} chains saturate at 3.35 eV already for length 3, the {2,0} chains at 3.18 eV for length 5 and the {1,1} chains at 3.1 eV for length 8. The saturation of the band minimum implies an approach of the limit where edge effects no longer play a role for the inner vacancies and the chains can be effectively treated in the limit of infinite lattice size. Furthermore, the observed shift relates to the size of the hopping parameter t which increases for smaller lattice spacing [112].

4.3. TWO-DIMENSIONAL LATTICES

To further investigate the band formation, we built two-dimensional structures with varying lattice spacing, ({3,3}, {2,3}, {2,2}) as well as 'stripes' and 'checkerboard' arrays, all of varying lattice size (Figure 4.2). For 2D lattices, the notation $\{x, y\}$ denotes the lattice spacing in the x and y directions in units of the lattice constant a. Moving inward along the diagonal of each structure, the position of the band onset shifts towards lower energies for denser and larger lattices, similar to the 1D lattices. In the case of the stripes lattice we observe two band onsets, $E_1 = 2.8$ eV and $E_2 = 3.1$ eV, measured at the centre vacancy (see Figure 4.2g). We attribute these to the two different lattice constants along the lattice diagonals, $a_1 = 0.51$ nm and $a_2 = 0.69$ nm. Assuming that the hopping parameter is exponentially dependent on the distance [112] and the bandwidth is linearly proportional to the hopping parameter t, the band is expected to be symmetric around the energy $E = 3.4$ eV of a single vacancy. We estimate the widths of the respective bands to be $W_1 \sim 1.2$ eV and $W_2 \sim 0.6$ eV, leading to a ratio $W_1/W_2 \sim 2$. This ratio is somewhat higher than the ratio between the hopping parameters $t(a_1)/t(a_2) \sim 1.2$, suggesting that another effect may play a role, affecting the width and/or position of the band, e.g. an electric field due to positively charged neighbouring vacancies observed at polar insulating surfaces. Such an electric field can cause a shift of the band onset towards lower energies, which is expected to be larger for denser lattices [47].

Just as in the one-dimensional case, we found that for larger lattices, the onset of the band shifts to lower energies. We constructed lattices of size $N \times N$ of the three least dense types ({3,3}, {2,3}, and {2,2}), up to $N = 16$, and plotted the band onset as function of N, see Figure 4.2f. Of sizes $N \geq 8$, the band onset does not change anymore, so we can assume the centre of the lattice to no longer be affected by edge effects.

4.4. DOS MAPS

The checkerboard lattice (Figure 4.2e) was found to be more sensitive to relatively high tunnelling currents than lattices with lower vacancy coverage. For large tunnelling current and voltage values, we observed chlorine atoms unintentionally changing their position, rendering the structure unstable and sometimes causing the entire structure to collapse. This instability seems to be strongly voltage dependent, as vacancy manipulation happens at 500 mV and ~1 μA. For bias voltages <1 V, most structures can handle currents in the microampère range, but for the higher density structures, even lower currents can be disastrous with high voltages, e.g. >2 nA at ~4.7 V.

In order to qualitatively extract the local density of states (DOS) in the checkerboard and stripes lattices, we used a method where, instead of acquiring $\mathrm{d}I/\mathrm{d}V$ spectra, we recorded the tip-sample distance z as a function of applied bias voltage V. The time con-

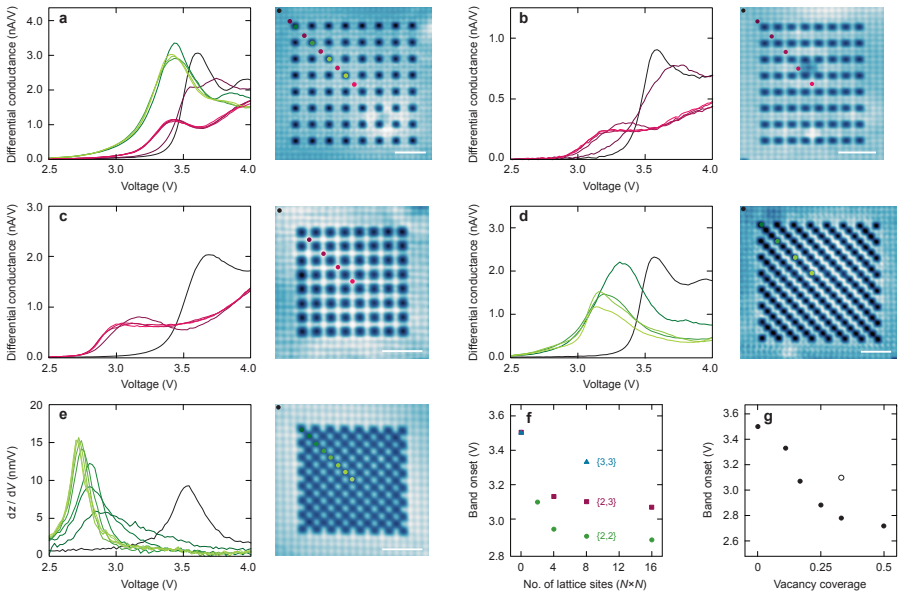

Figure 4.2: **Analysis of artificial 2D lattices by chlorine vacancies on Cl/Cu(100). a**, **b**, **c**, **d**, **e**, Differential conductance spectra measured along diagonals of the lattices with spacing {3,3} (**a**), {2,3} (**b**), {2,2} (**c**) and with stripes (**d**) and checkerboard (**e**) patterns. Coloured dots denote the positions where the spectra were acquired. **f**, Evolution of band onset as a function of lattice spacing and lattice size. Band onset was extracted from the spectra taken in the middle of the lattices. **g**, Band onset as a function of lattice density, i.e. number of vacancies divided by number of total positions in the unit cell. STM images were acquired in constant current mode $I = 2$ nA and $V = 500$ mV. All scale bars 2 nm.

stant of the feedback-loop was much smaller ($t = 25$ µs) than the time set to measure a single data-point ($t \sim 1$ s), thus ensuring that the tip had enough time to stabilize. In this mode the tunnelling current was kept constant at $I = 500$ pA. Subsequently, a numerical derivation of a z-V curve, i.e. the $\mathrm{d}z/\mathrm{d}V$ curve, has been extracted (see Figure 4.3). As the tunnel current I is exponentially proportional to the tip-sample distance z,

$$I(z) = AVe^{-2\frac{\sqrt{2m\phi}}{\hbar}z} \tag{4.1}$$

where A is a constant, V the bias voltage, m the mass of the tunnelling electron, ϕ the height of the tunnelling barrier and $\hbar$ the reduced Planck constant. Extracting z as a function of the tunnelling current and the applied bias voltage results in

$$z = \frac{\ln(\frac{I}{V}) - \ln(A)}{-2\frac{\sqrt{2m\phi}}{\hbar}} \tag{4.2}$$

Derivation of the distance z to voltage V gives

$$\frac{\mathrm{d}z}{\mathrm{d}V} \propto \frac{\mathrm{d}I}{\mathrm{d}V}\frac{V}{I} \tag{4.3}$$

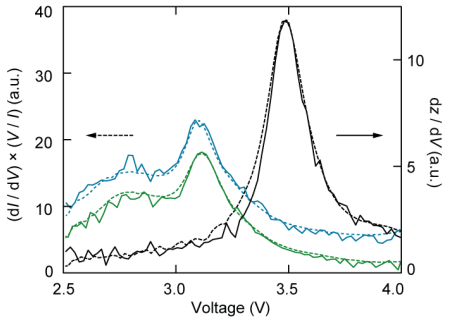

Figure 4.3: **Comparing dz/dV** (solid lines) **and dI/dV × V/I spectra** (dashed lines). Black, blue and green correspond respectively to the bare Cl/Cu(100) substrate and two different vacancies within the stripes lattice.

As can be seen from Equation (4.3), the dz/dV is linearly proportional to the normalized differential conductance spectra (dI/dV × V/I), which in turn is proportional to the local density of states (LDOS).

dz/dV maps have been acquired in constant current mode, where consecutive topography images have been taken on the same area at different bias voltages in 10 mV intervals for checkerboard lattices and in 50 meV intervals for stripes lattices. The consecutive images have been subtracted, thus providing the height difference dz for each point of the topography images for the respective voltage difference dV.

4.4.1. STANDING WAVES

Apart from preserving the lattice integrity, the dz/dV measurement mode also provides sufficient sensitivity to detect standing wave modes in some of the lattices that are not visible in dI/dV mode. Figure 4.4 shows dz/dV maps acquired on the checkerboard (panels a-d) and stripes (panels j-k) lattices. Interestingly, the modes are resolved very symmetric in the x and y directions, i.e. the number of protrusions in both directions is equivalent, even though the unit cell of the stripes lattice is highly asymmetric.

To shine more light onto the standing wave pattern, we performed numerical calculations of artificial lattices of size 8 × 8 using a tight-binding approach that effectively simulate dz/dV maps (Figure 4.4e-h, l-n), which are proportional to the density of states (see Section 4.4.3 for details). The observed modes can be described in terms of two-dimensional confinement modes with k-vectors $k_x = N\pi/L$ and $k_y = M\pi/L$, where L is the width of the lattice. The experimentally observed modes resemble some of the calculated modes with $N = M$ (Figure 4.6a). However, the experimental data show a richer structure with the links connecting the very bright protrusions in x and y direction. Furthermore, the experimentally observed modes are gradually transforming from one mode to another with an increasing number of lobes. At certain energies some of the lobes are not spherical, but rather have an elongated shape, that splits into two with increasing voltage.

This smooth crossover can be reproduced by including the coupling of the confined modes to the electronic bath underneath. This interaction, which is mathematically represented by a self-energy term with finite imaginary part, leads to a finite lifetime of the

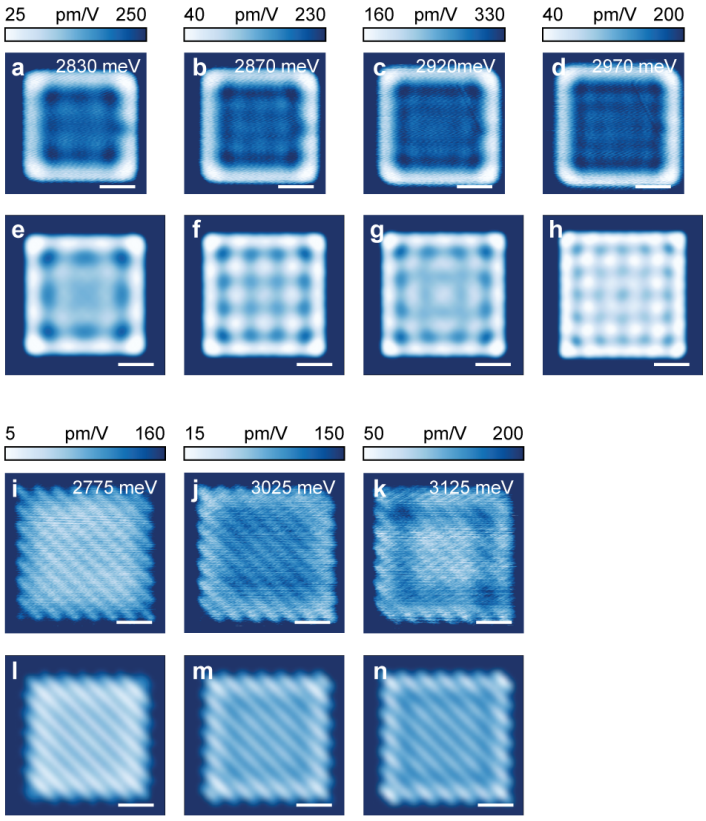

Figure 4.4: **dz/dV maps acquired on checkerboard and stripes lattices.** **a**, **b**, **c**, **d**, dz/dV maps taken on an 11×11 checkerboard lattice at different energies. **e**, **f**, **g**, **h**, Corresponding numerical calculations using a tight-binding model including an additional hybridization term. **i**, **j**, **k** and **l**, **m**, **n**, Similar to **(a)**-**(d)** and **(e)**-**(h)** for a 7×7 unit cells stripes lattice of the same size. All scale bars 2 nm.

states and a broadening of the spectral function, which consequently overlap neighbouring energy states and alter the appearance of the modes (see Section 4.4.3 for details on the numerical calculations). The addition of this hybridization term yields a DOS profile composed from the mixture of many individual modes that can no longer be resolved, and resembles up to very fine details the experimental STM maps, including the smooth crossover. Similar broadening of the energy modes was also attributed to strong electron-phonon coupling [84]. As such, the experimental modes have to be understood as coming from the mixture of many individual modes due to the finite coupling of the lattice to the underlying copper, so that at a particular energy we do not observe a single confined mode, but a weighted mixture of the neighbouring modes.

In a similar manner, we calculated the DOS on the stripes lattice, where the distance between vacancies along two lattice directions is not equal. We included two different

hopping terms in our calculations in order to properly reproduce the experimental data. If only the hopping term along the direction of the stripes is considered, the numerically resolved modes within the chains are decoupled from each other and do not reflect the experimentally observed patterns (Figure 4.6b). Comparison of numerical results with the experimental images allows to directly extract the effective hopping parameters for the effective square lattices. In our numerical simulations we used a model with only first neighbour hopping term of -215 meV, that reproduces the features of checkerboard lattice very well, but fails to capture the features of stripes lattice. However, the tight binding model with first and second neighbour hopping parameters -139 meV and -38 meV, respectively, can reproduce both the checkerboard and stripes lattice patterns to a great extent.

Assigning mode numbers to the standing waves in Figure 4.4 is possible when realising that the bright spots represent the anti-nodes in the wave pattern, and the dark spots the nodes. The outermost anti-nodes of e.g. the $N = 4$ mode blend together in our measurements and in the simulations below, which means that the modes shown in Figure 4.4a-d are $N = 4,5,6,7$ (checkerboard), and those in Figure 4.4j,k are $N = 3,4$ (stripes).

The standing wave pattern is present in all lattices of these two vacancy densities. Checkerboard arrays of two different sizes (8×8 and 11×11 unit cells) have been built, as well as a 45° rotated 8×8 unit cell lattice. The standing wave pattern is present in all of them, and in the rotated lattice, the pattern is also rotated, to fit the boundary conditions (Figure 4.8). Stripes lattices of the same sizes (5×5 and 7×7 unit cells) both show the standing wave pattern as well (Figure 4.7). For the different lattices of a certain density, the modes occur at different energies, but when the lattice size is taken into account, they follow the same dispersion relation $E(k)$. This demonstrates that the quasiparticle dispersion really is a property of the material that we built, regardless of its size, boundaries and orientation.

4.4.2. TWO-DIMENSIONAL FAST FOURIER TRANSFORM

The previous discussion requires investigation of the $\mathrm{d}z/\mathrm{d}V$ maps one by one and identifying the interference patterns. The emergence of dispersive modes within the maps can be explored systematically by taking the quantitative fast Fourier transform (FFT) analysis of these $\mathrm{d}z/\mathrm{d}V$ maps as in Figure 4.5a-f.

Each pixel of the FFT image carries information about the intensity I, i.e. weight, of the corresponding k-vector value. Then, the intensity and the corresponding k-vector value are squared, i.e. I^2 and k^2, respectively. The profiles along the k_x^2 axis, i.e. $k_y^2 = 0$, and along the k_y^2 axis, i.e. $k_x^2 = 0$, are normalized by the sum of I^2, leading to expectation values $\langle k_x^2 \rangle$ and $\langle k_y^2 \rangle$, respectively. The $\mathrm{d}z/\mathrm{d}V$ maps exhibit a noise signal with a very small real-space wavelength, corresponding to a large k-vector, thus we calculate the expectation values considering only 3 points left and 3 points right from the maximal I^2. Profiles along the k_x^2 and k_y^2 axes appear identical and we thus calculate the expectation value $\langle k^2 \rangle = (\langle k_x^2 \rangle + \langle k_y^2 \rangle)/2$.

This expectation value of the square of the k-vector $\langle k^2 \rangle$ of each FFT image is used to assign a single value to a complete $\mathrm{d}z/\mathrm{d}V$ map. Plotting the energy E (i.e. the applied bias voltage) as a function of $\langle k^2 \rangle$, we provide a dispersion curve that allows to

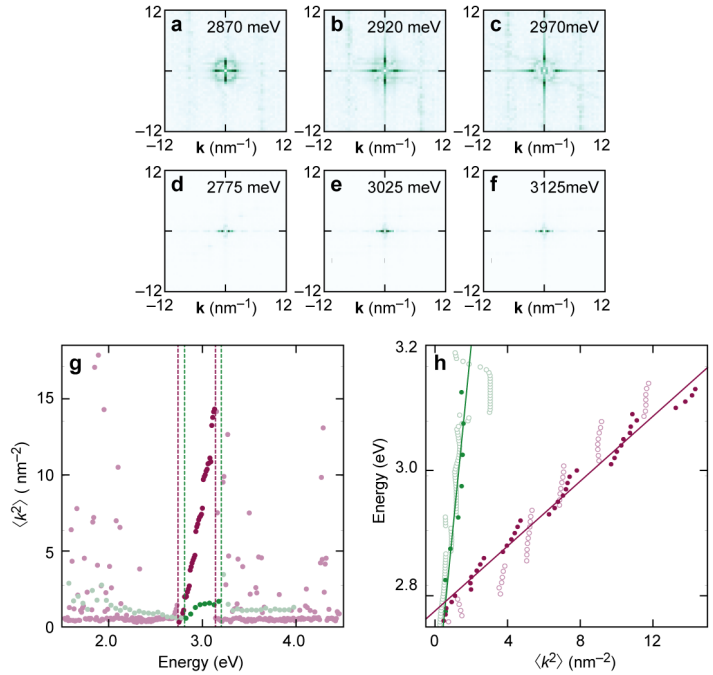

Figure 4.5: **Fourier analysis of the dz/dV maps. a**, **b**, **c**, **d**, **e**, **f**, Evolution of the Fourier map for the checkerboard and stripes lattices at different energies, corresponding to dz/dV maps presented in Figure 4.4**(a)**, **(b)**, **(c)**, and **(i)**, **(j)**, **(k)**, respectively. Increasing energy leads to a shift of the maximal intensity towards higher k-vector values. **g**, Evolution of the expectation value of the square of the momentum vs. the energy for checkerboard (purple) and stripes lattice (green) in a wide energy range. Dashed lines define the energy intervals within which the dispersive modes are observed in each lattice. **h**, Dispersion plots E vs. $\langle k^2 \rangle$ for the energy intervals marked in **(g)**. The experimental and theory data points are represented by full and open circles, respectively. Solid lines show linear fits, from which the effective masses of experimental observed modes are extracted.

systematically identify the energy regions where an interference pattern is visible. Figure 4.5h shows the obtained dispersion diagrams for the checkerboard in the energy interval 2750 meV to 3140 meV, and for the stripes lattice in the energy interval 2775 meV to 3175 meV. The full E vs. $\langle k^2 \rangle$ plots are shown in Figure 4.5g.

4.4.3. DISPERSION RELATION

We performed linear fits to the E vs. $\langle k^2 \rangle$ plots in order to extract effective electron masses for the checkerboard $m_{\text{eff}} = 1.470 \pm 0.034\ m_e$ and for the stripes lattice $m_{\text{eff}} = 0.131 \pm 0.025\ m_e$, where m_e is the free electron mass. One would expect the stripes lattice, being highly anisotropic, to yield different effective masses for the directions parallel and perpendicular to the stripes. However, the weight in the FFT maps is found predominantly along the k_x and k_y axis, which are rotated 45°with respect to the stripes. Therefore, a single value for the effective mass suffices to describe the observed standing wave patterns. The obtained values suggest that quasiparticle waves in the checker-

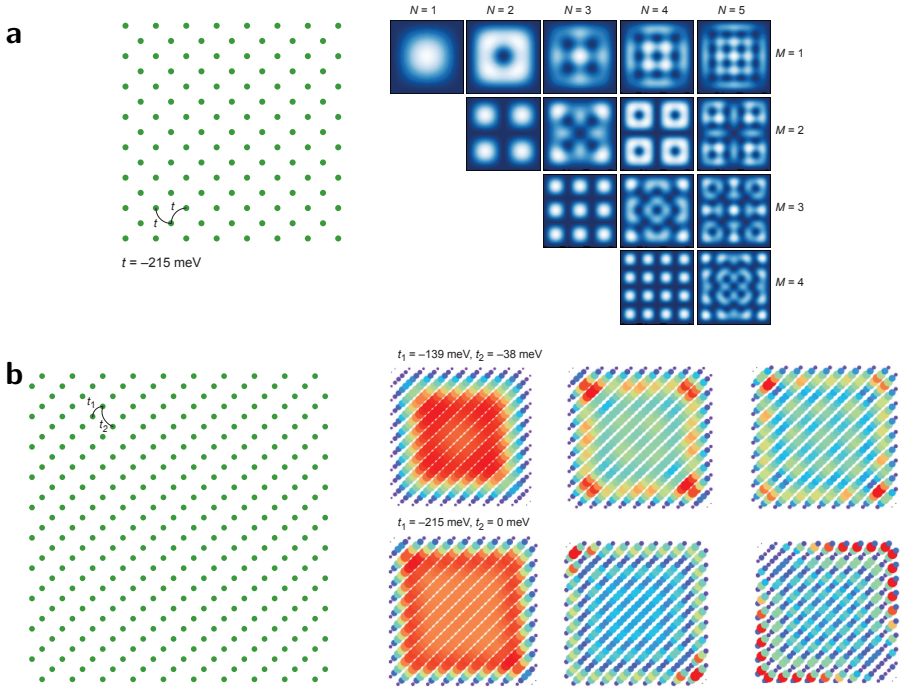

Figure 4.6: **Numerical calculations on (a) checkerboard and (b) stripes lattice using a tight-binding model. a**, Standing wave patterns acquired from the numerical calculations with the hybridization term set to zero. The integers N and M denote number of modes for k_x and k_y axis. **b**, Standing wave pattern within the stripes lattice has been simulated using nearest neighbour and next nearest neighbour hoping terms (top row) or nearest neighbour hopping term only (bottom row). Experimental data are better reproduced using both the nearest and next-nearest hopping term.

board lattice are heavier than those in the stripes lattice. While the calculations confirm this observation (theory: checkerboard: $m_{\text{eff}} = 0.98 \pm 0.06\ m_e$ and stripes: $m_{\text{eff}} = 0.22 \pm 0.016\ m_e$), intuitively, one might expect the checkerboard lattice, being denser than the stripes lattice, to provide greater band width due to larger hopping parameters, and therefore to yield a lower effective mass. The dispersive properties found from the analysis in Figure 4.5 should therefore be considered as phenomenological only. Structures of the same density also show the same dispersion relation, regardless of size or angle.

NUMERICAL CALCULATIONS

We performed numerical calculations[1] for a model Hamiltonian defined on two different geometries: the checkerboard lattice and the stripes lattice. In both situations the size of the lattice we considered is exactly the same as in the experiment. The calculations are

[1] Numerical calculations were performed by José Lado and Joaquín Fernández-Rossier from the International Iberian Nanotechnology Laboratory (INL) in Braga, Portugal [43].

performed in the tight-binding approximation using a Hamiltonian with local orbitals in the form

$$\mathscr{H} = \sum_{ij} t_{ij} c_j^\dagger c_i \tag{4.4}$$

where the parameters t_{ij} are the elements of the overlap matrix between states localized within the chlorine vacancies and defined as

$$t_{ij} = \langle \psi_i | \mathscr{H} | \psi_j \rangle \tag{4.5}$$

where $c_j^\dagger$ and c_i are creation and annihilation operators at sites j and i, respectively.

In our calculations, we use a value of -139 meV for the first neighbour hopping term t_1 and a value of -38 meV for the second neighbour hopping term t_2. Furthermore, to simulate the potential well, we use the edge potential of 38 meV for the checkerboard lattice and 80 meV for the stripes lattice.

The effect of the hybridization with the metallic bath is taken into account by means of a self-energy parameter with finite imaginary part, that enters the Dyson equation of the Green function. For simplicity we assume the self-energy term to be site-independent and diagonal, which allows to precisely reproduce the experimental features in a wide energy range. The Green function is thus defined as follows:

$$G(E) = (E - \mathscr{H} - \Sigma)^{-1} \tag{4.6}$$

with the self-energy term defined as

$$\Sigma = i\delta \tag{4.7}$$

where $\delta = 40$ meV. Within the previous Green function, the density of states at the site i is given by

$$\rho_i(E) = \mathrm{Im}(G_{ii}(E)) \tag{4.8}$$

The spatially resolved DOS is calculated assuming that the local state ψ_i, centred in $\mathbf{r}_i$ has the form

$$\psi_i(\mathbf{r}) = N e^{-(\mathbf{r}-\mathbf{r}_i)^2/\sigma^2} \tag{4.9}$$

with $\sigma = 0.9d$, where d is the first-neighbour vacancy-vacancy distance.

Theoretical calculations of the artificial checkerboard lattice of size 8×8 using a tight-binding approach with $t = -215$ meV without hybridization term are shown in Figure 4.6a, showing the individual modes. In two dimensions, the patterns are characterized by two vectors k_x and k_y, that are independent of each other. The vectors are defined as $k_x = N\pi/L$ and $k_y = M\pi/L$, where $N, M = (1, 2, 3, ..., 8)$ are the mode numbers and L is the size of the lattice ($L = 8$ in our case). In order to get agreement with the experiment, a finite hybridization with the metal is needed. Furthermore, in the case of the stripes lattice, an additional next nearest neighbour hopping term is needed. In Figure 4.6b, we show calculations for the stripes lattice using the tight-binding model without hybridization term, (i) with nearest neighbour and next-nearest neighbour hopping term and (ii) with nearest neighbour hopping term only. The best agreement with the experimental results is found when both terms are included.

4.5. CONCLUSIONS

Engineering artificial lattices by means of atom manipulation of chlorine vacancies in the Cl/Cu(100) substrate demonstrate a way to craft artificial one- and two-dimensional materials with tunable electronic properties. We explore the emergent band formation as we build lattices of varying structure, density and size. For all lattices studied, the bottom of the emerging band is found to shift towards lower energies, in accordance to the tight-binding model, as the lattice size or density is increased. Furthermore, we find that the band onset saturates for larger structures, implying that the effect of finite size can be neglected. In the case of two-dimensional checkerboard- and stripe-shaped lattices, we observe standing Bloch waves. These patterns are well explained using a tight-binding model that includes coupling to the electron bath. Surprisingly, the effective mass of the observed Bloch waves is found to depend strongly on the lattice geometry. Our work provides a testing ground for future designer materials where the electronic properties can be defined a priori.

4.6. SUPPLEMENTARY FIGURES

dz/dV maps have been acquired in constant current mode, for two sizes (5 × 5 and 7 × 7 unit cells) of the stripes lattice (Figure 4.7), and for three different geometries (45° rotated 8 × 8, 8 × 8, and 11 × 11 unit cells) of the checkerboard lattice (Figure 4.8).

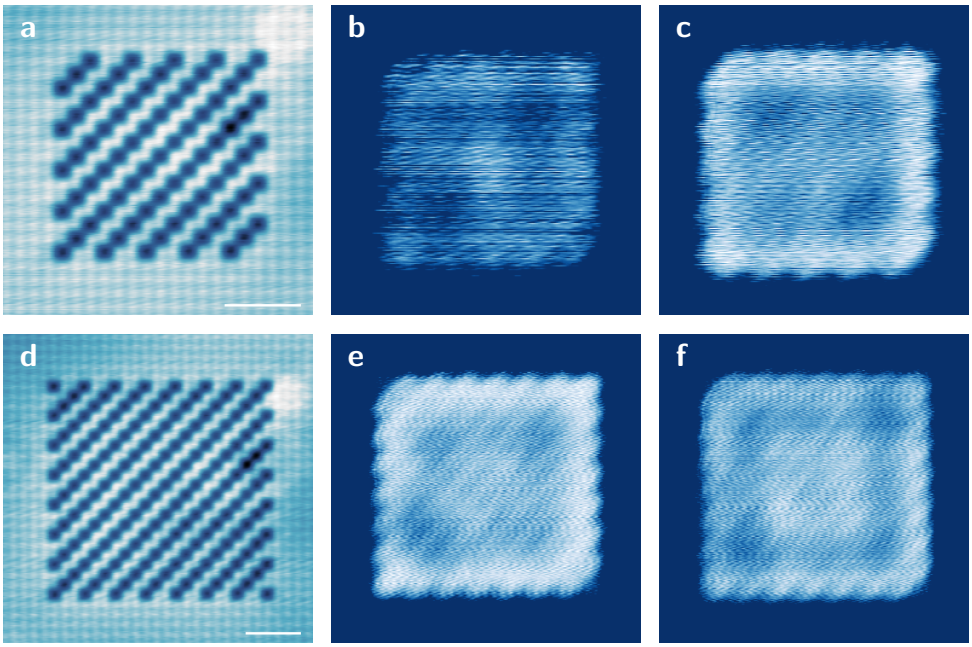

Figure 4.7: **The two stripes lattices, of vacancy density x=0.33. a**, A 15 × 15 lattice site array, with 5 × 5 unit cells, and dz/dV maps at 2.97 and 3.17 V, showing the the $N = 3$ mode anti-nodes shifting outward with increasing energy. **b**, A 22 × 22 lattice site array, with 7 × 7 unit cells, and dz/dV maps at 2.84 and 3.01 V, showing the the $N = 3$ and $N = 4$ modes, respectively. Scale bars are 2 nm.

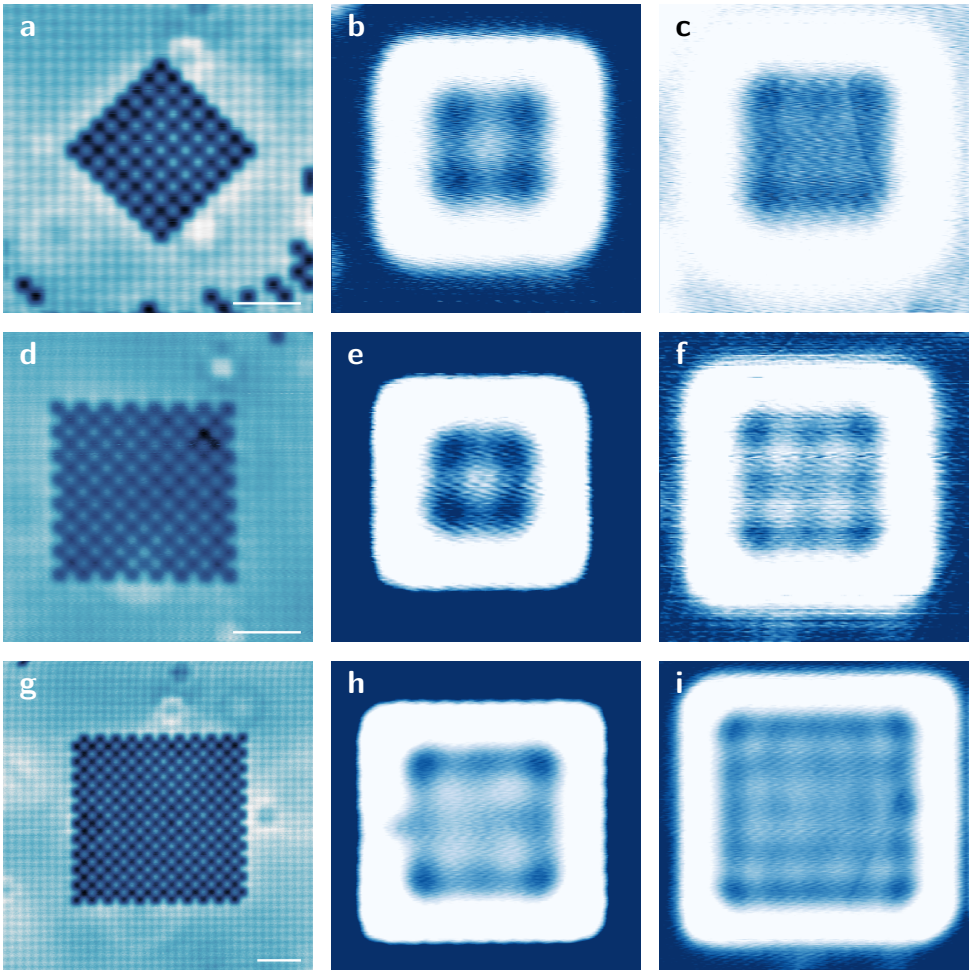

Figure 4.8: **The various checkerboard lattices, of vacancy density x=0.50. a**, A 45° rotated lattice of size 8 × 8, with rotated dz/dV maps of the $N = 3$ and $N = 4$ modes at 2.97 and 3.17 V, respectively. **b**, Array of 15 × 15 lattice sites, or 8 × 8 unit cells, with dz/dV maps of the $N = 3$ and $N = 4$ modes at 2.83 and 2.97 V, respectively. **c**, Array of 22 × 22 lattice sites, or 11 × 11 unit cells, with a dz/dV maps of the $N = 4$ and $N = 6$ modes at 2.84 and 3.01 V, respectively. Scale bars are 2 nm.

5

ARTIFICIAL MOLECULES

The vacancy states in a chlorinated copper (100) surface can couple together when placed in certain relative positions. We explore the strength of this coupling for various orientations and distances between sets of two vacancies, dimers, in light of the tight-binding model. Using this coupling, we construct several structures where the geometry and coupling represents that of an acene molecule. We perform scanning tunnelling spectroscopy on these 'artifical molecules' in order to find the band structure, and the closing and opening of the optical gap as a function of the chain length, as was predicted by Korytar et al. [113]. Tight-binding simulations lead to a quantitative comparison with measurements on three different configurations with increasing coupling strength. The effect, however, is not found, as it is thought to lie beneath our detection limit.

WITH vacancies in a chlorinated copper (100)-surface having a state around 3.5 V [42], it is predicted that multiple vacancies can couple together, when placed in close proximity of each other, thus making structures where a tight-binding approximation can be applied [43, 112]. Following up on the work of Chapter 4, we construct vacancy structures that couple in a similar way as certain molecules, the class of polyacenes. These are molecules consisting of linearly fused benzene rings that are very difficult to synthesize with more than six rings [8, 114]. We replicate polyacenes of different lengths and with different couplings, to find out if we can measure the closing and reopening of the optical gap as a function of the length, as predicted by Korytar et al. [113].

5.1. TIGHT-BINDING MODEL

For sufficiently large crystals, the energy bands for the electrons can be approximated by the free electron model, but when the crystal is small, this model no longer holds. Using a bottom-up approach, we expand upon the overlap between electron states that are bound to neighbouring lattice sites, the tight-binding method [115, 116].

For simplicity, consider a one-dimensional lattice, with the wave function of a bound electron state on the n^{th} lattice site $|\phi_n\rangle$, such that the total wave function over the entire lattice is

$$|\psi\rangle = \sum_{n=1}^{N} c_n |\phi_n\rangle \tag{5.1}$$

with N the number of lattice sites. Inserting this into the Schrödinger equation, we get

$$\hat{H}|\psi\rangle = E(k)|\psi\rangle \tag{5.2}$$

If we consider only nearest-neighbour interactions with a coupling t, the Hamiltonian acting on $|\phi_n\rangle$ will be

$$\hat{H}|\phi_n\rangle = E_n \sum_{n=1}^{N} c_n |\phi_n\rangle = E_0|\phi_n\rangle - t\left(|\phi_{n-1}\rangle + |\phi_{n+1}\rangle\right) \tag{5.3}$$

To satisfy the Bloch condition demands that the eigenstates of the Hamiltonian are periodic in the boundary condition, $|\phi_{n+m}\rangle = e^{ikm}|\phi_n\rangle$, with m any integer. We can substitute this into the Schrödinger equation:

$$\begin{aligned}
\hat{H}|\psi\rangle &= E|\phi_n\rangle && (5.4)\\
&= E_n \sum_{n=1}^{N} c_n |\phi_n\rangle && (5.5)\\
&= E_0|\phi_n\rangle + t\left(|\phi_{n-1}\rangle + |\phi_{n+1}\rangle\right) && (5.6)\\
e^{ikn}\hat{H}|\phi_n\rangle &= e^{ikn}E_0|\phi_n\rangle + t\left(e^{ik(n-1)}|\phi_n\rangle + e^{ik(n+1)}|\phi_n\rangle\right) && (5.7)\\
\hat{H}|\phi_n\rangle &= E_0|\phi_n\rangle + t\left(e^{-ik}|\phi_n\rangle + e^{ik}|\phi_n\rangle\right) && (5.8)\\
&= E_0|\phi_n\rangle + 2t\cos(k)|\phi_n\rangle && (5.9)
\end{aligned}$$

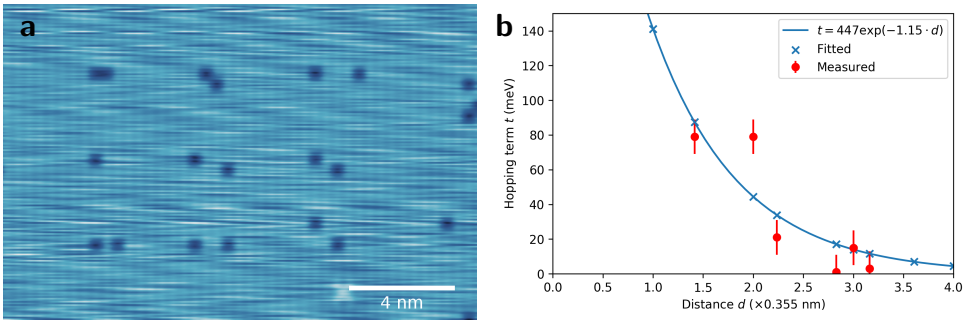

Figure 5.1: **The various dimers for which the coupling has been measured. a**, STM topography of the dimers consisting of vacancies of varying distances. **b**, Measured coupling t as a function of vacancy-vacancy distance d (in units of lattice spacing $a = 0.355$ nm), in red; and the exponential fit through these points in blue.

This gives us the dispersion relation $E(k) = E_0 + 2t\cos(k)$ for a 1D lattice.

This can be expanded to a two-dimensional lattice, such as the graphene lattice. The graphene lattice has two atoms per unit cell, and if we only count nearest-neighbour interactions, each atom 'feels' only its three neighbours. For large amounts of atoms, the Hamiltonian matrix will become large [117]. We are mainly interested in polyacenes, essentially graphene nanoribbons of one benzene ring wide, for which we will use the Python package `pybinding` [118] that uses the tight-binding model to calculate the dispersion, the density of states (DOS) and even the local density of states (LDOS).

5.2. COUPLING BETWEEN DIMERS

According to Drost et al. [112], the vacancy states, as seen in Chapter 4, can couple together to form a tightly bound bonding/anti-bonding pair. The coupling t between the two states depends on the exact relative configuration, where the bonding state is shifted down in energy by an amount t, and the anti-bonding state is shifted up by the same amount, with the Hamiltonian:

$$\mathcal{H} = \sum_{i,j} t_{ij} c_j^\dagger c_i \tag{5.10}$$

The coupling t is half the energy difference Δ between the bonding and anti-bonding states, the two lowest-energy states in the tight-binding model. The anti-symmetric wave-function $|\Psi_-\rangle = |\psi\rangle - |\psi_2\rangle$ crosses zero in-between the two vacancies, so its probability density distribution is localized more on the outsides of the structure, while the symmetric wave-function $|\Psi_+\rangle = |\psi\rangle + |\psi_2\rangle$is localized in-between the two vacancies. By comparing the energies of the peak in the differential conductance spectrum, the $\mathrm{d}I/\mathrm{d}V(V)$ curve, we can extract $\Delta = E_{ab} - E_b = 2t$ and thus find the coupling t between the two vacancies. This approach gives a value for the coupling t for each dimer configuration.

At a background spectrum on a chlorine atom, i.e. at least four unit cells away from a vacancy, the onset of the conduction band is at 3.5 V, where a plateau with some small peaks continues at higher voltage. The state of a single vacancy is at 3.46 V, so for a dimer, we expect the bonding and anti-bonding state to be centred around that value.

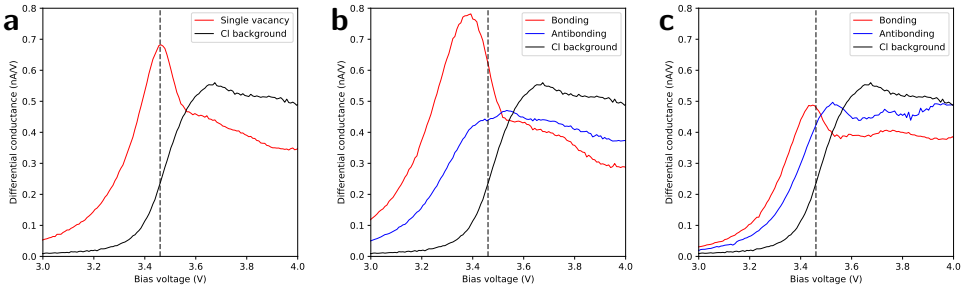

Figure 5.2: **Differential conductance spectra, a**, taken at a single vacancy, **(b)**, a {1,1} dimer, and **(c)**, a {3,0} dimer. The height was determined for 500 pA at 4.5 V, and kept constant during the measurement. The dI/dV spectrum at the single vacancy (a, red), has a peak at 3.46 V (dashed line in b and c). The spectrum at the chlorine background, far from any vacancy, is also plotted in b an c. The bonding spectrum (red) is taken in the middle between the two vacancies, and the anti-bonding spectrum (blue) ~1 lattice constant outside the dimer.

5

The bonding state is expected to move to lower voltages with increasing coupling, which will make it well visible over the low conduction background, but the anti-bonding state would move to higher energies, which makes it hard to distinguish between an anti-bonding peak and the background. Because the vacancies in the {1,1} and {1,0} dimers are touching, it is hard to make out the precise location of the bonding state, if there is any. Furthermore, the {4,0} dimer does not show any spectra that differ from those of two uncoupled vacancies, so we can assume the coupling there to be negligible.

The dI/dV spectra were measured with a lock-in oscillation amplitude of 10 mV, which determines the systematic error in the state energies, and by extension, in the hopping terms calculated below.

dimer	E_b (eV)	E_{ab} (eV)	$t = \Delta/2$ (meV)	$t = E_v - E_b$ (meV)	t_{fit} (meV)
{1,0}	3.45	3.61	83	-	141
{1,1}	3.38	3.54	80	79	87
{2,0}	3.38	3.63	126	79	44
{2,1}	3.44	3.53	45	21	34
{2,2}	3.46	3.62	79	0	17
{3,0}	3.45	3.51	33	15	14
{3,1}	3.46	3.53	33	0	12

Defining the coupling as half the energy difference for the bonding and antibonding states, the fourth column of the table above is calculated as $t = \Delta/2 = (E_{ab} - E_b)/2$. The values for t_{20} and t_{30} are similar to those reported before, with 35 and 138 meV, respectively [112].

The lower, bonding peak can be resolved for each of the dimers, but the higher, anti-bonding peak is hard to distinguish from the features already present in the background spectra, and it is less localised than the bonding peak because its location is not confined to within the two vacancies. This means that the uncertainty of the anti-bonding state energies is of the order of tens of millivolts higher than for the bonding states.

Taking only well-defined peaks into account, we can also define t as the energy shift from the vacancy state at $E_v = 3.46$ eV to the bonding state energy E_b. These values are shown in the fifth column in the table above. In doing so, we assume that the bonding and anti-bonding states move an equal amount t down and up in energy from the individual vacancy state energy, 3.46 eV. An exponential dependence on vacancy-vacancy distance has been fitted through these values, as shown in Figure 5.1. This fit allows us to predict the values for $t_{10} = 141$ meV and $t_{11} = 87$ meV, which are needed for the tight binding calculations of polyacene structures.

It does appear, however, that the two peaks are not equally shifted with respect to the energy of the vacancy state peak, e.g. that the energy difference is not centred on E_v for all dimer configurations. This should be attributed mostly to the fact that the peaks at higher energies are more difficult to find, but any underlying additional shift doesn't seem to show a pattern as a function of dimer distance. Even though the earlier method ($t = \Delta/2$) would account for any shift, the latter method of obtaining t only from the peak at lowest energy is deemed the most meaningful, because of the accuracy of the peak energy measurement.

5.3. OPTICAL GAP SIMULATIONS

When the polyacene chain is infinite, the valence and conduction bands cross before the end of the Brioullin zone, if the third nearest neighbour hopping t_{nnnn} is taken into account [113, 119]. To find the optical gap, we have two approaches: measure the energy difference between highest occupied molecular orbital (HOMO) and lowest unoccupied molecular orbital (LUMO) at $\tilde{k}^{(N)}$, the allowed k-value closest to the Dirac point k_D; or calculate the density of states (DOS) for each molecule, then take the difference between the two peaks around zero energy. It is also possible to find the optical gap from density functional theory (DFT) calculations, which is the method used by Korytar et al. [113], but this method is not employed in this chapter.

ALLOWED k-VALUES

The band structure is continuous for an infinite lattice, i.e. the limit of $L \to \infty$. If we restrict the size L of the lattice, however, we allow only those values for the crystal momentum of $k = 2\pi n/L$, where $n \in \mathbb{N}$, and with $2\pi/a$ the largest allowed k-value, where a is the periodicity or lattice constant.

In the continuous band structure for the polyacenes, the two bands around the Fermi level, the HOMO and LUMO cross at a certain k, and the band gap is zero. But for any practical acene chain, there is a finite number of k's, and the HOMO and LUMO might not necessarily cross. Taking only those allowed k-values into account, the smallest energy difference between the HOMO and LUMO is the band gap. By plotting it as a function of the number of chains, one can see that it oscillates, cf. [113].

CALCULATING THE LDOS FROM TIGHT-BINDING THEORY

The Python package `pybinding` was used to calculate the band structure of a polyacene chain of length N [118]. A Green's function method was then used to find the DOS of the structure as a whole, and the local density of states (LDOS) on each different vacancy.

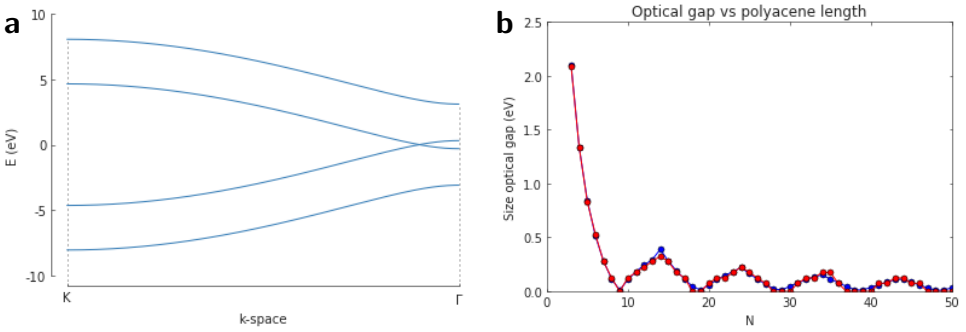

Figure 5.3: **Band structure and optical gap oscillation. a**, Band structure for an infinite polyacene molecule. **b**, Optical gap oscillation computed in 2 ways: by using the tight-binding method (blue), and with the allowed k-values method (red).

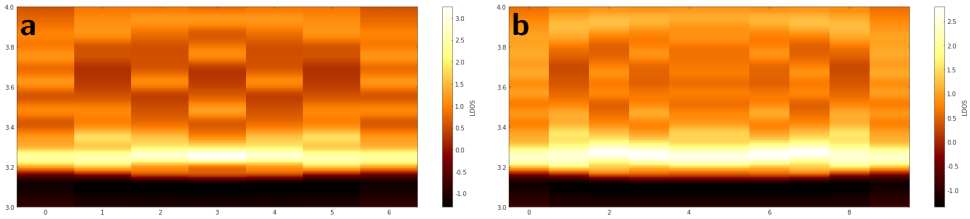

Figure 5.4: **Simulated local density of states (LDOS)**, on the outer atoms of a chain of length **(a)** $N = 7$, and **(b)** $N = 10$. y-axis is energy in eV, shifted up so 3.5 eV is the effective 'zero', x-axis the position along the chain, and the color scale is the LDOS (a.u.).

First, the band structure of an infinite polyacene molecule is calculated with the parameters of the actual carbon-based molecule, as shown in Figure 5.3a. The optical gap oscillation, with increasing k, as calculated from the tight-binding method, is compared to the gap oscillation calculated with the allowed k-value using the infinite chain band structure. As can be seen in Figure 5.3b, they resemble each other very much, so from now on, the allowed k-values method is used to calculate intensity and periodicity of the gap oscillations.

The LDOS was calculated on the outer atoms (those not forming the connection between two rings) of the chain of length N, as plotted in Figure 5.4. When the coupling parameters of our copper chloride system are used, the optical gap oscillation becomes much weaker compared to the carbon-based acene molecules, by an order of magnitude. The LDOS is normally centred around zero energy, but because our vacancy state is at 3.5 eV, all values are shifted to account for that offset. A thermal broadening of 20 meV is applied, in order to try to better resemble the measured data, but still leaving the individual peaks visible.

As can be seen, we expect the largest contribution to the density of states at lower energies, around 3.25 V, almost equally bright for all outer atom positions along the chain. In the middle of the chain, we see some patterns emerge at slightly higher energy, 3.5-3.8 V for individual states that are far apart in energy in the centre ring, but approach

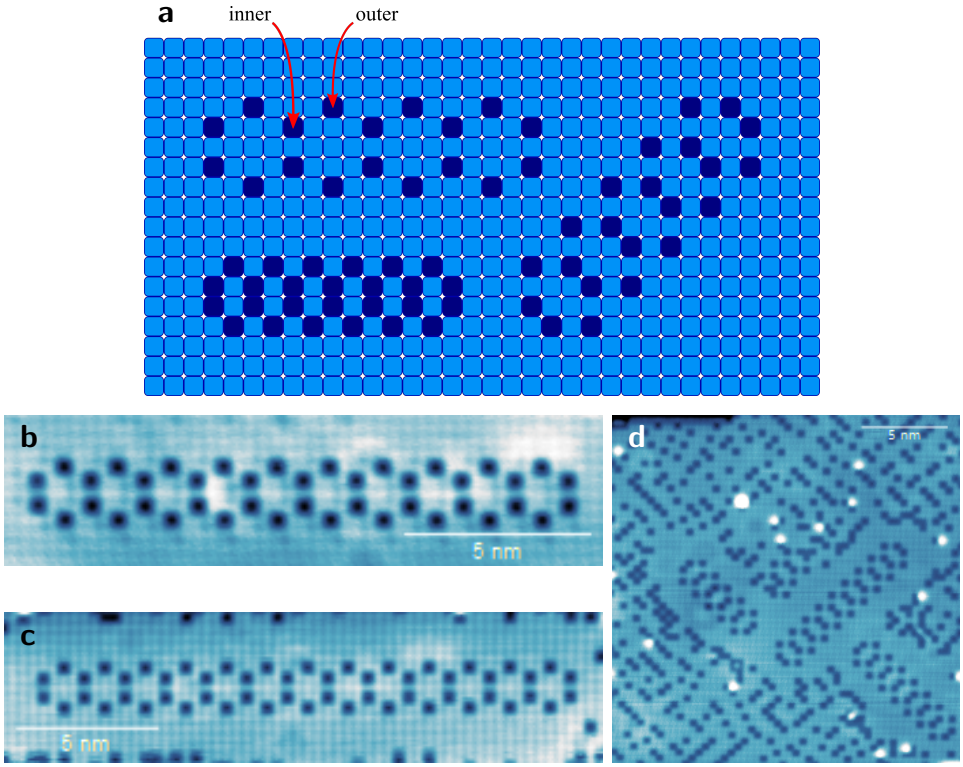

Figure 5.5: **The three different acene types.** **a**, Sketch of the three types, with different couplings. 'Inner' vacancies are those that connect two hexagons, 'outer' vacancies are part of only one. STM topography of **b**, a decacene, and **c**, a tridecacene with t_{21} and t_{20} couplings. **d**, STM topography of the slightly denser acene type with t_{20} and t_{11} couplings. Shown here are a pentacene (5 rings), a heptacene (7) and a nonacene (9).

each other to ~ 3.6 eV when moving outwards along the chain.

An open gap should correspond to a non-zero difference of the two lowest-energy states, and the closing of the gap would be shown with the two lowest states on either side of zero converging to zero (or 3.5 eV).

5.4. BAND STRUCTURE IN LONG ACENES

We made polyacene chains of the three types shown in Figure 5.5. The vacancies making up the 'molecule' can be divided in two classes, we call those that connect two neighbouring rings the 'inner', and those in between the 'outer' vacancies. Taking $\mathrm{d}I/\mathrm{d}V$ spectra along the vacancies, we hope to see a signature of band structure in our density of states (DOS). Because the state in a single vacancy is at 3.5 V, we expect to see the features that would relate to the polyacene band structure around that energy.

The closer the vacancies are together, the higher the coupling between them: the least dense configuration has t_{21} and t_{20} couplings between nearest-neighbour vacancies, and the diagonal configuration has t_{20} and t_{11} couplings, which are both much

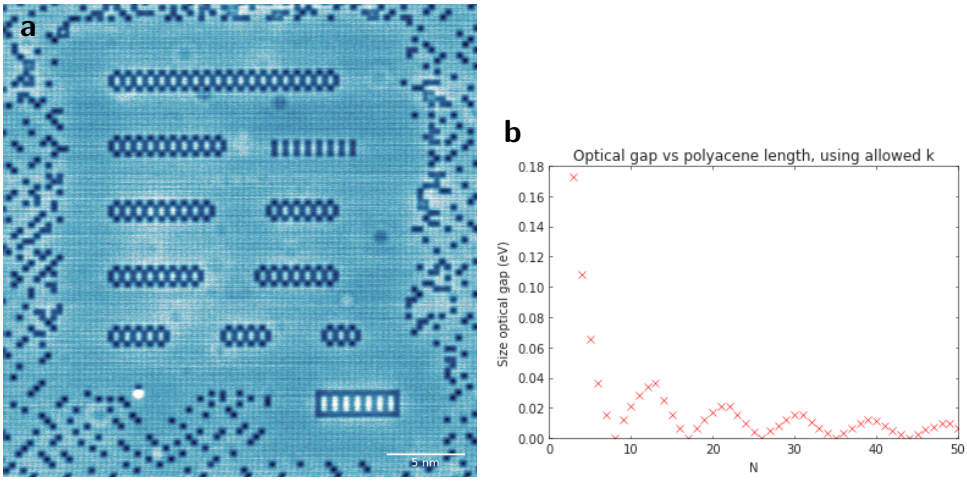

Figure 5.6: **Acene structures of the densest kind, with t_{11} and t_{10} couplings. a**, Chains of lengths 3 through 10, as well as a $N = 20$ chain and two 'gratings' of length $N = 7$. **b**, Simulation of the optical gap oscillation for these chains. The gap is expected to close at $N = 9$ and to be maximum at $N \leq 7$ and $N = 13$, where $E_g \geq 36$ meV.

5

smaller than the t_{11} and t_{10} couplings of the densest configuration. The calculation of the band structure for an infinite chain with these couplings predicts a gap of 36 meV for the first oscillation, i.e. for $N = 13$, while for the two less dense arrangements the gap would be 9 and 7 meV, respectively. Because this is comparable to the energy resolution of our signal, only in the densest polyacene configuration it might be possible to tell from our spectra if there is a gap oscillation as function of the chain length.

CHAIN LENGTH DEPENDENCE

The third configuration in Figure 5.5a is the densest that we made. The vacancies in the the inner positions, the vertical dimers, are already bordering each other on one side, so it can be questioned if these still have separate states. The couplings in this arrangement have the highest couplings of all possible dimer configurations, as t_{10} and t_{11} are fitted to be 141 and 87 meV, as in Figure 5.1. For any denser arrangement, the vacancies will surely be too closely packed for separate states to exist. Also, the hexagonal symmetry of the molecule can then no longer be replicated in the square lattice geometry of the $Cu_2Cl/Cu(100)$ surface.

The calculations in Figure 5.6 show that for this configuration, we would expect the optical gap to be open for $N \leq 7$, where it is larger than 10 meV, closed for $N = 8$ and again open around $N = 13$. We have built acenes of all lengths N=3-10, and N=20. Spectra were taken along line cuts through the inner and outer positions.

The line spectra in Figure 5.7 show a periodic oscillation in x, but this seems – as far as we can discern – entirely due to the fact that they are taken on a line crossing the outer vacancies, with three $\mathrm{d}I/\mathrm{d}V$ spectra taken per lattice constant $a = 0.36$ nm. The vertical stripes indeed have a periodicity of six spectra, as the outer vacancies are $2a$ apart. The simulations suggest that the gap opening and closing should be most visible in the center

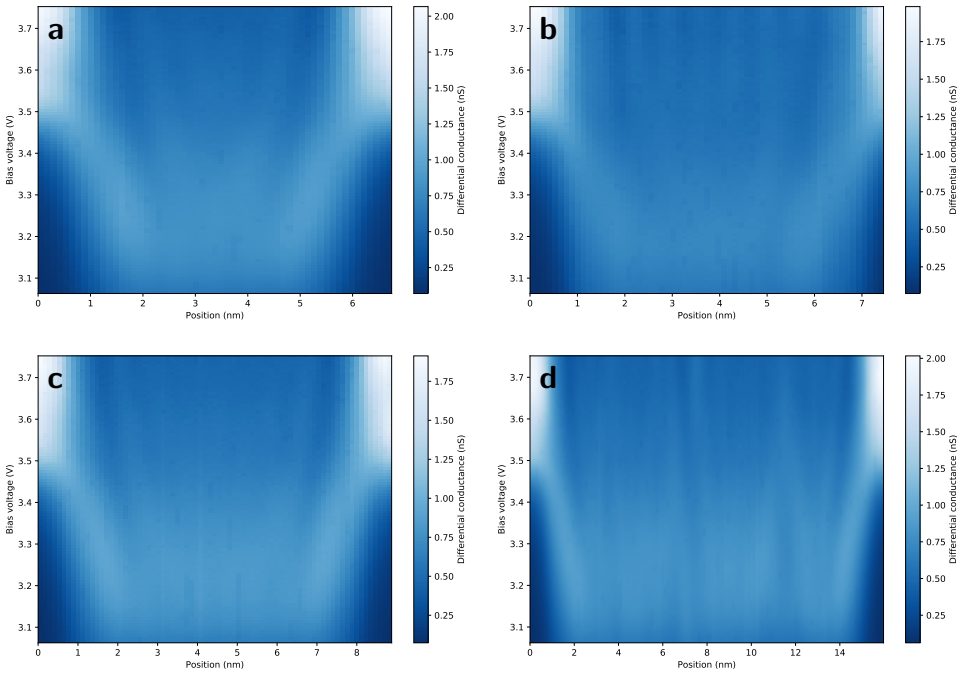

Figure 5.7: **Spatial differential conductance spectra.** $\mathrm{d}I/\mathrm{d}V$ spectra along a line cut through the outer vacancies of **(a)** the 7-ring heptacene, **(b)** the 8-ring octacene, **(c)** the 10-ring decacene, and **(d)** the 20-ring icosacene. Bias voltage from 3.06 to 3.75 V, with a constant tip height set for 1.2 nA at 3.75 V.

outer vacancy, where a pair of states should be centred around 3.5 V. No peaks in the in differential conductance can be discerned around 3.5 V, regardless of the position.

The simulations also predict a state at around 3.25 eV for all positions, with the spectra at the centre ring looking slightly different than the two rings around it. Unfortunately, in these line spectra plots, we don't see any features resembling the predictions.

5.5. CONCLUSIONS

As a single vacancy exhibits a peak in the differential conductance around 3.5 eV, it is proposed to position multiple vacancies close together in order to couple their states in a tight-binding manner. Dimers have been created, of pairs of vacancies in a variety of specific configurations between 1 and 4 lattice constants apart. Spectra have been obtained along a line through these pairs, where a bonding and anti-bonding state have been predicted to emerge inside and outside the vacancies, respectively [112].

We obtained the hopping term $t = \Delta/2$ from these spectra, where Δ is the difference in energy between the bonding and anti-bonding peaks in the spectra. For smaller distances, the shift in the peaks is larger, and it becomes much more difficult to reliably obtain the anti-bonding peak, which is at higher energy, as it is obscured by the peaks and features already present in the spectrum above 3.6 V. Using only the bonding peak,

at lower energy, the couplings that are calculated are of the same order of magnitude as before, but behave more like an exponential dependence on the dimer separation. A fit through these values for the coupling t gave the predictions on which the optical gap simulations are based.

Making structures of coupled vacancies allows us to describe the tight-binding band properties of the total structure. Organic polyacene molecules of various lengths are replicated in three different vacancy configurations, where we expect the optical band gap to close and open as a function of the chain length [113]. Tight-binding calculations of the structures predict a band gap for certain lengths in the order of tens of meV for the densest configuration, which has the strongest coupling that can be achieved in this system.

Two-dimensional line cuts through the chains, however, don't reveal any features in the DOS that resemble our simulations, even when comparing all lengths from $N = 3$ to 10, and $N = 20$. The proposed signal (36 meV) is in the order of our detection limit (10 meV), and even though we operate at low temperatures and with low noise, it is not possible to resolve the gap oscillations that were predicted.

It is possible that the couplings that were measured and calculated in Section 5.2 are an overestimation of their actual values, if the vacancies indeed couple in a tight-binding way, and that consequently the gap is smaller than expected. In that case, even if we manage to increase the energy resolution and sensitivity of our measurement, it might not yet be possible to see the oscillation. This chlorine terminated copper (100) substrate is therefore unlikely to be a good substrate for building artificial molecules, but similar surfaces with a different termination, e.g. bromine or iodine on copper, that also exhibit vacancies, might be better candidates for this endeavour.

6

MEASURING THE LOCAL ELECTRIC FIELD WITH STM

Resonances in differential conductance spectra are observed when measured on the chlorinated copper (100) substrate, sometimes leading to negative differential conductance. These are explained with the presence of a quantum dot on the apex of the scanning tunnelling microscope (STM) tip, that is sensitive to the local electric field. These resonances shift to lower energies with decreasing tip height, indicating a dependence on the capacitive electric field of tip and sample. They also shift when the tip is brought over a vacancy in the copper chlorine substrate. We investigate the resonance behaviour for various vacancy structures with non-uniform electric field, and compare it to image charge simulations of point charges on a perfect conductor. A qualitative agreement is found when taking into account only the vertical electric field. When multiple resonances occur, it is possible to estimate the relative distance between the quantum dots in all three directions. We compare the resonance behaviour when the tip is positioned above the chlorine background and above the centre of a large copper patch in order to differentiate between the tip and sample electric field contributions. Reconstructing the total experienced electric field on known surface geometries can lead to a way of determining the exact sample electric field, possibly opening the door to novel ways of scanning probe microscopy.

This chapter forms the basis for a future publication by D. Coffey Blanco et al.

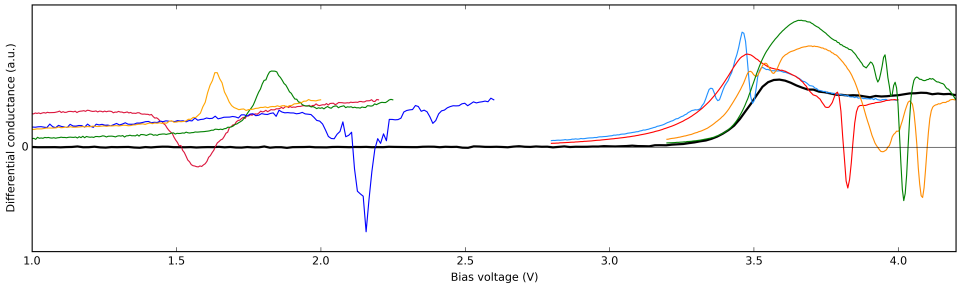

Figure 6.1: **Various of the resonances encountered in this study.** Some of the resonances appear as peaks or dips, others as multiple peaks or dips together, in the [1.0,4.2] V range. Differential conductance curves are normalised to either the maximum or the value at highest bias voltage. In black, a reference spectrum on the chlorine background is shown, without a resonance on the spectrum.

6.1. INTRODUCTION

On occasion, features with negative differential conductance (NDR) can be observed in the $\mathrm{d}I/\mathrm{d}V$ spectrum, when measuring a differential conductance spectrum on the copper chloride surface, after indenting the STM tip into the surface. These features are (sets of) peaks and/or dips that deviate from the normal $\mathrm{d}I/\mathrm{d}V$ curve, at various bias voltages (Figure 6.1). When comparing spectra taken at different positions over a vacancy structure, the voltage of the resonance is seen to shift to different values of V_R. This dependence on the local environment, as well as on the tip height, suggests that the resonances are sensitive to the local electric field. We speculate that a chlorine atom (or a cluster thereof) forms a weakly coupled quantum dot on the tip apex, thus being sensitive to the local electric field it experiences. In this chapter, we examine this model in order to explain the observed behaviour.

During controlled tip indentation in the $Cu_2Cl/Cu(100)$ sample, we probably picked up a chlorine atom behaving as a quantum dot. When taking a differential conductance spectrum on a uniform chlorine background, a resonance occurs at a certain value, e.g. 1.5 or 4.1 V. This resonance is shifted to different voltages when the tip is positioned over a vacancy or a structure made of multiple vacancies, where the surface exhibits a locally non-uniform charge distribution, due to the charge transfer from the Cu to the Cl atoms [51, 53, 86]. The resonance voltage V_R also changes with current set-point, implying that the height-dependent electric field is an important factor influencing the quantum dot.

A number of resonances encountered in this investigation is shown in Figure 6.1. Some shapes are smooth peaks or troughs, but others have both a peak and a dip in conjunction with each other, while some seem to consist of a dip with multiple satellite troughs, forming a jagged shape. On occasion, the dips go into negative differential resistance, representing not an actual negative density of states (DOS), but a resonant state of the quantum dot, featured on top of the local density of states (LDOS). The various resonances resemble that of other studies where the charging of molecules, a negative differential resistance, or a tuneable magnetoresistance is studied [120–125], leading to the hypothesis that a quantum dot is attached to the tip apex.

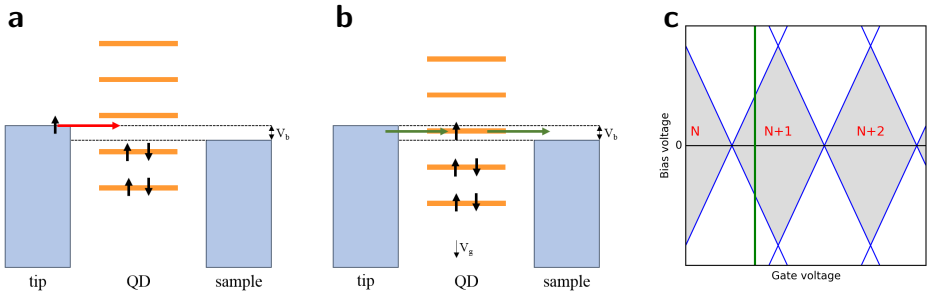

Figure 6.2: **Energy diagram and Coulomb diamonds of a quantum dot between two leads. a,** An electron from the filled states on the tip cannot tunnel to the empty states on the sample, because there is no quantum dot state in the bias window V_b. Vertical axis is energy. **b,** When the QD is shifted in energy, by gating it with voltage V_g, some of its states may move into the bias window, allowing electrons to tunnel from the tip to the QD, and then to the sample. **c,** When plotting the differential conductance as function of bias and gate voltage, each of the transitions are given by the blue lines, forming Coulomb diamonds. A tunnelling (or QD charging) event happens when either the bias voltage window is large enough, or the gate electrostatically moves a quantum dot state into the bias window. In the shaded regions, no tunnelling is allowed due to Coulomb blockade, and the QD has exactly $N+i$ electrons. A typical differential conductance spectrum in STM is done along a line with constant gate voltage, by only changing the bias voltage, as shown by the green line.

A quantum dot (QD) is an object, a molecule or a fabricated nanostructure, that has bound, discrete electronic states [126–128]. These discrete states can lead to excited electrons emitting light of a tunable wavelength, as evidenced by the large interest by the consumer industry for e.g. Quantum Dot television screens [128]. Here, we focus on the possibility of shifting the states when applying an external electric field.

An important feature in quantum dots is Coulomb blockade. This is the effect that prevents an electron from tunnelling through the QD, because the (Coulomb) charging energy of adding another charge to it is larger than the applied bias voltage. When the bias voltage exceeds this charging energy, electrons can tunnel into the QD state, raising the number of electrons from N to $N+1$. If a gate locally applies a voltage (i.e. an electric potential) to the QD, its states shift in energy. This can cause a state that was outside the bias window to move into the bias window, thus also allowing electrons to tunnel into the dot, moving it to the $N+1$ state, and thus temporarily lifting the blockade. Adding an extra electron, however, is still problematic, because the next state $N+2$ is still out of reach, and either a higher bias voltage or a higher gate voltage is required. Plotting the allowed transitions as a function of both gate and bias voltage (V_G and V_b), this looks like a series of diamonds, called Coulomb diamonds, see Figure 6.2 [115, 129].

In transport measurements of e.g. molecules or nano-fabricated quantum dots, one typically can change the chemical potential of the dot by gating it with an electrode nearby that shifts the levels of the quantum dot so that they are near the Fermi energy or within the bias window of source and drain. With STM, this is typically not possible, because only two electrodes exist there: the tip and sample act as the source and drain, but in most designs there is no room for a gate to influence the atom, molecule or structure.

Scanning Quantum Dot Microscopy (SQDM) uses a quantum dot that is attached to the tip apex to directly probe the local electrostatic potential. In this method, Wag-

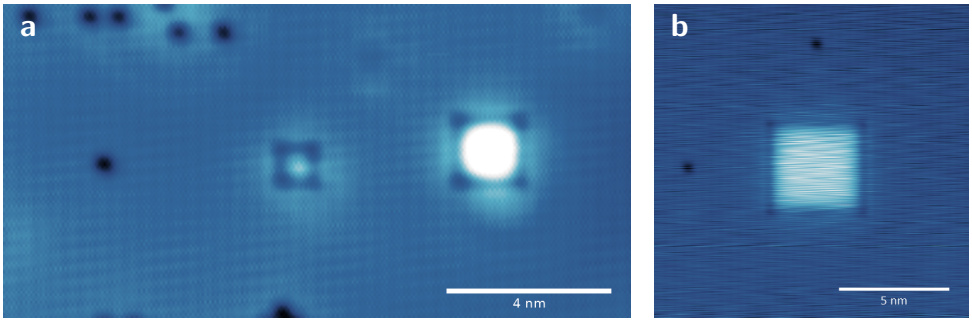

Figure 6.3: **Topography images** of **(a)**, 1×1, 3×3, 5×5, and **(b)**, a 11×11 vacancy patch. For arrangements where multiple vacancies are next to each other, the image appears brighter there, because the copper underneath is more conductive than the chlorinated copper surface.

ner et al. [130] pick up a quantum dot with known behaviour, the molecule naphtalene tetracarboxylic dianhydride, so that it is attached to the apex of the tip. This QD has a weak coupling to both tip and sample because of the weak orbital amplitude at the corner oxygens. This results in very sharp line widths and the "possibility to gate these levels because a sizeable fraction of the applied bias voltage drops over the insulating oxygen-tip bond" [130]. Another way to measure the local potential of a sample is via the electrostatic force, measured by Kelvin Probe Force Microscopy (KPFM) [9–11]. In a similar manner, it is in certain cases also possible to use the STM or AFM tip as a gate, in order to control the charge in molecules or quantum dots [120–123, 131].

In our case, we scan the quantum dot over a charge distribution in the surface, which means that the electrostatic potential varies locally, and this changes the levels in the QD. This is a way of gating the QD, so that resonant levels are now at different energies with respect to the Fermi energy. This means that their signatures will occur at different applied bias voltages [122, 130], just as we see the resonance voltages shift with varying surface geometry and tip heights.

6.2. DEPENDENCE ON THE LOCAL ENVIRONMENT

To examine the nature of the resonances occurring in the differential conductance spectra, we perform a number of different experiments with a quantum dot on the tip apex. We construct various vacancy structures in the Cu_2Cl surface, to find out how the local geometry and the surface charge distribution, i.e. the local electric field as experienced by the quantum dot, affect the observed resonances. Furthermore, the resonance behaviour as a function of tip-sample distance is explored, by way of increasing the tunnel current during $\mathrm{d}I/\mathrm{d}V$ measurements.

6.2.1. VACANCY STRUCTURES

We scan the tip over structures with vacancies assembled in $N \times N$ square patches, with $N \in \{1,3,5,7,11\}$ (Figure 6.3), and notice that when the tip is over a vacancy, a resonance shifts to a lower voltage V_R than when it is over the chlorinated background.

Taking $\mathrm{d}I/\mathrm{d}V$ spectra along a line through the patch, with 5 spectra taken per lattice

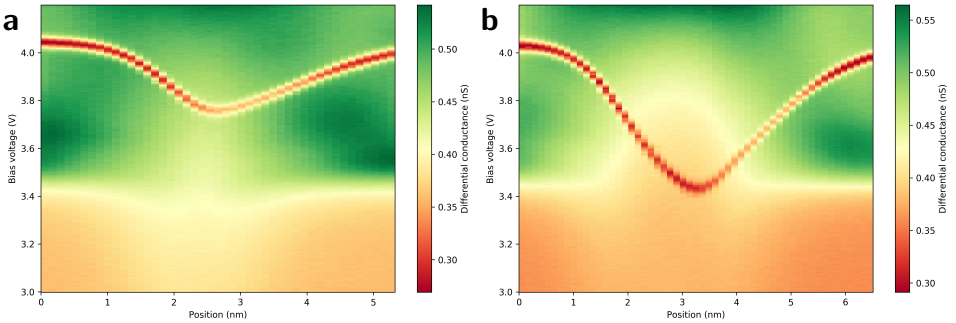

Figure 6.4: **Differential conductance spectra for line cuts over a patch of copper.** The resonance voltage shifts from higher than 4.0 V (outside) to **(a)** below 3.8 V in the centre of a 3×3 vacancy patch, **(b)** and almost to 3.4 V in the centre of a 5×5 patch. The $\mathrm{d}I/\mathrm{d}V$ spectra were taken along a line from $3a$ on either side of the square vacancy patch, with 5 spectra per unit cell, with the height determined by 200 pA set-point current at 4.2 V.

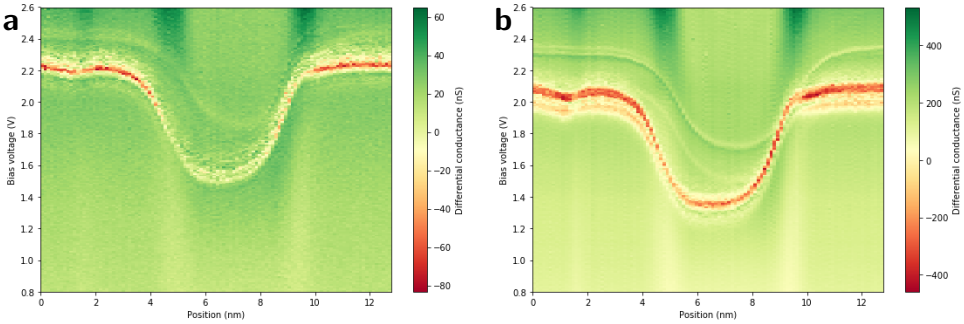

Figure 6.5: **Differential conductance spectra along a line cut through a** 11×11 **patch of copper.** The spectra were taken at a height determined with a set-point current of (**a**) 50 pA and (**b**) 500 pA at 2.6 V. Note that a second resonance is visible at a slightly higher voltage, and shifted a bit to the right. This is discussed in Section 6.4. More line cuts are shown in Figure 6.12

constant $a = 0.355$ nm, we see that V_R shifts farther down in energy when the patch is larger, as can be seen in Figure 6.4. We see that for small patches, the resonance voltage goes down when the tip moves over the patch, and increases again at the other end of the patch. For larger patches, e.g. $N = 11$ in Figure 6.5, V_R levels off for the internal part of the square patch. This levelling off suggests that the quantum dot on or near our tip apex still feels the chlorine atoms that form the edge of the surface when the apex is located within $\sim 2a$ of the edge, while in the center V_R is again constant, like on the Cl background.

6.2.2. CURRENT DEPENDENCE

As can be seen in Equation (4.1), the tunnel current is proportional to the applied voltage V, and exponentially dependent on the height z of the tip over the sample:

$$I(z) = AVe^{-2\frac{\sqrt{2m\phi}}{\hbar}z} \tag{6.1}$$

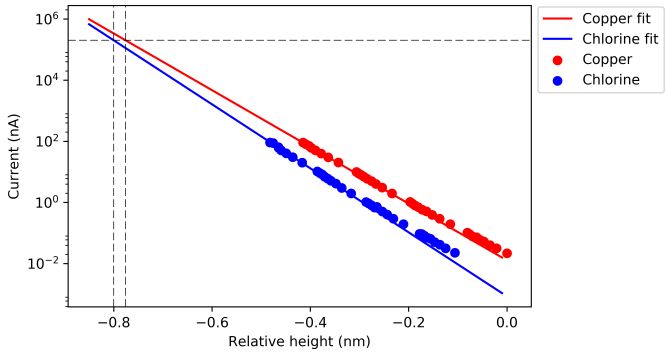

Figure 6.6: **Current dependence on chlorine and on copper.** An $I(z)$ curve was measured on the chlorine background (blue) and in the centre of a 11×11 vacancy patch, i.e. on copper (red). An exponential dependence on tip height was found, and, when extrapolated, the absolute tip height can be determined, by finding the z_0 for which $I = G_0 V = 201$ µA, for 2.6 V. The difference between z_0 for Cu and Cl is 24 pm.

with A a constant, m the mass of the tunnelling electron, ϕ the height of the the tunnelling barrier, or work function, and $\hbar$ the reduced Planck constant. When taking a $\mathrm{d}I/\mathrm{d}V$ spectrum, the height is kept constant while sweeping the bias voltage, and the resulting signal is proportional to the density of states.

The line cuts over the centre of an 11×11 patch of copper, shown in Figure 6.5, were taken with different current set-points (50 pA to 500 pA). This factor ten increase in current corresponds to a ~1 Å difference in height. We can see that – at this lower height – the resonance of the quantum dot has shifted by sometimes more than 0.1 V. Line cuts for 50, 100, 200, and 500 pA in two directions over the vacancy patch are shown in Figure 6.12.

To determine the absolute height of the tip above the surface, we take $z = 0$ when the tip is in contact with the topmost atoms. We define contact as the height where the conductance is determined solely by a single quantum channel (or two, for spin up and down), i.e. when the quantum of conductance $G_0 = 2e^2/h = 7.748{\cdot}10^{-5}$ S is reached. This is equivalent to a tunnel junction resistance of $R = 1/G_0 = 12.9$ kΩ.

When plotting an $I(z)$ curve taken at two positions, one in the middle of the copper patch and the other on the chlorine background, we see that the behaviour is indeed exponential (Figure 6.6). Extrapolating the fitted behaviour, we can determine the absolute z_0 as the height where $I = G_0 V = 201$ µA, for 2.6 V. We can use this calibration to determine the absolute height $d(I, V = 2.6\,\mathrm{V}) = z - z_0$ in future measurements.

6.3. ELECTRIC FIELD SIMULATIONS

To verify if the quantum dot on our tip is sensitive to the electric field, and if so, in what manner, we have to simulate the effective applied electric field. We can then compare this simulation to our experiments, to validate our model of a QD on the tip apex. The E-field consists of two parts: the field generated by the tip and that by the sample. The tip electric field comes from applying a bias voltage V to the tip-sample junction, which we can approximate as a capacitor with a plane as one electrode and a sphere or hyper-

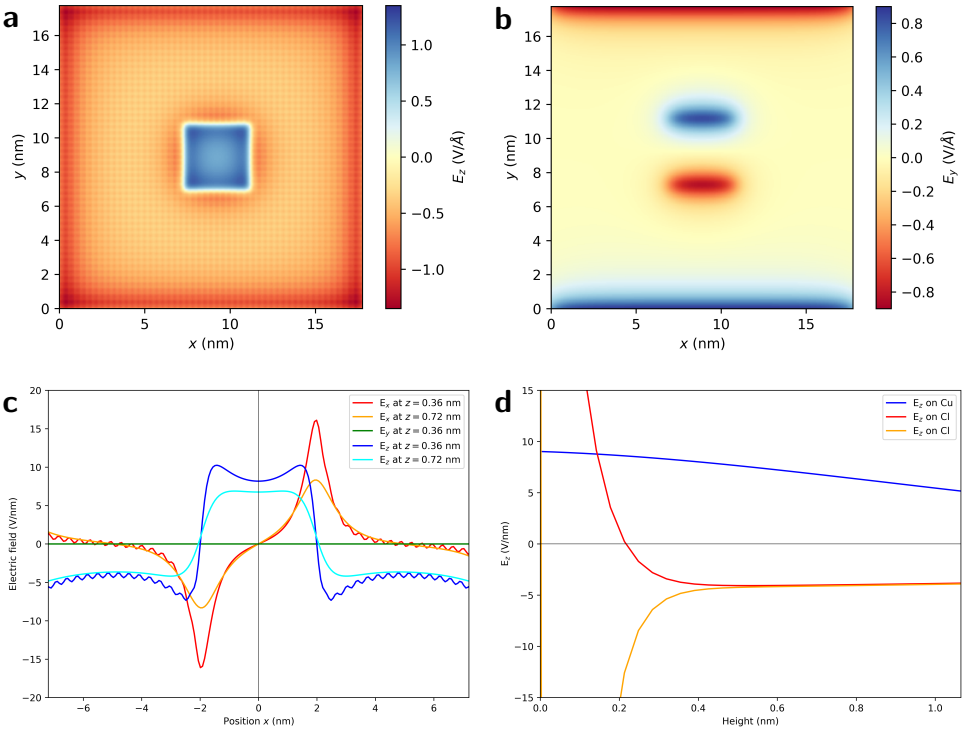

Figure 6.7: **The electric field of an** 11×11 **patch of vacancies in a copper chlorine layer. a**, The vertical component E_z of the electric field due to the sample, at a height $a = 0.36$ nm above the surface. **b**, The horizontal component E_y of the electric field due to the sample, at a height $2a = 0.72$ nm. **c**, The x (red), y (green) and z (blue) components of the electric field on a vertical line through the centre of the 11×11 vacancy patch at a height $a = 0.36$ nm above the chlorine atoms, and the x (orange) and z (cyan) components at height $2a = 0.72$ nm. **d**, E_z as a function of height in the centre of the copper patch (blue) and on the chlorine background far away from any vacancies (red, orange). The red curve starts directly on top of a Cl atom, and the orange in between four Cl atoms. They diverge for very small distances, but converge for heights larger than ~0.4 nm.

boloid with radius of curvature R as the other [132, 133]. The electric field inside is:

$$E = \frac{V}{d} \frac{\sqrt{u(1+u)}}{\ln\left(\sqrt{u} + \sqrt{1+u}\right)} \approx \frac{V}{d} \qquad \text{for } u = \frac{d}{R} \ll 1 \tag{6.2}$$

A large tip radius, typically in the order of $R = 10 - 100$ nm, and a small tip-sample distance $d \leq 1$ nm when in tunnelling range are consistent with approximating the junction as a parallel-plate capacitor, which also gives $E = V/d$.

Because the sample is not homogeneous, it might also generate a non-zero electric field, due to the specific charge configuration present in the sample. Taking each chlorine atom as an ion of charge $q = -e = -1.602 \cdot 10^{-19}$ C, located at height Δz above the copper atoms, we assume that the bulk copper crystal can be treated as a perfect infinite grounded conductor. Using the method of image charges, we can also calculate the electric field of the system by replacing the conductive plane with a charge $-q$ at $z = -\Delta z$ for

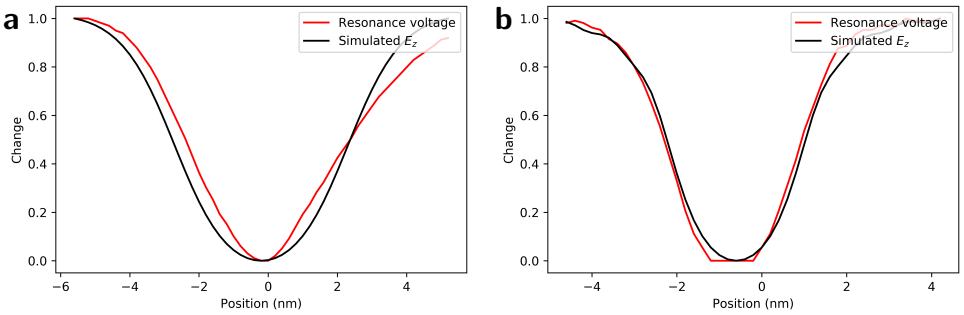

Figure 6.8: **The shape of the resonances for a** 5×5 **and** 3×3 **patch fitted with the simulated electric field. a**, Simulated E_z at height $2.3a = 0.82$ nm (black) and the resonance voltage (red) along a line through the centre of a 5×5 vacancy patch. The correlation coefficient is 96.3 %. **c**, Simulated E_z at height $1.0a = 0.36$ nm (black) and the resonance voltage (red) along a line through the centre of a 3×3 vacancy patch. The correlation coefficient is 99.4 %.

each charge above [134, pp. 121-125]. We take here $\Delta z = a/2 = 1.78$ Å, the vertical distance between the Cl c(2×2) reconstructed layer and the top layer of Cu atoms, as half the lattice constant $a = 3.55$ Å, which is the horizontal distance between two chlorine atoms in the monolayer [52]. The contribution of each charge i to the electric field at a position $\vec{r}$ is then given by

$$\vec{E}_i(\vec{r}) = \frac{1}{4\pi\epsilon_0} \frac{q_i}{R^2} \frac{\vec{R}}{R} \tag{6.3}$$

with $\vec{R}$ the distance between each charge i and the point $\vec{r}$.

The model lattice consists of a square array of 51×51 point charges $q = -e$ (plus image charges with $-q$), where the charges and their images of each specific vacancy structure have been removed from the center. The electric field contributions of all charges are added to the total electric field, which is calculated for all x and y, and for $z = 0$ to $3a$ in $0.1a$ steps. The z-component of the electric field as a function of height z, directly on a Cu patch and on two positions on the Cl background, are plotted in Figure 6.7d.

At low heights above the surface, e.g. at 3.6 Å (Figure 6.7a), the regular pattern of the Cl grid is visible in the z-component of the electric field. In the center of a Cu patch, the field is positive, as the field lines go through there. Looking at the horizontal component of the field (e.g. E_y in Figure 6.7b), we note that it is zero mostly everywhere, except at the two patch edges in the x-direction, i.e. perpendicular to the field, as expected. The E_x simulation gives an equivalent result. For heights in the few-ångström range, the values for the electric field are in the order of 1 V/Å.

For a line cut in the x-direction at height d through the center of the copper patch – the square of missing Cl (and mirror) atoms – the E_y contribution to the electric field is negligible. E_x only significantly deviates from zero at the edges, while E_z is the largest of the three: small on the Cl, but with a large plateau on the Cu area, see Figure 6.7c.

The shift of the bias voltage at which the resonance is observed while crossing a copper patch is consistent with the enhanced electric field obtained by this model, so we compare the shape of the resonance voltage trace with that of the simulated electric field.

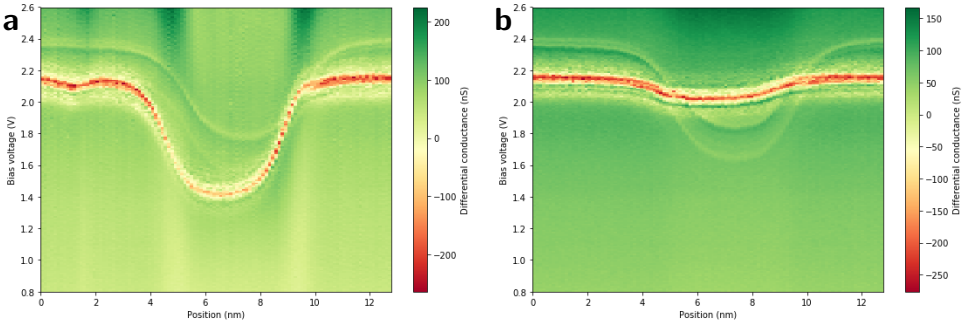

Figure 6.9: **Differential conductance line cuts through the centre and just outside of a copper patch. a**, Line through the centre of the 11 × 11 patch of vacancies. **b**, A parallel line 8 unit cells down, so along the 3rd chlorine row next to the copper patch. dI/dV spectra taken for a 200 pA set-point current at 2.6 V. All line cuts shown in Figure 6.13

As the vertical component is symmetric over the surface, we assume that the quantum dot on our tip is mostly responsive to the experienced E_z. To obtain a qualitative comparison, we only take the shape of the curves into account, defining the maxima as 1 and the minima as 0, with a sign change to compensate for the electron charge. Comparing the field at heights below $3a$ (in steps of $a/10$) with a linear regression method to the curves of the resonance, we can find the height for which E_z matches best with the resonance voltage. For the resonance over a 5×5 patch, the field at $z = 2.3a$ matched with 96 % (Figure 6.8a).

The resonance shapes observed with this tip were slightly asymmetrical, as shown in Figure 6.4. This might be due to a number of different explanations. It might be that the tip, that we assume to be half of a parallel-plate capacitor on the microscale, is slightly slanted with respect to the sample plane. The quantum dot might be positioned not exactly at the apex of the tip, but slightly to the side, resulting in a reduced sensitivity on one side. Subsurface defects sometimes result in elevation differences in the topography for identical vacancy structures, but as we see the asymmetry only for this specific tip, it is unlikely that this is the case here. It might also be possible that the quantum dot is sensitive to other directions of the electric field than the vertical one, implying an additional, positive effect near one edge and an additional, negative effect near the other. As these hypotheses are difficult to test, more research might be performed to determine the cause of this occasional asymmetry.

6.4. MULTIPLE QUANTUM DOTS

If several Cl atoms are located at different positions near the tip apex, multiple resonances can be expected for a given tip. In the case of Figure 6.9, at least two main resonances can be seen (at 1.4 V and a smaller one at 2.2 V), as well as a number of satellite peaks. The resonances are shifted along the direction of the line cut, the x direction, by an amount of $\Delta x = (2.5 \pm 1)a = 0.9 \pm 0.36$ nm with respect to each other. Comparing the line through the centre (Figure 6.9a) with a line a few unit cells away from the copper patch (Figure 6.9b), one can see that the shift of the main resonance is almost completely

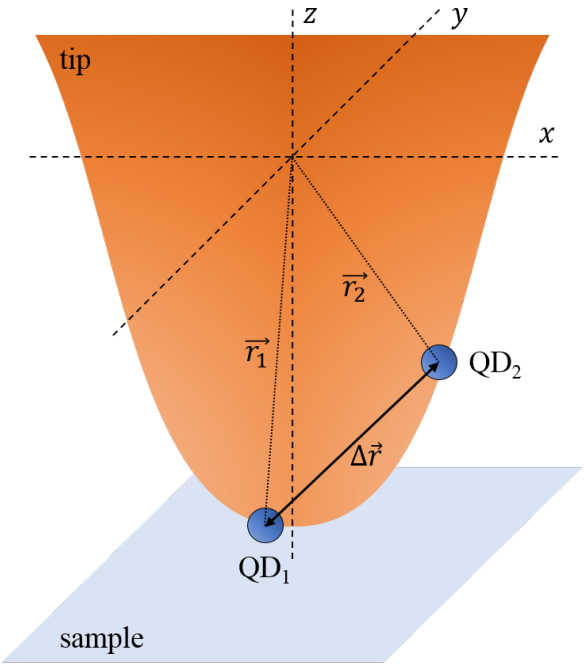

Figure 6.10: **Multiple quantum dots on the tip.** If multiple quantum dots exist on the apex of our STM tip, they will have a certain relative distance $\Delta\vec{r}$. Their relative position might be found by comparing the response of the resonances to the position of the tip over a known surface geometry with a known electric field.

diminished. The smaller resonance (at 2.2 V when outside) retains a pronounced shift in the middle region of the line. This not only suggests that the two resonances are due to two different quantum dots, but also that the second one is still affected by the copper patch when the first is already outside, thus suggesting a non-zero Δy. In Figure 6.10, a schematic of this scenario is shown, where a second quantum dot resides on the tip apex, but with some displacement $\Delta\vec{r}$ with respect to the first one.

Line cuts have been taken in parallel lines down from the centre of the patch at each Cl row, one lattice parameter a apart. With the centre at $y = 0$, the lines with $y \leq 5a$ are still over the 'vacancies' making up the copper patch. The lines $y = 6a - 8a$ are taken just outside the structure, and the shift of the main resonance is clearly reduced strongly, i.e. the sample electric field there quickly loses its strength. All of the lines $y = na$ are shown in Figure 6.13.

Because we assume that both resonances occur due to two identical quantum dots, we expect them to behave similar as a function of the experienced electric field. As the second resonance is still over the copper patch when the first one is already outside, we can estimate their relative distance not only in Δx as above, but also in Δy. The resonance voltage is lowest in the centre of the vacancy patch, as evidenced by all the other measurements. With increasing n, the resonance voltage in the centre of the line is monotonously increasing for the first (lowest) quantum dot. The second (highest in V)

quantum dot has its minimum resonance voltage (i.e. maximum field) at $n = 5-7$. This indicates that the relative displacement is $\Delta y = (6 \pm 1)a = 2.1 \pm 0.4$ nm.

To obtain the difference in height Δz, we need to compare the resonance voltages and how much they shift when the height is changed. Because the two resonances occur at different voltages, their voltage difference ΔV is a measure for their relative height difference. In Figure 6.12, the same lines – through the centre of the 11×11 copper patch – are plotted for decreasing tip heights, with a current set-point of 50, 100, 200 and 500 pA at 2.6 V. By comparing the linear behaviour of the resonance voltage of the first with the second resonance, as a function of tip height, we can estimate the height difference between the two quantum dots to be $\Delta z = 0.1 \pm 0.03$ nm.

With these methods, we have estimated the displacement between the two quantum dots to be $\Delta\vec{r} = (\Delta x, \Delta y, \Delta z) = (0.9, 2.1, 0.1)$ nm, with the absolute distance $|\Delta\vec{r}| = 2.3 \pm 0.6$ nm. When two resonances occur that behave so prominently different from each other, it is therefore feasible to get an estimation of their relative distance. For their horizontal displacement, a detailed two-dimensional map of $\mathrm{d}I/\mathrm{d}V$ spectra should reveal the (x, y) coordinates of the minimum resonance voltage for each of the different resonances, provided that they are sharp enough to be distinguishable. For their vertical displacement, a thorough study of the voltage shift as function of height is needed to verify that both resonances indeed lie on the same $V(z)$ curve.

This analysis is only valid if all quantum dots react in an identical way to the applied electric field, i.e. to their position over the sample and its charge configuration. We have found resonances in our differential conductance spectra in all sorts of different shapes (Figure 6.1), however, no differences in behaviour due to variables such as current, tip height and surface geometry have been observed. From this, it can be assumed that all resonances are indeed from identical quantum dots, where their relative distance can be inferred by the above methods.

6.5. LOCAL TIP GATING

Transport measurements in an STM set-up typically only have a source and a drain: the tip and the sample. Apart from the tip-sample distance, the bias voltage is the only controlling parameter, leading to a tunnel current from tip to sample, flowing through any objects in between. Generally, no space for a gating electrode is available. However, by adjusting the tip height, the local electric field $E = V/d$ can be controlled, thus acting as a gate for any atoms or molecules in the junction. Since the three parameters tip height, bias voltage, and tunnel current are always interdependent, keeping the bias voltage constant while decreasing the tip height means that the tunnel current will increase exponentially.

To get an idea of the electric field sensitivity of the quantum dot, we compare the gating behaviour on the chlorine background and in the middle of the 11×11 copper patch. Differential conductance spectra are taken at those two positions, for set-point currents from 20 pA up to 90 µA, set at 2.6 V. The exact z positions for each spectrum are extracted, and converted to an absolute height via the $I(z)$ curve in Figure 6.6. In Figure 6.11a,b, the spectra are shown, with the bias voltage versus the absolute height and the differential conductance in colour, normalised to the value of the first data point for a qualitative comparison. For both Cl and Cu data sets, two resonances can be observed

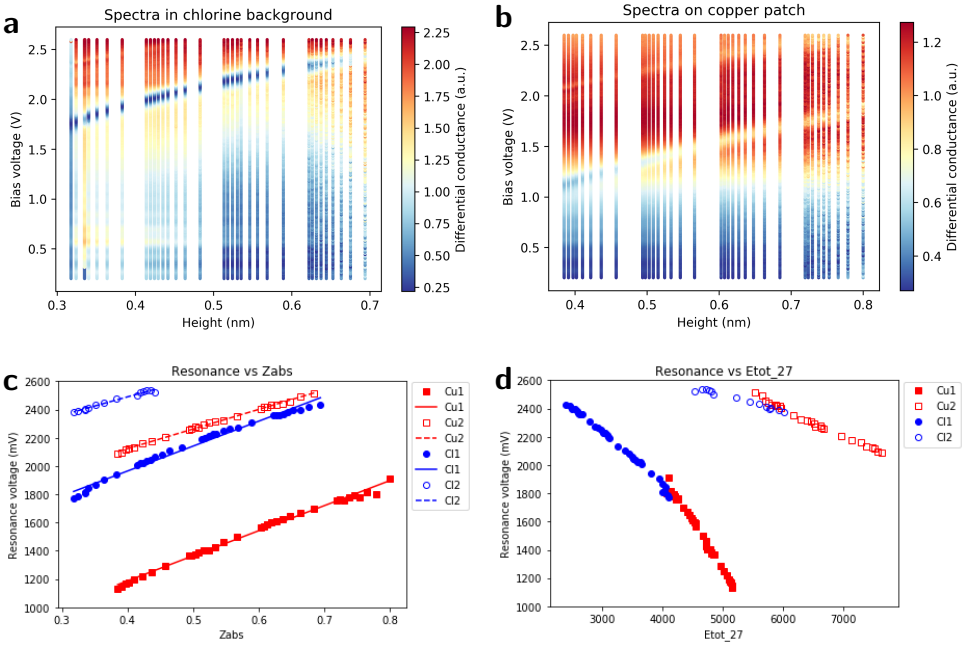

Figure 6.11: **Behaviour of the quantum dot resonance on the chlorine background and on a copper patch.** **a**, Each point in a normalised $\mathrm{d}I/\mathrm{d}V$ spectrum (colour scale) as a function of the bias voltage and its absolute height, where spectra have been taken on the chlorine background for multiple set-point currents, i.e. tip heights. **b**, Same as in **(a)**, but in the centre of an 11×11 copper patch. **c**, The resonance voltage of the two resonances in each spectrum, as a function of the absolute height. Red squares are on the copper, blue circles on the chlorine background. Filled markers are the main resonance at lower voltage, open markers are the second resonance at higher voltage. Linear fits have been drawn through each of the four sets. **d**, For each of the points in **(c)**, the total electric field has been calculated from the tip field $E_t = V/z$ and the simulated sample field $E_s(z)$ by $E_{tot} = E_t + c \cdot E_s$, with $c = 0.27$. Both the first resonances (filled markers) and the second resonances (open markers) line up with this factor.

at different voltages. The resonance voltage and height appear to have a linear relation, as shown in Figure 6.11c.

Like before, we assume that the two resonances are two identical quantum dots, located at different heights, with one at the tip apex and the second slightly above. As we expect the behaviour for both quantum dots to be the same, their height difference may be calculated from this graph by shifting the upper resonances until they lie on the same line as the lower resonances. We find that a correction of $\Delta z = 494$ pm for the copper patch and $\Delta z = 303$ pm for the chlorine background is needed for the resonances to line up. We expect Δz to be the same in both cases, because the measurements were done alternately on copper and on chlorine. However, due to the non-linear decay of $E_z(z)$, particularly when over the copper patch, a difference in Δz is expected. Any further apparent difference in the relative distance might be explained by a horizontal offset, i.e. if one quantum dot is in the centre of the Cu patch, the other one is close to one of the edges, and thus feels a larger or smaller field. For this to be the case, however, the hori-

zontal offset has to be quite large, as the distance between the centre of the copper patch and the edge is $5.5a = 2$ nm. Albeit the height difference $\Delta z = 0.4 \pm 0.1$ nm calculated in this way is larger than that in Section 6.4 (0.1 nm), this might be explained by tip changes between these measurements rearranging both the apex atoms and the quantum dots there.

Using the absolute height, it is possible to calculate the tip electric field $E_t = V/z$, and combine it with the simulated field $E_s = E_z(z)$ that is due to the sample, from Figure 6.7d. For the sample field, we only use the z component, because due to symmetry reasons, the horizontal components are zero on both the chlorine background and in the centre of the copper patch. In the quantum dot model, the resonance voltage represents the voltage at which a state in the quantum dot is resonant with the Fermi level of the tip. This transition from N to $N+1$ electrons in the QD shows up as a Coulomb diamond when the $\mathrm{d}I/\mathrm{d}V$ spectrum is plotted versus both bias and gate voltage (Figure 6.2). When we plot our spectra versus the effective electric field, we therefore expect the resonances to line up, to form Coulomb diamonds.

In the simplest picture, each chlorine atom binds ionically to the copper substrate, and harbours almost exactly one electron [50, 53, 135], but we do not know to what extent this approximation is valid. We therefore calculate the total field as $E_{tot} = E_t + c \cdot E_s$ for different charges $c \in [-1, 1]$. The resonance voltages of the copper and chlorine measurements line up when $c = 0.27$, as shown in Figure 6.11d. This would suggest that the charge transfer from copper substrate to chlorine monolayer is such that the chlorine atoms each have a charge of $q = -0.27e$, or 0.27 electron per Cl ion. This value seems too low, since literature tells us that the Cu_2Cl surface is essentially ionic (0.93 electrons per Cl) [136]. However, if we consider that the electric field of a single dipole is proportional to the charge q and the separation between the dipole charges d, and inversely proportional to the 3rd power of the distance r, $E \propto qd/r^3$ [134], we can naively assume that the errors of these parameters also multiply into the total error. For the simulation, we took the distance between the Cl atom and the Cu layer (acting as conductor plane) as $a/2 = 0.178$ nm, while it actually is smaller: 0.158 nm [53]. And considering that errors in the absolute height are in the order of 50 pm, the error in r can be estimated as 550/600 for the average height between 0.4 and 0.8 nm, where our measurements and simulations took place. Together, the error is then $0.93 \times \frac{1.58}{1.78} \times \left(\frac{550}{600}\right)^{-3} = 0.60$. This crude approximation brings us part of the way to reconcile experiment and simulation, but not quite. Furthermore, we define a single conductance channel as being in contact, $z = 0$. If this point of contact is more accurately described by a distance of two atom radii, $z = 270$ pm for two Cu atoms, the resonance alignment is best for $c = 0.14$ (half the previous value). Clearly, for a full understanding of the electric fields applied to the quantum dot on our tip, more calculations are needed that take the quantum mechanical properties of our surface into account (such as DFT calculations). However, the model of an E-field sensitive quantum dot on the tip apex does lead to a qualitative explanation of this phenomenon.

6.6. CONCLUSIONS AND OUTLOOK

We observe a resonance in some of our $\mathrm{d}I/\mathrm{d}V$ spectra, leading in some cases to a negative differential resistance (NDR). This can be explained by the resonance of a state of a quantum dot located on or near the apex of our STM tip. A chlorine atom, weakly coupled to the tip, can lead to a situation with a double tunnel barrier, thus giving rise to the observed QD-like behaviour. The voltage V_R, at which the resonance occurs, shifts to lower values with decreasing tip height and when the tip is positioned over vacancies in the Cu_2Cl surface. This observation is consistent with a dependence of the QD on the experienced electric field.

Line cuts of $\mathrm{d}I/\mathrm{d}V$ spectra were made over structures made from vacancies arranged in square $N \times N$ patches, to compare the behaviour over bare Cu with that over Cl. For small ($N \leq 5$) patches, the resonance voltage V_R shifts to lower values for larger N without levelling off, but for 11×11 copper patches they do level off inside the patch, suggesting that the quantum dot on the tip feels the electric field of the boundary up to $2a \approx 0.7$ nm away.

Because the sample geometry and thus charge distribution influences the behaviour of the resonance, we simulated the electric field of vacancy patches of various sizes using a simple image charge model, with one electron charge per Cl atom and using the Cu substrate as the conductor. This provides the electric field in three directions as a function of tip position over the area. We compare $\mathrm{d}I/\mathrm{d}V$ line cuts over copper patches of different sizes with the simulations, to find for which height the simulation matches the measurement best. The quantum dot seems to be mostly sensitive to the z component, and this simple model reproduces the qualitative behaviour of the resonances as it crosses the copper patch at a height of ~0.5 nm.

In some cases, two distinctly behaving resonances can be seen, indicating that there are two different quantum dots on or near our tip apex. By comparing the resonance voltage curves for different line cuts over a copper patch, the horizontal displacement can be estimated. Curves at different set-point currents give us an indication for the height difference, telling us the relative distance of the two quantum dots on our tip.

We compared the resonant behaviour between the copper and the chlorine by taking constant-height $\mathrm{d}I/\mathrm{d}V$ spectra on set-point currents from 20 pA to 90 nA. Two resonances are seen, where we can estimate the height difference by shifting the curves until they align. We use the absolute height to calculate both the tip and the sample contribution to the electric field, and plot the resonance voltage versus the experienced electric field $E_{tot}(z) = E_t + c \cdot E_s = V/z + c \cdot E_z(z)$, with c a fitting parameter for the simulated sample field $E_z(z)$. We expect the resonance voltage to be a single continuous curve as a function of the experienced electric field, analogous to Coulomb diamonds in a gated transport measurement. In this case, the combination of changing tip height and sample field would lead to an effective electric field applied to the QD on our tip, thus forming a way to gate the system. For $c = 0.27$, the resonances align to a single curve, suggesting that only 0.27 electrons are present per chlorine ion, which is not in agreement with the ionic bond that Cl forms with the Cu substrate. Instead, the approximations used in the model are discussed, showing how small changes in charge q, dipole distance d, and height z can partially account for the quantitative disparity, without compromising the qualitative agreement of our model with the measurements.

In conclusion, we observe resonance-like features in a number of our differential conductance spectra, sometimes leading to NDR. We explain this by the presence of a quantum dot – for instance a weakly bound chlorine atom – on the apex of our STM tip, causing a resonance at varying bias voltages for varying local effective electric fields. The quantum dot is gated by a combination of the tip height and the local surface charge distribution. The existence of multiple resonances can point to multiple quantum dots, of which the relative position is discussed, using vacancy structures of various shapes and sizes. A simulation of the electric field due to the sample gives a qualitative agreement with the experiment, indicating that once the quantitative behaviour of the quantum dot is known, the system can be used to probe the local electric field distribution of unknown structures.

6.7. SUPPLEMENTARY FIGURES

Multiple line cuts of the $\mathrm{d}I/\mathrm{d}V$ spectra over the 11×11 copper patch have been taken. In Figure 6.12, horizontal cuts in both the x and y directions through the centre of the 11×11 patch have been taken at different current set-points, from 50 to 500 pA, while at 2.6 V. See Figure 6.5 and the discussion in Section 6.2.2.

In Figure 6.13, line cuts at 200 pA set-point current for 2.6 V have been measured along the centre ($y = 0$) and along parallel lines interspersed by na, with $n \in 0, 1, \ldots, 8$ and $a = 0.355$ nm the lattice constant. See Figure 6.9 and the discussion in Section 6.4.

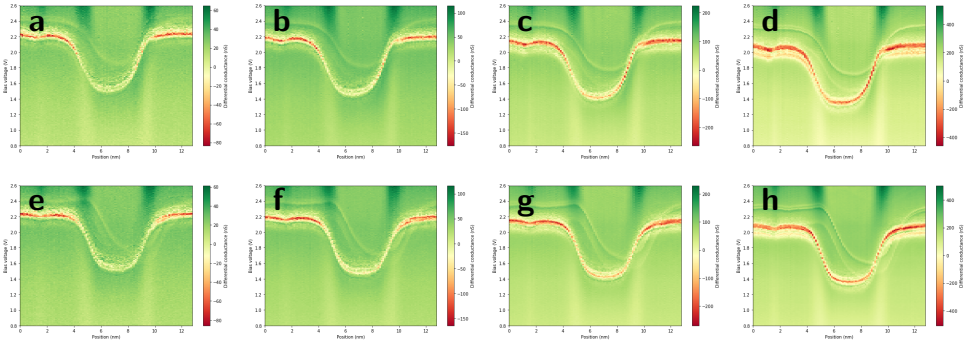

Figure 6.12: **Line cuts over the 11 × 11 copper patch as a function of height.** Horizontal (**a-d**) $y = 0$ and (**e-h**) $x = 0$ line cuts of the differential conductance (colour scale) for different heights, with increasing current set-points at 2.6 V: (**a**,**e**) 50, (**b**,**f**) 100, (**c**,**g**) 200, and (**d**,**h**) 500 pA. The resonances shift down with decreasing height. From the $V_R(z)$ relation, the vertical distance between the two resonances might be inferred, while from the difference between the two axis directions, their horizontal distance might be estimated.

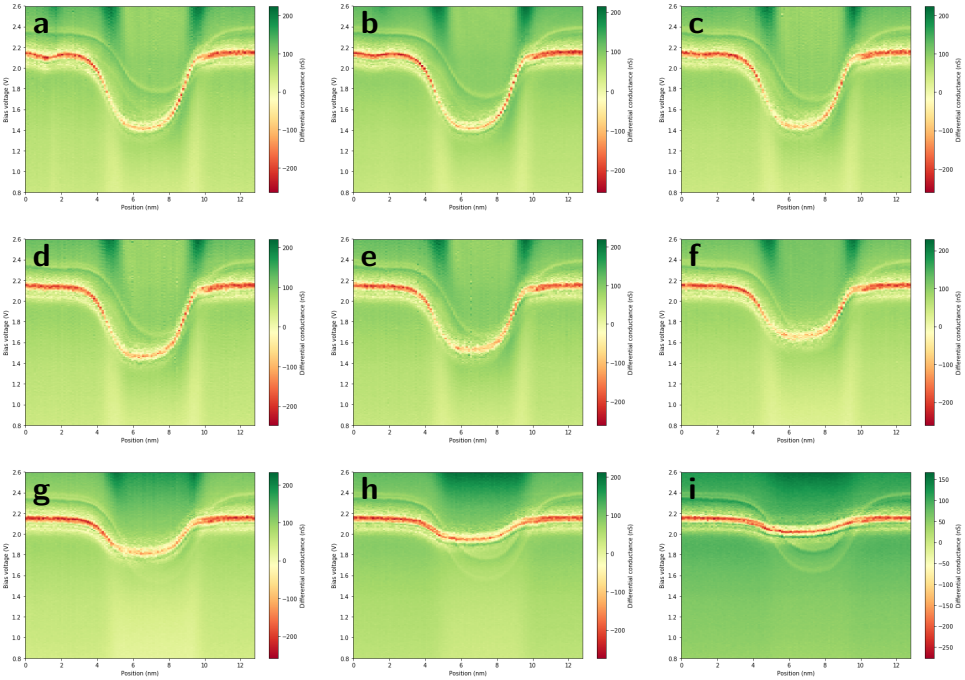

Figure 6.13: **Line cuts over a copper patch showing two distinct resonances.** Horizontal lines of the differential conductance (colour scale) over the 11 × 11 patch, at position $y = na$, starting in the centre then going down, with $n \in \{0, 1, \ldots, 8\}$ (**a-i**). The largest resonance remains pronounced within the patch ($y \leq 5a$), but dies off quickly when on the chlorine again ($y \geq 6a$). The fainter resonance at slightly higher V_R remains pronounced throughout, suggesting that it is horizontally displaced so it is still above the patch.

7

TRANSITION METAL ATOMS ON COPPER CHLORIDE

Various metals are evaporated on the Cu_2Cl surface in order to study their behaviour on this substrate. The different adsorption sites for silver, nickel, and iron are explored, and atom manipulation was on occasion shown to be possible. Silver and nickel do not show any steps in the differential conductance spectrum that can be attributed to inelastic tunnelling. The steps present in the iron spectra on hollow sites seem to shift to lower energies with an out-of-plane magnetic field of up to 9 T, although more work is needed to confirm this finding.

To study the magnetic behaviour of individual atoms, the spin states need to have lifetimes in the measurable range. Since the outer orbitals of single atoms on a bare metal surface tend to hybridize with the electronic states of the bulk, a decoupling layer is needed to isolate the adatom from the bulk [20, 34, 87, 137, 138]. Copper nitride islands on Cu(100) surfaces have long been a workhorse substrate to study magnetism on the atomic scale [58], and since the chlorine terminated surface forms large, clean insulating areas on copper, it follows that Cu_2Cl/Cu(100) surfaces might also be used for the study of magnetic adatoms.

7.1. INELASTIC TUNNELLING SPECTROSCOPY

The most common way of tunnelling in STM is elastic, in which the tunnelling electron does not lose energy on its way from tip to sample (or vice versa). If the electron, however, loses energy in the process, for example by vibrationally [139–141] or magnetically [17] exciting a molecule or atom, it is called inelastic tunnelling. Because these excitations cost energy, it can only occur when the electron energy eV is larger than the excitation energy ΔV, so that $eV \geq \Delta V$, with e the electron charge and V the applied bias voltage. At low voltages, all electrons tunnel elastically, but at each excitation energy, an additional conduction path opens, and a step in the differential conductance curve appears. Taking $\mathrm{d}I/\mathrm{d}V$ measurements on these systems is therefore called inelastic tunnelling spectroscopy (IETS).

Most vibrational excitations in molecules occur at higher voltages of at least tens of millivolts, while magnetic excitations in atoms typically occur at voltages below ~20 mV [18, 141]. In the magnetic case, electrons are excited to a higher orbital in the outer shell, with an optional spin-flip. In this chapter, we search for steps in the $\mathrm{d}I/\mathrm{d}V$ spectra of transition metal atoms placed on the Cu_2Cl surface. To find out if these steps are indeed magnetic, we place them in an external magnetic field, both in-plane and out-of-plane with respect to the surface, to see if they shift in energy.

We evaporate three different transition metals (silver, nickel and iron) using the procedure described in Chapter 2. As magnetism typically has its origin in unpaired electrons in the d orbitals, silver (with $[\mathrm{Kr}]4d^{10}5s^1$), is not expected to behave magnetically, because of its filled d shell. Nickel ($[\mathrm{Ar}]3d^8 4s^2$ or $[\mathrm{Ar}]3d^9 4s^1$) and iron ($[\mathrm{Ar}]3d^6 4s^2$) on the other hand, do have unpaired electrons in their $3d$ shells, and are ferromagnetic at room temperature. The magnetic moment of Ni is small, if not negligible, on Cu_2N [137], while that of Fe is definitely present in comparable systems [18, 142].

7.2. ADATOM POSITIONS

There are three possible distinct high-symmetry positions for an adatom to lie on the Cu_2Cl surface after evaporation, see Figure 7.1: the *bridge* position along one of the lattice axes between two chlorine atoms; in the *hollow* site between four neighbouring chlorine atoms; and the *on-top* site, where the adatom is above, and bound to only one chlorine atom. Additionally, in the case of a non-saturated Cu_2Cl layer, it is possible for an evaporated atom to land on or in a chlorine vacancy. This is at the same lattice position as the on-top sites, so it may be hard to distinguish, but the atom will appear lower, because of the height difference.

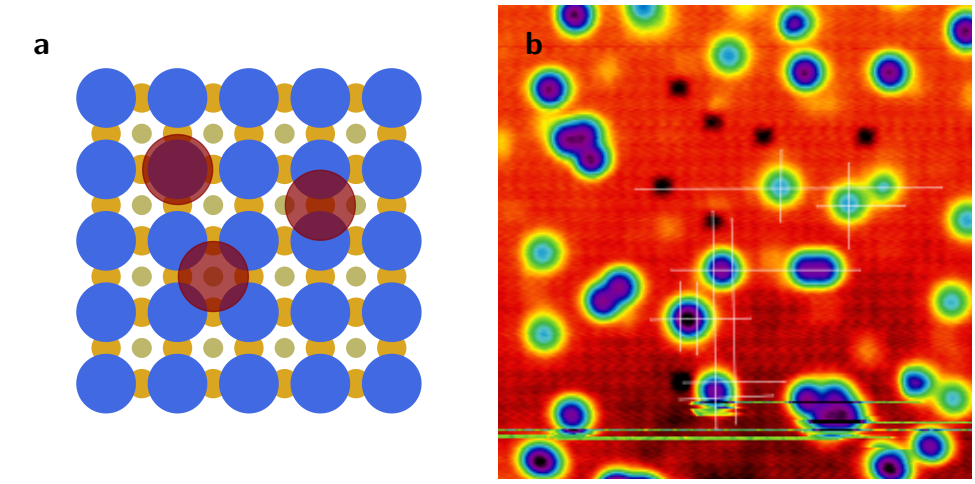

Figure 7.1: **Possible adsorption sites for adsorbate atoms on $Cu_2Cl/Cu(100)$. a,** Orange circles are Cu atoms in the top layer of the bulk, khaki the Cu atoms in the second layer, blue the Cl atoms. Three adatom positions are shown in red: on top of a Cl atom (*on-top* position), in between four Cl atoms (*hollow*) and in one of the Cl rows, in between two Cl atoms (*bridge*). In the case of under-saturation of the Cu_2Cl monolayer, it is also possible for an adatom to be positioned on top of a Cl vacancy (not shown). **b**, Silver adatoms on CuCl, with some lattice axes drawn.

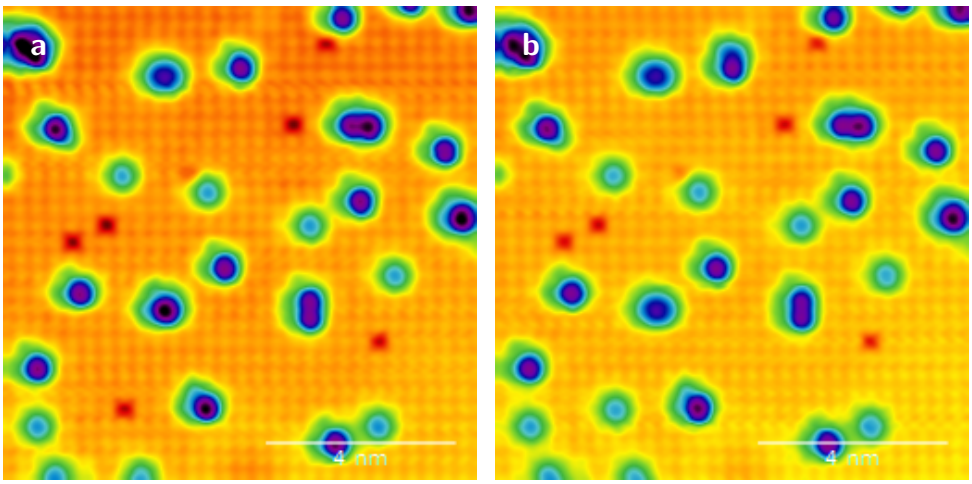

Figure 7.2: **Ag atoms on vacancies. a**, Manipulating an Ag atom from a cluster to a vacancy, **b**, which afterwards looks identical to many other atoms. Adatoms appear roughly 100 pm high. Scale bars 4 nm.

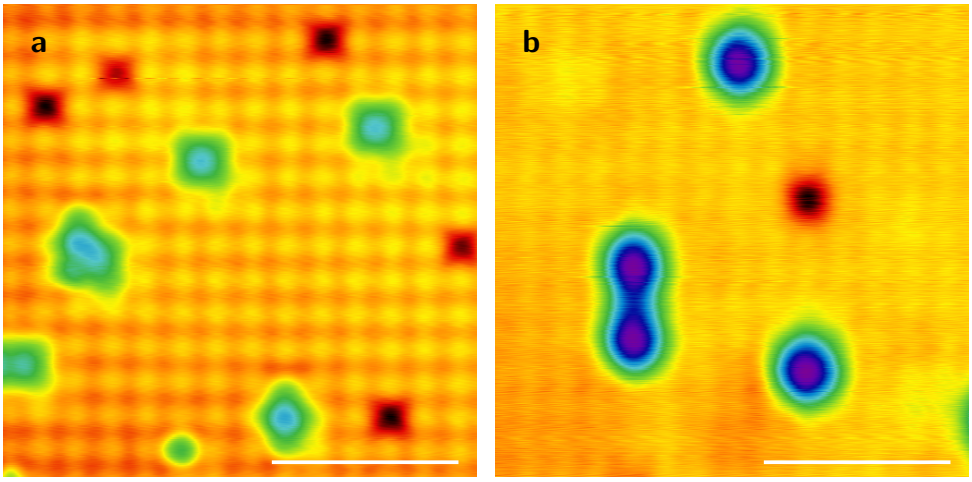

Figure 7.3: **Ni atoms on Cu_2Cl**. Colour scales for visibility are not identical. Scale bars 2 nm.

We found silver atoms generally on two different positions: at bridge sites and on vacancies. In Figure 7.2, we can see the vacancy Ag adatoms as ~100 pm high, and the Ag bridge adatoms as ~170 pm. Dragging the tip from a higher cluster to a vacancy sometimes resulted in atom manipulation. Though not always reproducible, we did extract one atom from a larger cluster, which was then placed on the vacancy, as shown in Figure 7.2a-b. As there are many adatoms with identical appearance, this suggests that all of them are in fact lying on a vacancy. Although we cannot exclude the existence of Ag at on-top and hollow sites, it seems that they mostly appear in the bridge and vacancy positions.

Nickel atoms on CuCl have a few unusual shapes (Figure 7.3): at the hollow sites, they appear as square protrusions roughly 60 pm in height. Also, there are oval-shaped objects at lattice sites, possibly a Ni atom on top of a Cl atom or on a vacancy. These oval objects come in two orientations, horizontal and vertical, and are ~70 pm high. Some circular atoms also occur on the surface, these where also in lattice positions and even lower in height: 50 pm. We speculate that the oval shapes might be Ni atoms somehow deforming the Cu_2Cl lattice in one of the two lattice axes, while the circular shapes might be Ni atoms on a vacancy.

Iron atoms on CuCl appear to occur in all possible positions, see Figure 7.4. Hollow sites and on-top sites both appear ≥150 pm high. In Figure 7.4c, some are shaped like isosceles triangles, with the centre on a lattice site. They appear pointing in all four directions, and seem to be ~80 pm high. Because they are lower in height, we speculate that these might be Fe atoms on a vacancy, that are either chemically distorting the Cu_2Cl lattice around it, or bound slightly more strongly to one than the other three neighbouring Cl atoms.

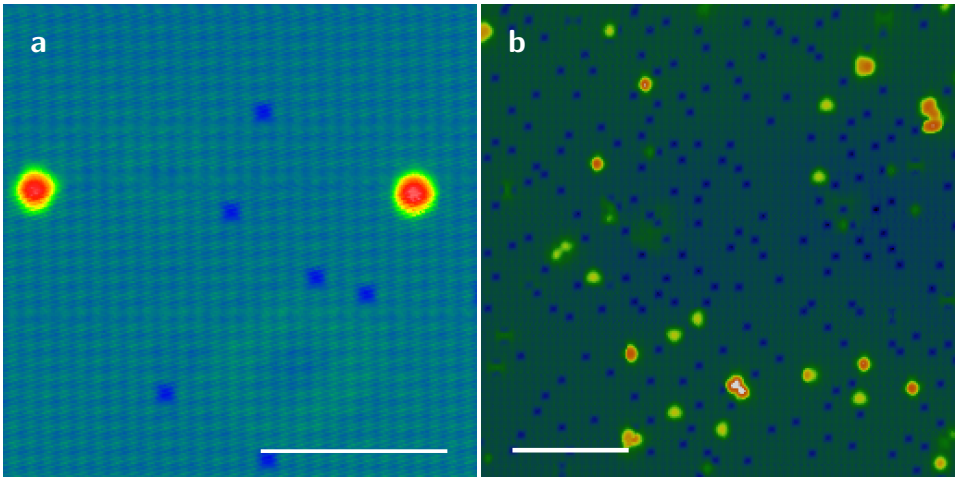

Figure 7.4: **Three landing sites seem to occur for Fe adatoms. a**, Adatoms on an on-top and hollow position. **b**, Fe adatoms on vacancy positions appear as triangles pointing in four directions. Scale bars are 5 nm.

7.3. SPECTROSCOPY AND FIELD DEPENDENCE

The differential conductance spectra for the bridge and vacancy silver adatoms were flat, and did not show any steps or other features within the ±100 mV range. The nickel spectra, on both the squares at hollow sites and the oval adatoms, also appeared featureless in the ±20 mV range. When an out-of-plane magnetic field of 6 T was applied, the nickel spectra also remained flat. This means that both silver and nickel appear to be non-magnetic at each of their adsorption positions. For silver this was expected, but nickel – with only two unpaired electrons – is magnetic in some cases, so there was an a priori chance for nickel adatoms on this surface.

Certain iron atoms, however, do show some features in their spectra. They were measured on the adatoms that were adsorbed on the hollow positions, as seen in Figure 7.4 (blue curve). The spectra have steps around ±10 mV, and possibly at ±15-20 mV. A magnetic field is applied in both the in-plane direction ($B_x = 2$ T, green) and the out-of-plane direction ($B_z = 6.5$ T, orange, and $B_z = 9$ T, red). If the steps shift when the field is applied, that would be proof that the inelastic tunnelling process is really present and magnetic in origin. In this case, it seems that, with increasing B_z, there is a shift toward zero, but the shift is smaller than 3 mV, which is comparable with the uncertainty. With an applied magnetic field in the x direction, there seems to be no shift.

Although it appears that Fe atoms in hollow positions have an inelastic magnetic transition at the same order of magnitude as anisotropy energies measured on Cu_2N (~5 mV, [18, 20]), it is still too early to definitively confirm this from these measurements alone. Furthermore, it is possible that the other adsorption sites also harbour IETS steps, as we do not have sufficient measurements on those adatoms to rule them out. It is to be expected that when iron atoms are bound in different ways to the substrate, different orbitals play a role, and that would mean that magnetic effects might be more or less pronounced, depending on the precise orbital filling and chemical interactions.

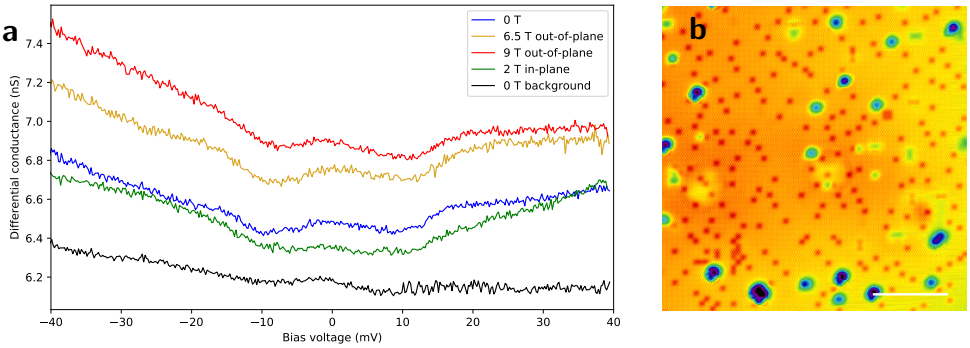

Figure 7.5: **Differential conductance spectra on Fe in various magnetic fields. a**, The $\mathrm{d}I/\mathrm{d}V$ spectra on an iron atom in a *hollow* site, without field (blue), and exposed to a 2 T in-plane field (green), and 6.5 T (orange) and 9 T out-of-plane (red) magnetic fields. An off-atom background spectrum at 0 T is shown in black. The features around ±10 mV do appear to shift slightly (≤3 mV) with increasing out-of-plane magnetic field. Measured at 1.5 K, the height was set at 40 mV, 400 pA. 0 T data corrected by adding a 5 pS/mV slope. **b**, A topography image of Fe adatoms on $Cu_2Cl/Cu(100)$. Scale bar is 5 nm.

7.4. CONCLUSIONS AND OUTLOOK

We evaporated the transition metal atoms silver, nickel and iron on the copper chloride surface, to investigate their magnetic behaviour. We found that silver atoms mainly adsorb in bridge positions and on chloride vacancies, while nickel adatoms mostly appear with a distorted non-circular shape: square in the hollow sites, and oval shapes on top of a Cl atom or a vacancy. Both silver and nickel do not show signs of inelastic tunnelling events, and are non-magnetic on this surface.

Iron appears in hollow and Cl positions and on vacancies as a triangle pointed in one of the four neighbouring atoms. The adatoms in hollow sites show some steps in their differential conductance spectra, which seem to shift slightly when an out-of-plane field of up to 9 T is applied. Although this is an indication that Fe atoms adsorbed on Cu_2Cl hollow sites might indeed be magnetic, more work needs to be done to verify this finding. The effect is relatively weak, so stronger tools to observe this are needed: higher fields and lower temperatures. It might be worthwhile to further scrutinize the atoms in other adsorption sites, especially if they can be manipulated to exact known locations. Once the properties for single adatoms are known, combinations of two or more can be invesigated, for example, for tuning the local magnetocrystalline anisotropy [27].

Incidentally, it was possible to manipulate atoms, although not yet reliably so. We used this in Figure 7.2 to prove that some of the silver adatoms indeed lie on a vacancy. Considering the success of vertical manipulation techniques on Cu_2N [35, 76], it seems very plausible that the same techniques might be tailored to this surface as well, since the nitride reconstruction is similar to our chloride reconstruction.

Combined with the vacancy manipulation introduced in Chapter 2 and the large terraces of uninterrupted, clean substrate, it might be possible to construct large structures where magnetic atoms are coupled to each other – or even to vacancies – over long distances, thus providing an entirely new template for future engineering.

8

CONCLUSIONS AND OUTLOOK

STM ON A CHLORINE RECONSTRUCTED CU(100) SURFACE

We have prepared chlorine terminated copper (100) surfaces with variable vacancy densities, for imaging and manipulation by scanning tunnelling microscopy. The non-saturated Cu_2Cl surface is characterised by single vacancy defects in large unobstructed terraces, unlike the island formation, typically only tens of nanometres large, that form in the Cu_2N surface [58]. This means that if the surface is used as a decoupling layer, it is only limited by the crystal terrace size, which can be hundreds of nanometres wide. Together with the slightly larger work function compared to similar substrates, this might lead to better opportunities of studying magnetism and other phenomena at the atomic scale, such as single atoms [36], chains [35], or more complex designs that might be assembled at the nanoscale.

We developed a vacancy manipulation technique, where the STM can controllably exchange a vacancy with one of the neighbouring atoms, with sometimes more than 99 % directional reliability. This manipulation was improved to be fast (~1 manipulation per second), so large-scale structures can be built, as demonstrated in Chapter 3. Furthermore, any vacancy structure can be built with high precision and relatively fast, as can be seen in Chapters 4, 5 and 6.

The vacancies in the Cu_2Cl surface are stable below 77 K, the temperature of liquid nitrogen. This means that the investigation of denser structures where the individual vacancies are closer than three lattice spacings ($3a$) apart, must be conducted at 77 K at the highest. Kept at low temperature in ultra-high vacuum for more than seven months, no significant contamination issues arose. This suggests that the surface is sufficiently chemically stable under these conditions, possibly allowing us to lift some of the stringent requirements without losing surface quality.

The Cu_2Cl surface is stable, can be prepared with reliable vacancy coverages, such that large-scale automated vacancy manipulation is possible. Since the heavier halogens Br and I have similar reconstructions on copper, they might be very viable alternatives

This chapter is a compilation of all the conclusion paragraphs in the previous chapters.

to Cl, using the techniques developed in this thesis. Finally, new venues might be found when combining the insulating properties of the substrate with the possibility of large-scale atom manipulation, creating hybrid designs where atoms or molecules are placed on custom-designed vacancy structures with locally varying material properties.

A KILOBYTE REWRITABLE ATOMIC MEMORY

Having a working, rewritable data storage with several thousands of single-atom bits represents a significant step forward in the field of atomic-scale electronics. For further advancement, an important improvement still to be made is an orders of magnitude increase in the readout speed. To this end, the memory would have to be scanned in constant height mode rather than constant current mode. At constant tip height, using settings similar to those presented here, the current difference between a Cl atom and a vacancy is on the order of 1 nA. Demonstrated high-frequency STM electronics [100] allow a 1 nA signal to be measured at a bandwidth of 1 MHz, suggesting that readout speeds on the order of 1 Mb/s should be attainable. The required scan speed of 0.36 mm/s can be achieved by using video-rate STM [100]. There is no physical limitation that prevents the fabrication of much larger in-plane atomic memories.

Going to higher temperatures, such as 77 K, can be very advantageous in order to make this data storage technique more accessible. Liquid nitrogen is much cheaper and easier to handle than liquid helium, and the STM can be designed in a much simpler way, because of the reduced needed cooling power, and thermal insulation. As no spectroscopy is needed on the atomic memory, but just the ability to manipulate atoms reliably, the only constraint is the stability of the surface itself.

As shown in Figure 2.8, the Cu_2Cl substrate is stable up to 77 K; the bytes as we designed them, two unit cells apart, however, are not. The two unit-cell vacancy spacing configuration is apparently too eager to collapse into a lower energy state, but a spacing of three unit cells as in Figure 2.7 is still stable at high temperatures. This means that the bit design has to be adapted, e.g. each bit now in a 3×3 area, so the information density will go down by at least a third from 502 Tbit/inch^2 at 4 K to ~335 Tbit/inch^2 at 77 K.

When going to memories that are much larger than our kilobyte, a big issue becomes locating a block when the tip is far away. Large and fast movements cause the piezo actuators of the tip to lag behind in moving, called piezo 'creep', and the tip position will only be stable after enough waiting time. This can be solved with intermediate 'stepping stones' every ten to twenty nanometres, where the tip can track and recalibrate its position on a marker, before moving to the next marker. We already used this method in our kilobyte-sized memory when moving from one row to the next. Tracking on a marker typically takes in the order of a second, because shorter tracking times hamper the accuracy. For larger memories, this means that the moving time will go up, because of the increased number of stepping stones.

Knowing where the tip currently is located, and where it needs to go, is also very important in this. The markers developed here are simple prototypes in a 5×5 space that can still be deciphered by the human eye. For larger memories, however, it might be more desirable to develop bigger markers with encoded coordinates, like the QR-codes being used more and more in society.

When the memory gets large enough, it eventually becomes larger than the scan

range of a normal scanning tunnelling microscope, which is in the order of a few micrometers at low temperatures. Scaling up to higher temperatures is an advantage here, because the piezoelectric materials that determine the scan range give larger extensions with higher temperatures, at the same applied voltage. At some point, it becomes necessary to involve multiple STM tips, as proposed in IBM's 'Millipede' project [101]. One of the main difficulties here would be to control them independently from each other. Maybe it is not necessary to completely decouple the movements of the tip, but each tip would still have to be aligned with respect to the other tips, before starting a simultaneous readout of each section's n^{th} bit. A scheme like this would greatly improve the speeds for writing and read-out.

Finally, it might be the case that there are substrates where it is equally possible to manipulate vacancies, but with a higher melting temperature, such that a memory can remain stable above 77 K and for longer times. Similar substrates such as the heavier halogens – bromine and iodine – on copper (100) come to mind, which form similar surface reconstructions [49, 50, 67–69]. Furthermore, with the recent advancements in assembling stacked structures from 2D-materials such as graphene, h-BN, MoS_2, and many more, it becomes tempting to fantasize about an expansion in 3D space. Translating the two-dimensional storage density presented here to three dimensions, would – assuming a modest vertical pitch of 5 nm – allow the storage of the entire US Library of Congress in a cube 100 µm wide.

From a physical perspective, the fact that we can manipulate thousands of atoms per day, and create structures where more than sixty thousand atoms lie exactly in their intended positions, really does ring true on Feynman's words, we can now "arrange the atoms one by one the way we want them".

EMERGENCE OF QUASIPARTICLE BLOCH STATES IN ARTIFICIAL CRYSTALS

By means of atom manipulations of chlorine vacancies in the $Cu_2Cl/Cu(100)$ substrate, we can engineer artificial lattices. This demonstrates a way to craft artificial one- and two-dimensional materials with tuneable electronic properties. We explore the emergent band formation as we build lattices of varying structure, density and size. For all lattices studied, the bottom of the emerging band is found to shift towards lower energies, in accordance to the tight-binding model, as the lattice size or density is increased. Furthermore, we find that the band onset saturates for larger structures, implying that the effect of finite size can be neglected. In the case of two-dimensional checkerboard- and stripe-shaped lattices, we observe standing Bloch waves. These patterns are well explained using a tight-binding model that includes coupling to the electron bath. Surprisingly, the effective mass of the observed Bloch waves is found to depend strongly on the lattice geometry. Our work provides a testing ground for future designer materials where the electronic properties can be defined a priori.

ARTIFICIAL MOLECULES

As a single vacancy exhibits a peak in the differential conductance around 3.5 eV, it is proposed to position multiple vacancies close together in order to couple their states in a tight-binding manner. Dimers have been created, of pairs of vacancies in a variety of specific configurations between 1 and 4 lattice constants apart. Spectra have been obtained along a line through these pairs, where a bonding and anti-bonding state have been predicted to emerge inside and outside the vacancies, respectively [112].

We obtained the hopping term $t = \Delta/2$ from these spectra, where Δ is the difference in energy between the bonding and anti-bonding peaks in the spectra. For smaller distances, the shift in the peaks is larger, and it becomes much more difficult to reliably obtain the anti-bonding peak, which is at higher energy, as it is obscured by the peaks and features already present in the spectrum above 3.6 V. Using only the bonding peak, at lower energy, the couplings that are calculated are of the same order of magnitude as before, but behave more like an exponential dependence on the dimer separation. A fit through these values for the coupling t gave the predictions on which the optical gap simulations are based.

Making structures of coupled vacancies allows us to describe the tight-binding band properties of the total structure. Organic polyacene molecules of various lengths are replicated in three different vacancy configurations, where we expect the optical band gap to close and open as a function of the chain length [113]. Tight-binding calculations of the structures predict a band gap for certain lengths in the order of tens of meV for the densest configuration, which has the strongest coupling that can be achieved in this system.

Two-dimensional line cuts through the chains, however, don't reveal any features in the DOS that resemble our simulations, even when comparing all lengths from $N = 3$ to 10, and $N = 20$. The proposed signal (36 meV) is in the order of our detection limit (10 meV), and even though we operate at low temperatures and with low noise, it is not possible to resolve the gap oscillations that were predicted.

It is possible that the couplings that were measured and calculated in Section 5.2 are an overestimation of their actual values, if the vacancies indeed couple in a tight-binding way, and that consequently the gap is smaller than expected. In that case, even if we manage to increase the energy resolution and sensitivity of our measurement, it might not yet be possible to see the oscillation. This chlorine terminated copper (100) substrate is therefore unlikely to be a good substrate for building artificial molecules, but similar surfaces with a different termination, e.g. bromine or iodine on copper, that also exhibit vacancies, might be better candidates for this endeavour.

MEASURING THE LOCAL ELECTRIC FIELD WITH STM

We observe a resonance in some of the $\mathrm{d}I/\mathrm{d}V$ spectra taken on the unsaturated copper chloride surface, leading in some cases to a negative differential resistance (NDR). This can be explained by the resonance of a state of a quantum dot located on or near the apex of our STM tip. A chlorine atom, weakly coupled to the tip, can lead to a situation with a double tunnel barrier, thus giving rise to the observed QD-like behaviour. The voltage V_R, at which the resonance occurs, shifts to lower values with decreasing tip height

and when the tip is positioned over vacancies in the Cu_2Cl surface. This observation is consistent with a dependence of the QD on the experienced electric field.

Line cuts of $\mathrm{d}I/\mathrm{d}V$ spectra were made over structures made from vacancies arranged in square $N \times N$ patches, to compare the behaviour over bare Cu with that over Cl. For small ($N \leq 5$) patches, the resonance voltage V_R shifts to lower values for larger N without levelling off, but for 11×11 copper patches they do level off inside the patch, suggesting that the quantum dot on the tip feels the electric field of the boundary up to $2a \approx 0.7$ nm away.

Because the sample geometry and thus charge distribution influences the behaviour of the resonance, we simulated the electric field of vacancy patches of various sizes using a simple image charge model, with one electron charge per Cl atom and using the Cu substrate as the conductor. This provides the electric field in three directions as a function of tip position over the area. We compare $\mathrm{d}I/\mathrm{d}V$ line cuts over copper patches of different sizes with the simulations, to find for which height the simulation matches the measurement best. The quantum dot seems to be mostly sensitive to the z component, and this simple model reproduces the qualitative behaviour of the resonances as it crosses the copper patch at a height of ~0.5 nm.

In some cases, two distinctly behaving resonances can be seen, indicating that there are two different quantum dots on or near our tip apex. By comparing the resonance voltage curves for different line cuts over a copper patch, the horizontal displacement can be estimated. Curves at different set-point currents give us an indication for the height difference, telling us the relative distance of the two quantum dots on our tip.

We compared the resonant behaviour between the copper and the chlorine by taking constant-height $\mathrm{d}I/\mathrm{d}V$ spectra on set-point currents from 20 pA to 90 nA. Two resonances are seen, where we can estimate the height difference by shifting the curves until they align. We use the absolute height to calculate both the tip and the sample contribution to the electric field, and plot the resonance voltage versus the experienced electric field $E_{tot}(z) = E_t + c \cdot E_s = V/z + c \cdot E_z(z)$, with c a fitting parameter for the simulated sample field $E_z(z)$. We expect the resonance voltage to be a single continuous curve as a function of the experienced electric field, analogous to Coulomb diamonds in a gated transport measurement. In this case, the combination of changing tip height and sample field would lead to an effective electric field applied to the QD on our tip, thus forming a way to gate the system. For $c = 0.27$, the resonances align to a single curve, suggesting that only 0.27 electrons are present per chlorine ion, which is not in agreement with the ionic bond that Cl forms with the Cu substrate. Instead, the approximations used in the model are discussed, showing how small changes in charge q, dipole distance d, and height z can partially account for the quantitative disparity, without compromising the qualitative agreement of our model with the measurements.

In conclusion, we observe resonance-like features in a number of our differential conductance spectra, sometimes leading to NDR. We explain this by the presence of a quantum dot – for instance a weakly bound chlorine atom – on the apex of our STM tip, causing a resonance at varying bias voltages for varying local effective electric fields. The quantum dot is gated by a combination of the tip height and the local surface charge distribution. The existence of multiple resonances can point to multiple quantum dots, of which the relative position is discussed, using vacancy structures of various shapes and

sizes. A simulation of the electric field due to the sample gives a qualitative agreement with the experiment, indicating that once the quantitative behaviour of the quantum dot is known, the system can be used to probe the local electric field distribution of unknown structures.

TRANSITION METAL ATOMS ON COPPER CHLORIDE

We evaporated the transition metal atoms silver, nickel and iron on the copper chloride surface, to investigate their magnetic behaviour. We found that silver atoms mainly adsorb in bridge positions and on chloride vacancies, while nickel adatoms mostly appear with a distorted non-circular shape: square in the hollow sites, and oval shapes on top of a Cl atom or a vacancy. Both silver and nickel do not show signs of inelastic tunnelling events, and are non-magnetic on this surface.

Iron appears in hollow and Cl positions and on vacancies as a triangle pointed in one of the four neighbouring atoms. The adatoms in hollow sites show some steps in their differential conductance spectra, which seem to shift slightly when an out-of-plane field of up to 9 T is applied. Although this is an indication that Fe atoms adsorbed on Cu_2Cl hollow sites might indeed be magnetic, more work needs to be done to verify this finding. The effect is relatively weak, so stronger tools to observe this are needed: higher fields and lower temperatures. It might be worthwhile to further scrutinize the atoms in other adsorption sites, especially if they can be manipulated to exact known locations. Once the properties for single adatoms are known, combinations of two or more can be invesigated, for example, for tuning the local magnetocrystalline anisotropy [27].

Incidentally, it was possible to manipulate atoms, although not yet reliably so. We used this in Figure 7.2 to prove that some of the silver adatoms indeed lie on a vacancy. Considering the success of vertical manipulation techniques on Cu_2N [35, 76], it seems very plausible that the same techniques might be tailored to this surface as well, since the nitride reconstruction is similar to our chloride reconstruction.

Combined with the vacancy manipulation introduced in Chapter 2 and the large terraces of uninterrupted, clean substrate, it might be possible to construct large structures where magnetic atoms are coupled to each other – or even to vacancies – over long distances, thus providing an entirely new template for future engineering.

BIBLIOGRAPHY

[1] G. Binnig and H. Rohrer, *Scanning tunneling microscopy,* Surface Science **126**, 236 (1983).

[2] G. K. Binnig and H. Rohrer, *US Patent US4343993A: Scanning Tunneling Microscope,* (1982).

[3] P. D. B. Parolo, R. K. Pan, F. Becattini, M. Mitrovic, A. Chatterjee, and S. Fortunato, *The Nobel Prize delay,* Physics Today (2014), 10.1063/PT.5.2012.

[4] G. Binnig, C. F. Quate, and C. Gerber, *Atomic Force Microscope,* Physical Review Letters **56**, 930 (1986).

[5] G. K. Binnig, *US Patent US4724318A: Atomic Force Microscope and method for imaging surfaces with atomic resolution,* (1988).

[6] R. P. Feynman, *There's Plenty of Room at the Bottom,* Engineering and Science **23**, 22 (1960).

[7] F. J. Giessibl, *Advances in atomic force microscopy,* Reviews of Modern Physics **75**, 949 (2003).

[8] L. Gross, F. Mohn, N. Moll, P. Liljeroth, and G. Meyer, *The Chemical Structure of a Molecule Resolved by Atomic Force Microscopy,* Science **325**, 1110 (2009).

[9] M. Nonnenmacher, M. P. O'Boyle, and H. K. Wickramasinghe, *Kelvin probe force microscopy,* Applied Physics Letters **58**, 2921 (1991).

[10] H. O. Jacobs, P. Leuchtmann, O. J. Homan, and A. Stemmer, *Resolution and contrast in Kelvin probe force microscopy,* Journal of Applied Physics **84**, 1168 (1998).

[11] W. Melitz, J. Shen, A. C. Kummel, and S. Lee, *Kelvin probe force microscopy and its application,* Surface Science Reports **66**, 1 (2011).

[12] J. R. Kirtley and J. P. Wikswo, *Scanning SQUID microscopy,* Annual Review of Materials Science **29**, 117 (1999).

[13] J. A. Sidles, J. L. Garbini, K. J. Bruland, D. Rugar, O. Züger, S. Hoen, and C. S. Yannoni, *Magnetic resonance force microscopy,* Reviews of Modern Physics **67**, 249 (1995).

[14] D. Rugar, R. Budakian, H. J. Mamin, and B. W. Chui, *Single spin detection by magnetic resonance force microscopy,* Nature **430**, 329 (2004).

[15] D. Mounce, *Magnetic resonance force microscopy,* IEEE Instrumentation & Measurement Magazine **8**, 20 (2005).

[16] D. M. Eigler and E. K. Schweizer, *Positioning single atoms with a scanning tunnelling microscope,* Nature **344**, 524 (1990).

[17] A. J. Heinrich, J. A. Gupta, C. P. Lutz, and D. M. Eigler, *Single-Atom Spin-Flip Spectroscopy,* Science **306**, 466 (2004).

[18] A. F. Otte, *Magnetism of a Single Atom*, Ph.D. thesis, Universiteit Leiden (2008).

[19] C. F. Hirjibehedin, C. P. Lutz, and A. J. Heinrich, *Spin coupling in engineered atomic structures.* Science **312**, 1021 (2006).

[20] C. F. Hirjibehedin, C.-Y. Lin, A. F. Otte, M. Ternes, C. P. Lutz, B. a. Jones, and A. J. Heinrich, *Large Magnetic Anisotropy of a Single Atomic Spin Embedded in a Surface Molecular Network,* Science **317**, 1199 (2007).

[21] A. F. Otte, M. Ternes, S. Loth, C. P. Lutz, C. F. Hirjibehedin, and A. J. Heinrich, *Spin Excitations of a Kondo-Screened Atom Coupled to a Second Magnetic Atom,* Physical Review Letters **103**, 107203 (2009).

[22] H. Brune and P. Gambardella, *Magnetism of individual atoms adsorbed on surfaces,* Surface Science **603**, 1812 (2009).

[23] S. Schintke and W.-D. Schneider, *Insulators at the ultrathin limit: electronic structure studied by scanning tunnelling microscopy and scanning tunnelling spectroscopy,* Journal of Physics: Condensed Matter **16**, R49 (2004).

[24] I. G. Rau, S. Baumann, S. Rusponi, F. Donati, S. Stepanow, L. Gragnaniello, J. Dreiser, C. Piamonteze, F. Nolting, S. Gangopadhyay, O. R. Albertini, R. M. Macfarlane, C. P. Lutz, B. a. Jones, P. Gambardella, A. J. Heinrich, and H. Brune, *Reaching the magnetic anisotropy limit of a 3d metal atom,* Science **344**, 988 (2014).

[25] J. Repp, G. Meyer, F. E. Olsson, and M. Persson, *Controlling the Charge State of Individual Gold Adatoms,* Science **305**, 493 (2004).

[26] A. F. Otte, M. Ternes, K. von Bergmann, S. Loth, H. Brune, C. P. Lutz, C. F. Hirjibehedin, and A. J. Heinrich, *The role of magnetic anisotropy in the Kondo effect,* Nature Physics **4**, 847 (2008).

[27] B. Bryant, A. Spinelli, J. J. T. Wagenaar, M. Gerrits, and a. F. Otte, *Local Control of Single Atom Magnetocrystalline Anisotropy,* Physical Review Letters **111**, 127203 (2013).

[28] J. C. Oberg, M. R. Calvo, F. Delgado, M. Moro-Lagares, D. Serrate, D. Jacob, J. Fernández-Rossier, and C. F. Hirjibehedin, *Control of single-spin magnetic anisotropy by exchange coupling.* Nature nanotechnology **9**, 64 (2014).

[29] A. A. Khajetoorians, J. Wiebe, B. Chilian, and R. Wiesendanger, *Realizing all-spin-based logic operations atom by atom.* Science **332**, 1062 (2011).

[30] A. A. Khajetoorians, J. Wiebe, B. Chilian, S. Lounis, S. Blügel, and R. Wiesendanger, *Atom-by-atom engineering and magnetometry of tailored nanomagnets,* Nature Physics **8**, 497 (2012).

[31] S. Loth, S. Baumann, C. P. Lutz, D. M. Eigler, and A. J. Heinrich, *Bistability in Atomic-Scale Antiferromagnets,* Science **335**, 196 (2012).

[32] A. A. Khajetoorians, B. Baxevanis, C. Hübner, T. Schlenk, and S. Krause, *Current-Driven Spin Dynamics,* Science **339**, 55 (2013).

[33] B. Bryant, R. Toskovic, A. Ferrón, J. L. Lado, A. Spinelli, J. Fernández-Rossier, and A. F. Otte, *Controlled Complete Suppression of Single-Atom Inelastic Spin and Orbital Cotunneling,* Nano Letters **15**, 6542 (2015).

[34] A. Spinelli, M. P. Rebergen, and A. F. Otte, *Atomically crafted spin lattices as model systems for quantum magnetism,* Journal of Physics: Condensed Matter **27**, 243203 (2015).

[35] R. Toskovic, R. van den Berg, A. Spinelli, I. S. Eliens, B. van den Toorn, B. Bryant, J.-S. Caux, and A. F. Otte, *Atomic spin-chain realization of a model for quantum criticality,* Nature Physics **12**, 656 (2016).

[36] F. Donati, S. Rusponi, S. Stepanow, C. Wackerlin, A. Singha, L. Persichetti, R. Baltic, K. Diller, F. Patthey, E. Fernandes, J. Dreiser, . Ljivan anin, K. Kummer, C. Nistor, P. Gambardella, and H. Brune, *Magnetic remanence in single atoms,* Science **352**, 318 (2016).

[37] F. D. Natterer, K. Yang, W. Paul, P. Willke, T. Choi, T. Greber, A. J. Heinrich, and C. P. Lutz, *Reading and writing single-atom magnets,* Nature **543**, 226 (2017).

[38] R. Wiesendanger, *Spin mapping at the nanoscale and atomic scale,* Reviews of Modern Physics **81**, 1495 (2009).

[39] S. Baumann, W. Paul, T. Choi, C. P. Lutz, A. Ardavan, and A. J. Heinrich, *Electron paramagnetic resonance of individual atoms on a surface,* Science **350**, 417 (2015).

[40] W. Paul, S. Baumann, C. P. Lutz, and A. J. Heinrich, *Generation of constant-amplitude radio-frequency sweeps at a tunnel junction for spin resonance STM,* Review of Scientific Instruments **87**, 074703 (2016).

[41] J. L. Lado, A. Ferrón, and J. Fernández-Rossier, *Exchange mechanism for electron paramagnetic resonance of individual adatoms,* Physical Review B **96**, 205420 (2017).

[42] F. E. Kalff, M. P. Rebergen, E. Fahrenfort, J. Girovsky, R. Toskovic, J. L. Lado, J. Fernández-Rossier, and A. F. Otte, *A kilobyte rewritable atomic memory,* Nature Nanotechnology **11**, 926 (2016).

[43] J. Girovsky, J. L. Lado, F. E. Kalff, E. Fahrenfort, L. J. J. M. Peters, J. Fernández-Rossier, and A. F. Otte, *Emergence of quasiparticle Bloch states in artificial crystals crafted atom-by-atom,* SciPost Physics **2**, 020 (2017).

[44] M. F. Crommie, C. P. Lutz, and D. M. Eigler, *Confinement of Electrons to Quantum Corrals on a Metal Surface,* Science **262**, 218 (1993).

[45] A. J. Heinrich, C. P. Lutz, J. A. Gupta, and D. M. Eigler, *Molecule Cascades,* Science **298**, 1381 (2002).

[46] P. Ebert, M. G. Lagally, and K. Urban, *Scanning-tunneling-microscope tip-induced migration of vacancies on GaP(110),* Physical Review Letters **70**, 1437 (1993).

[47] B. Schuler, M. Persson, S. Paavilainen, N. Pavlicek, L. Gross, G. Meyer, and J. Repp, *Effect of electron-phonon interaction on the formation of one-dimensional electronic states in coupled Cl vacancies,* Physical Review B **91**, 235443 (2015).

[48] Z. Li, H.-Y. T. Chen, K. Schouteden, K. Lauwaet, E. Janssens, C. Van Haesendonck, G. Pacchioni, and P. Lievens, *Lateral Manipulation of Atomic Vacancies in Ultrathin Insulating Films,* ACS Nano **9**, 5318 (2015).

[49] C. Nakakura, G. Zheng, and E. Altman, *Atomic-scale mechanisms of the halogenation of Cu(100),* Surface Science **401**, 173 (1998).

[50] S. Huemann, N. T. M. Hai, P. Broekmann, K. Wandelt, H. Zajonz, H. Dosch, and F. Renner, *X-ray diffraction and STM study of reactive surfaces under electrochemical control: Cl and I on Cu(100),* Journal of Physical Chemistry B **110**, 24955 (2006).

[51] A. Migani and F. Illas, *A Systematic Study of the Structure and Bonding of Halogens on Low-Index Transition Metal Surfaces,* The Journal of Physical Chemistry B **110**, 11894 (2006).

[52] I. A. Suleiman, M. W. Radny, M. J. Gladys, P. V. Smith, J. C. Mackie, E. M. Kennedy, and B. Z. Dlugogorski, *Interaction of Chlorine and Oxygen with the Cu(100) Surface,* The Journal of Physical Chemistry C **114**, 19048 (2010).

[53] H. C. Tolentino, M. De Santis, Y. Gauthier, and V. Langlais, *Chlorine chemisorption on Cu(001) by surface X-ray diffraction: Geometry and substrate relaxation,* Surface Science **601**, 2962 (2007).

[54] I. A. Suleiman, M. W. Radny, M. J. Gladys, P. V. Smith, J. C. Mackie, E. M. Kennedy, and B. Z. Dlugogorski, *An equilibrium ab initio atomistic thermodynamics study of chlorine adsorption on the Cu(001) surface,* Physical Chemistry Chemical Physics **13**, 10306 (2011).

[55] J. Nowakowski, S. Nowakowska, G. Srivastava, M. Baljozovic, J. Girovsky, N. Ballav, and T. A. Jung, *Probing the Reactivity of Functionalized Surfaces by Porphyrin Metalation,* ChemistrySelect **1**, 891 (2016).

[56] G. Binnig, H. Rohrer, C. Gerber, and E. Weibel, *Surface Studies by Scanning Tunneling Microscopy,* Physical Review Letters **49**, 57 (1982).

[57] G. Binnig, H. Rohrer, C. Gerber, and E. Weibel, *Tunneling through a controllable vacuum gap,* Applied Physics Letters **40**, 178 (1982).

[58] A. Spinelli, *Quantum magnetism through atomic assembly*, Ph.D. thesis, Technische Universiteit Delft (2015).

[59] F. Besenbacher, *Scanning tunnelling microscopy studies of metal surfaces,* Reports on Progress in Physics **59**, 1737 (1999).

[60] M. Seah, *Pure element sputtering yields using 500–1000 eV argon ions,* Thin Solid Films **81**, 279 (1981).

[61] A. L. Southern, W. R. Willis, and M. T. Robinson, *Sputtering Experiments with 1- to 5-keV Ar+ Ions,* Journal of Applied Physics **34**, 153 (1963).

[62] N. Laegreid and G. K. Wehner, *Sputtering Yields of Metals for Ar+ and Ne+ Ions with Energies from 50 to 600 eV,* Journal of Applied Physics **32**, 365 (1961).

[63] M. Ritter, M. Stindtmann, M. Farle, and K. Baberschke, *Nanostructuring of the Cu(001) surface by ion bombardment: a STM study,* Surface Science **348**, 243 (1996).

[64] R. Lee and H. Farnsworth, *LEED studies of adsorption on clean (100) copper surfaces,* Surface Science **3**, 461 (1965).

[65] K. Motai, T. Hashizume, H. Lu, D. Jeon, T. Sakurai, and H. Pickering, *STM of the Cu(111)1 × 1 surface and its exposure to chlorine and sulfur,* Applied Surface Science **67**, 246 (1993).

[66] R. Toskovic, M. C. Martinez Velarte, J. Girovsky, M. Kokken, F. González, F. Delgado, and A. F. Otte, *Orbital-specificity in probing inelastic excitations in single Co adatoms on Cl-reconstructed Cu(111),* manuscript in preparation .

[67] R. G. Jones, *Halogen adsorption on solid surfaces,* Progress in Surface Science **27**, 25 (1988).

[68] C. Nakakura and E. Altman, *Scanning tunneling microscopy study of the reaction of Br$_2$ with Cu(100),* Surface Science **398**, 281 (1998).

[69] B. V. Andryushechkin, K. N. Eltsov, V. M. Shevlyuga, U. Bardi, and B. Cortigiani, *Structural transitions of chemisorbed iodine on Cu(100),* Surface Science **497**, 59 (2002).

[70] B. V. Andryushechkin, K. N. El'tsov, and V. M. Shevlyuga, *Scanning tunneling microscopy of 'commensurate – incommensurate' structural phase transitions in the chemisorbed layers of halogens,* Physics-Uspekhi **43**, 527 (2000).

[71] B. V. Andryushechkin, V. V. Zheltov, V. V. Cherkez, G. M. Zhidomirov, A. N. Klimov, B. Kierren, Y. Fagot-Revurat, D. Malterre, and K. N. Eltsov, *Chlorine adsorption on Cu(111) revisited: LT-STM and DFT study,* Surface Science **639**, 7 (2015).

[72] P. Goddard and R. Lambert, *Adsorption-desorption properties and surface structural chemistry of chlorine on Cu(111) and Ag(111),* Surface Science **67**, 180 (1977).

[73] A. F. Carley, P. R. Davies, K. R. Harikumar, and R. V. Jones, *A low energy pathway to CuCl2 at Cu(110) surfaces,* Physical Chemistry Chemical Physics **11**, 10899 (2009).

[74] V. V. Cherkez, V. V. Zheltov, C. Didiot, B. Kierren, Y. Fagot-Revurat, D. Malterre, B. V. Andryushechkin, G. M. Zhidomirov, and K. N. Eltsov, *Self-ordered nanoporous lattice formed by chlorine atoms on Au(111),* Physical Review B **93**, 045432 (2016).

[75] J. Inukai, Y. Osawa, and K. Itaya, *Adlayer Structures of Chlorine, Bromine, and Iodine on Cu(111) Electrode in Solution: In-Situ STM and ex-Situ LEED Studies,* The Journal of Physical Chemistry B **102**, 10034 (1998).

[76] A. Spinelli, B. Bryant, F. Delgado, J. Fernández-Rossier, and A. F. Otte, *Imaging of spin waves in atomically designed nanomagnets,* Nature Materials **13**, 782 (2014).

[77] A. A. Khajetoorians, T. Schlenk, B. Schweflinghaus, M. dos Santos Dias, M. Steinbrecher, M. Bouhassoune, S. Lounis, J. Wiebe, and R. Wiesendanger, *Spin Excitations of Individual Fe Atoms on Pt(111): Impact of the Site-Dependent Giant Substrate Polarization,* Physical Review Letters **111**, 157204 (2013).

[78] F. M. Leibsle, C. F. J. Flipse, and A. W. Robinson, *Structure of the Cu{100}- c (2×2)N surface: A scanning-tunneling-microscopy study,* Physical Review B **47**, 15865 (1993).

[79] D. M. Eigler, C. P. Lutz, and W. E. Rudge, *An atomic switch realized with the scanning tunnelling microscope,* Nature **352**, 600 (1991).

[80] M. Brandbyge and P. Hedegård, *Theory of the Eigler switch,* Physical Review Letters **72**, 2919 (1994).

[81] S.-W. Hla, *Scanning tunneling microscopy single atom/molecule manipulation and its application to nanoscience and technology,* Journal of Vacuum Science & Technology B: Microelectronics and Nanometer Structures **23**, 1351 (2005).

[82] C. Ghosh, A. Kara, and T. S. Rahman, *Theoretical aspects of vertical and lateral manipulation of atoms,* Surface Science **502-503**, 519 (2002).

[83] S. Hosoki, S. Hosaka, and T. Hasegawa, *Surface modification of MoS2 using an STM,* Applied Surface Science **60-61**, 643 (1992).

[84] J. Repp, G. Meyer, S. Paavilainen, F. E. Olsson, and M. Persson, *Scanning tunneling spectroscopy of Cl vacancies in NaCl films: Strong electron-phonon coupling in double-barrier tunneling junctions,* Physical Review Letters **95**, 1 (2005).

[85] R. M. Tromp, *Spectroscopy with the scanning tunnelling microscope: a critical review,* Journal of Physics: Condensed Matter **1**, 10211 (1989).

[86] T. Roman and A. Groß, *Periodic Density-Functional Calculations on Work-Function Change Induced by Adsorption of Halogens on Cu(111),* Physical Review Letters **110**, 156804 (2013).

[87] C. D. Ruggiero, T. Choi, and J. A. Gupta, *Tunneling spectroscopy of ultrathin insulating films: CuN on Cu(100),* Applied Physics Letters **91**, 253106 (2007).

[88] L. Rademaker, Y. Pramudya, J. Zaanen, and V. Dobrosavljević, *Influence of long-range interactions on charge ordering phenomena on a square lattice,* Physical Review E **88**, 032121 (2013).

[89] P. Giannozzi, S. Baroni, N. Bonini, M. Calandra, R. Car, C. Cavazzoni, D. Ceresoli, G. L. Chiarotti, M. Cococcioni, I. Dabo, A. Dal Corso, S. de Gironcoli, S. Fabris, G. Fratesi, R. Gebauer, U. Gerstmann, C. Gougoussis, A. Kokalj, M. Lazzeri, L. Martin-Samos, N. Marzari, F. Mauri, R. Mazzarello, S. Paolini, A. Pasquarello, L. Paulatto, C. Sbraccia, S. Scandolo, G. Sclauzero, A. P. Seitsonen, A. Smogunov, P. Umari, and R. M. Wentzcovitch, *QUANTUM ESPRESSO: a modular and open-source software project for quantum simulations of materials,* Journal of Physics: Condensed Matter **21**, 395502 (2009).

[90] M. Fuechsle and S. Mahapatra, *Spectroscopy of few-electron single-crystal silicon quantum dots,* Nature Nanotechnology **5**, 502 (2010).

[91] J. R. Maze, P. L. Stanwix, J. S. Hodges, S. Hong, J. M. Taylor, P. Cappellaro, L. Jiang, M. V. Dutt, E. Togan, A. S. Zibrov, A. Yacoby, R. L. Walsworth, and M. D. Lukin, *Nanoscale magnetic sensing with an individual electronic spin in diamond,* Nature **455**, 644 (2008).

[92] G. Balasubramanian, I. Y. Chan, R. Kolesov, M. Al-Hmoud, J. Tisler, C. Shin, C. Kim, A. Wojcik, P. R. Hemmer, A. Krueger, T. Hanke, A. Leitenstorfer, R. Bratschitsch, F. Jelezko, and J. Wrachtrup, *Nanoscale imaging magnetometry with diamond spins under ambient conditions,* Nature **455**, 648 (2008).

[93] C. Schirm, M. Matt, F. Pauly, J. C. Cuevas, P. Nielaba, and E. Scheer, *A current-driven single-atom memory,* Nature Nanotechnology **8**, 645 (2013).

[94] D. Eom, C. Y. Moon, and J. Y. Koo, *Switching the charge state of individual surface atoms at Si(111)-3x3:B surfaces,* Nano Letters **15**, 398 (2015).

[95] R. Bennewitz, J. N. Crain, A. Kirakosian, J.-L. Lin, J. L. McChesney, D. Y. Petrovykh, and F. J. Himpsel, *Atomic scale memory at a silicon surface,* Nanotechnology **13**, 312 (2002).

[96] R. J. Celotta, S. B. Balakirsky, A. P. Fein, F. M. Hess, G. M. Rutter, and J. A. Stroscio, *Invited Article: Autonomous assembly of atomically perfect nanostructures using a scanning tunneling microscope,* Review of Scientific Instruments **85**, 121301 (2014).

[97] H. W. Kuhn, *The Hungarian method for the assignment problem,* Naval Research Logistics Quarterly **2**, 83 (1955).

[98] J. Munkres, *Algorithms for the Assignment and Transportation Problems,* Journal of the Society for Industrial and Applied Mathematics **5**, 32 (1957).

[99] P. Hart, N. Nilsson, and B. Raphael, *A Formal Basis for the Heuristic Determination of Minimum Cost Paths,* IEEE Transactions on Systems Science and Cybernetics **4**, 100 (1968).

[100] M. J. Rost, L. Crama, P. Schakel, E. Van Tol, G. B. E. M. Van Velzen-Williams, C. F. Overgauw, H. Ter Horst, H. Dekker, B. Okhuijsen, M. Seynen, A. Vijftigschild, P. Han, A. J. Katan, K. Schoots, R. Schumm, W. Van Loo, T. H. Oosterkamp, and J. W. M. Frenken, *Scanning probe microscopes go video rate and beyond,* Review of Scientific Instruments **76**, 1 (2005).

[101] P. Vettiger, M. Despont, U. Drechsler, U. Durig, W. Haberle, M. I. Lutwyche, H. E. Rothuizen, R. Stutz, R. Widmer, and G. K. Binnig, *The "Millipede"—More than thousand tips for future AFM storage,* IBM Journal of Research and Development **44**, 323 (2000).

[102] C. R. Darwin, *On the Origin of Species by Means of Natural Selection, or the Preservation of Favoured Races in the Struggle for Life.*, 5th ed. (John Murray, London, 1869).

[103] J. A. Stroscio and D. M. Eigler, *Atomic and Molecular Manipulation with the Scanning Tunneling Microscope,* Science **254**, 1319 (1991).

[104] L. Venema, B. Verberck, I. Georgescu, G. Prando, E. Couderc, S. Milana, M. Maragkou, L. Persechini, G. Pacchioni, and L. Fleet, *The quasiparticle zoo,* Nature Physics **12**, 1085 (2016).

[105] K. K. Gomes, W. Mar, W. Ko, F. Guinea, and H. C. Manoharan, *Designer Dirac fermions and topological phases in molecular graphene,* Nature **483**, 306 (2012).

[106] Y. Pennec, W. Auwärter, A. Schiffrin, A. Weber-Bargioni, A. Riemann, and J. V. Barth, *Supramolecular gratings for tuneable confinement of electrons on metal surfaces,* Nature Nanotechnology **2**, 99 (2007).

[107] M. R. Slot, T. S. Gardenier, P. H. Jacobse, G. C. P. van Miert, S. N. Kempkes, S. J. M. Zevenhuizen, C. M. Smith, D. Vanmaekelbergh, and I. Swart, *Experimental realization and characterization of an electronic Lieb lattice,* Nature Physics **13**, 672 (2017).

[108] N. Nilius, *Development of One-Dimensional Band Structure in Artificial Gold Chains,* Science **297**, 1853 (2002).

[109] J. Lobo-Checa, M. Matena, K. Müller, J. H. Dil, F. Meier, L. H. Gade, T. a. Jung, and M. Stöhr, *Band formation from coupled quantum dots formed by a nanoporous network on a copper surface.* Science **325**, 300 (2009).

[110] F. Klappenberger, D. Kühne, W. Krenner, I. Silanes, A. Arnau, F. De Javier García Abajo, S. Klyatskaya, M. Ruben, and J. V. Barth, *Dichotomous array of chiral quantum corrals by a self-assembled nanoporous kagomé network,* Nano Letters **9**, 3509 (2009).

[111] S. R. Schofield, P. Studer, C. F. Hirjibehedin, N. J. Curson, G. Aeppli, and D. R. Bowler, *Quantum engineering at the silicon surface using dangling bonds,* Nature Communications **4**, 1649 (2013).

[112] R. Drost, T. Ojanen, A. Harju, and P. Liljeroth, *Topological states in engineered atomic lattices,* Nature Physics **13**, 668 (2017).

[113] R. Korytár, D. Xenioti, P. Schmitteckert, M. Alouani, and F. Evers, *Signature of the Dirac cone in the properties of linear oligoacenes,* Nature Communications **5**, 5000 (2014).

[114] S. S. Zade and M. Bendikov, *Heptacene and Beyond: The Longest Characterized Acenes,* Angewandte Chemie International Edition **49**, 4012 (2010).

[115] C. Kittel, *Introduction to Solid State Physics*, 8th ed. (John Wiley & Sons, Inc., 2005).

[116] N. W. Ashcroft and N. D. Mermin, *Solid State Physics* (Brooks/Cole, Belmont, CA, USA, 1976).

[117] A. H. Castro Neto, F. Guinea, N. M. R. Peres, K. S. Novoselov, and A. K. Geim, *The electronic properties of graphene,* Reviews of Modern Physics **81**, 109 (2009).

[118] D. Moldovan, M. Anđelković, and F. Peeters, *pybinding v0.9.4: a Python package for tight-binding calculations,* (2017).

[119] S. Kivelson and O. L. Chapman, *Polyacene and a new class of quasi-one-dimensional conductors,* Physical Review B **28**, 7236 (1983).

[120] S. W. Wu, G. V. Nazin, X. Chen, X. H. Qiu, and W. Ho, *Control of Relative Tunneling Rates in Single Molecule Bipolar Electron Transport,* Physical Review Letters **93**, 236802 (2004).

[121] G. Mikaelian, N. Ogawa, X. W. Tu, and W. Ho, *Atomic scale control of single molecule charging,* The Journal of Chemical Physics **124**, 131101 (2006).

[122] I. Fernández-Torrente, D. Kreikemeyer-Lorenzo, A. Stróżecka, K. J. Franke, and J. I. Pascual, *Gating the Charge State of Single Molecules by Local Electric Fields,* Physical Review Letters **108**, 036801 (2012).

[123] S. Karan, D. Jacob, M. Karolak, C. Hamann, Y. Wang, A. Weismann, A. I. Lichtenstein, and R. Berndt, *Shifting the Voltage Drop in Electron Transport Through a Single Molecule,* Physical Review Letters **115**, 016802 (2015).

[124] B. Warner, F. El Hallak, H. Prüser, J. Sharp, M. Persson, A. J. Fisher, and C. F. Hirjibehedin, *Tunable magnetoresistance in an asymmetrically coupled single-molecule junction,* Nature Nanotechnology **10**, 259 (2015).

[125] S. Rolf-Pissarczyk, S. Yan, L. Malavolti, J. A. J. Burgess, G. McMurtrie, and S. Loth, *Dynamical Negative Differential Resistance in Antiferromagnetically Coupled Few-Atom Spin Chains,* Physical Review Letters **119**, 217201 (2017).

[126] M. A. Kastner, *Artificial Atoms,* Physics Today **46**, 24 (1993).

[127] R. C. Ashoori, *Electrons in artificial atoms,* Nature **379**, 413 (1996).

[128] Wikipedia contributors, , *Quantum dot — Wikipedia, The Free Encyclopedia,* (2018).

[129] L. P. Kouwenhoven, D. G. Austing, and S. Taruch, *Time-dependent single-electron transport through quantum dots,* Reports on Progress in Physics **64**, 701 (2001).

[130] C. Wagner, M. F. B. Green, P. Leinen, T. Deilmann, P. Krüger, M. Rohlfing, R. Temirov, and F. S. Tautz, *Scanning Quantum Dot Microscopy,* Physical Review Letters **115**, 026101 (2015).

[131] H. Sellier, B. Hackens, M. G. Pala, F. Martins, S. Baltazar, X. Wallart, L. Desplanque, V. Bayot, and S. Huant, *On the imaging of electron transport in semiconductor quantum structures by scanning-gate microscopy: successes and limitations,* Semiconductor Science and Technology **26**, 064008 (2011).

[132] C. Schönenberger and S. F. Alvarado, *Observation of single charge carriers by force microscopy,* Physical Review Letters **65**, 3162 (1990).

[133] C. Girard, C. Joachim, C. Chavy, and P. Sautet, *The electric field under a STM tip apex: implications for adsorbate manipulation,* Surface Science **282**, 400 (1993).

[134] D. J. Griffiths, *Introduction to Electrodynamics*, 3rd ed. (Pearson Benjamin Cummings, San Francisco, CA, USA, 2008).

[135] M. T. Koper, *A lattice-gas model for halide adsorption on single-crystal electrodes,* Journal of Electroanalytical Chemistry **450**, 189 (1998).

[136] L. G. M. Pettersson and P. S. Bagus, *Adsorbate ionicity and surface-dipole-moment changes: Cluster-model studies of Cl/Cu(100) and F/Cu(100),* Physical Review Letters **56**, 500 (1986).

[137] A. Ferrón, J. L. Lado, and J. Fernández-Rossier, *Electronic properties of transition metal atoms on Cu$_2$N/Cu(100),* Physical Review B **92**, 174407 (2015).

[138] D. Coffey Blanco, *Rare earth adatoms and nanoislands studied by Scanning Tunnelling Microscopy*, Ph.D. thesis, Universidad Zaragoza (2016).

[139] J. Lambe and R. C. Jaklevic, *Molecular Vibration Spectra by Inelastic Electron Tunneling,* Physical Review **165**, 821 (1968).

[140] B. C. Stipe, M. A. Rezaei, and W. Ho, *Single-Molecule Vibrational Spectroscopy and Microscopy,* Science **280**, 1732 (1998).

[141] R. H. M. Smit, Y. Noat, C. Untiedt, N. D. Lang, M. C. van Hemert, and J. M. van Ruitenbeek, *Measurement of the conductance of a hydrogen molecule,* Nature **419**, 906 (2002).

[142] S. Baumann, F. Donati, S. Stepanow, S. Rusponi, W. Paul, S. Gangopadhyay, I. G. Rau, G. E. Pacchioni, L. Gragnaniello, M. Pivetta, J. Dreiser, C. Piamonteze, C. P. Lutz, R. M. Macfarlane, B. A. Jones, P. Gambardella, A. J. Heinrich, and H. Brune, *Origin of Perpendicular Magnetic Anisotropy and Large Orbital Moment in Fe Atoms on MgO,* Physical Review Letters **115**, 237202 (2015).

SUMMARY

In this thesis, a technique is developed to manipulate individual atoms on an ionic surface, with great precision and at a large scale, to study the quantum mechanical properties of atomic assemblies on the nanoscale. The scanning tunnelling microscope (STM) is our method of choice, where the scanning motion of an ultra-thin needle over an atomically flat surface allows us to observe the individual atoms making up structures in our surface, making use of the tunnel current between tip and sample. By varying the applied bias voltage and measuring the tunnel current, the local density of states can be determined, which gives us information about the electronic states at the position of the needle, a powerful tool called scanning tunnelling spectroscopy (STS).

To manipulate atoms, we used a chlorine terminated copper surface. By evaporating $CuCl_2$ powder, a salt, onto a clean, atomically flat Cu(100) crystal, the chlorine atoms bind ionically with the copper atoms, forming a square c(2 × 2)R45° reconstruction, denoted as the Cu_2Cl surface. When the amount evaporated is insufficient to form a complete chlorine monolayer, the missing chlorine atoms appear as single defects in the Cu_2Cl/Cu(100) layer: square depressions appearing 20-50 pm deep that we call *vacancies*. The vacancy coverage after preparation of a surface can be controlled by the evaporation time.

By approaching a vacancy with the STM tip such that the tunnel current ramps up to the μA range, it is found that a neighbouring Cl atom can jump to the vacancy position, effectively moving the vacancy in the inverse direction. In Chapter 2, a method to precisely manipulate vacancies is developed: by controlling the tip height with feedback on the current, placing the tip with a slight asymmetry between vacancy and neighbouring Cl atom, reliabilities of sometimes over 99 % can be reached. This technique is robust to small variations in tip-sample distance that are not counteracted by the vibration isolation system, because the STM feedback, which is faster than most vibrations, is always on. This also prevents unwanted manipulations, allowing a very fast (up to 1 manipulation per second) and reliable manipulation protocol.

The scope of the manipulation control becomes clear in Chapter 3, where the procedure is automated to construct a 1 kB memory with 1 atom per bit. An image recognition program determines the precise locations of the vacancies in the grid of Cl atoms by looking at the apparent height of all pixels in a standardised image frame. Each vacancy is then matched to a specific destination, with a path-finding algorithm connecting initial and destination coordinates such that the individual paths don't interfere. Next, the program instructs the STM to move the vacancies into the desired structure. In eight-byte blocks, the data storage is built up, forming a full kilobyte in a $\sim 100 \times 100$ nm^2 area. Due to occasional defects on the surface, some of these blocks need to be avoided to prevent damage to the tip, or are otherwise unsuitable for functioning bits. Each block therefore has a 5 × 5 marker on one corner, to be able to differentiate between regular blocks, 'broken' blocks, and beginning or end of line markers, to aid in automatic nav-

igation of the memory. After the data storage has been constructed, the entire text can be read and rewritten automatically using these markers, in approximately an hour. The information density of the more than sixty thousand atoms, positioned precisely at their intended locations, thus reaches 502 terabits per square inch, or 0.778 bits/nm^2.

Vacancies appear as depressions when imaging the apparent height of the surface. When taking a dI/dV spectrum, there is also a difference between vacancy and chlorine background. A localised electronic vacancy state is observed at an energy that is slightly below the onset of the copper chloride conduction band, which is at 3.5 V. In Chapter 4, we constructed various one- and two-dimensional periodic structures of vacancies, to measure the electronic behaviour when vacancies are coupled together. In the centre of one-dimensional chains, the onset of the band moves to lower energy as the length of the chain goes up. This effect is stronger when the vacancies are positioned closer to each other than for bigger separations. However, for all spacings, the maximum shift in the band onset is reached for chains longer than eight vacancies, thus giving an indication for the extent of the coupling, as described by the tight-binding model. We also constructed artificial crystals in two dimensions in various sizes and vacancy densities. Here, a similar shift of the band onset is observed as for the one-dimensional chains, saturating at sizes 8 × 8 or above. The shift is largest for the structures with highest density and smallest for the crystals with bigger spacings.

Maps of the local density of states (LDOS) are reconstructed from dz/dV measurements, because the arrangements are too delicate for regular dI/dV spectroscopy, which can reach multiple nA's at 5 V. In LDOS maps taken on the most dense structures (50 % and 33 % vacancies), we observe a standing wave pattern at certain energies, with higher modes at higher voltages. Taking the 2D Fourier transform of these images allows us to calculate the wave vector of the quasi-particle Bloch waves and thus the dispersion. For both densities, these Bloch waves are exhibited in crystals of different orientations (straight, 45° rotated) and different sizes, each time leading to the same dispersion relation. By fitting simulations of a tight-binding model with coupling to the electron bath to these measurements, we find a lower effective electron mass for the stripes lattice than for the checkerboard lattice. This means that by engineering structures at the atomic level with different densities, it is possible to tune electronic properties such as the dispersion, thus providing a testing ground for future designer materials.

In Chapter 5, the tight-binding coupling between vacancies is further explored, as well as the dependence on the spacing between vacancies. We made structures where the geometry and coupling of the individual vacancies resemble that of acene molecules, a class of molecules consisting of chains of benzene rings. We perform scanning tunnelling spectroscopy on these 'artificial molecules' in order to find the band structure, and the closing and opening of the optical gap as a function of the chain length, as was predicted before. Tight-binding simulations lead to a quantitative comparison with measurements on three different configurations with increasing coupling strength. The effect, however, is not found, as it is thought to lie beneath our detection limit.

In Chapter 6, we investigate the occurrence of resonances in STS measurements on the copper chloride surface, which sometimes leads to negative differential conductance. These resonances shift in energy when the needle is placed over vacancies or when the tip height is adjusted, via the set-point current. We explain this by a quantum

dot – possibly a Cl atom – that is weakly connected to the apex of our STM tip, where the resonant energy levels shift due to the experienced electric field. The applied electric field is dependent on tip-sample distance and the local charge distribution of the surface. In order to investigate the dependence on geometry, we made various vacancy structures, such as square patches of copper where enough vacancies have been clustered to show the bare copper. With a simulation of the local electric field in various geometries, a qualitative understanding is reached, even suggesting some values for the precise location of the quantum dot – or sometimes multiple dots – on the tip apex. Adjusting these simulations to our measurements suggests that it might be possible to reconstruct the actual charge distribution of a surface. This would mean that after calibrating the quantum dot to a known surface, this method might be used to probe the local electric field distribution of unknown structures.

After manipulating atoms within the $Cu_2Cl/Cu(100)$ monolayer, we investigate the behaviour of adatoms on top of the copper chloride, which acts as a thin insulating layer. On Cu_2N, a very similar substrate, magnetic spin excitations were observed with several transition metal atoms, due to the decoupling layer. In Chapter 7, we deposited single iron, silver and nickel adatoms, and study the local geometry, i.e. where the adatoms bond to the substrate, and if we can observe inelastic tunnelling excitations in their differential conductance spectra. There are four possible lattice sites for an adatom to adsorb on: the *bridge*, *hollow*, and *on-top* positions on a fully chlorinated substrate, or on top of a chlorine vacancy. We used atom manipulation to prove that some silver atoms lie on vacancies, and this rudimentary manipulation procedure suggests that it should be possible to develop a reliable vertical and horizontal adatom manipulation technique, just like on similar substrates. Iron adatoms on hollow positions show small steps in the differential conductance spectrum, around the expected energy for magnetic spin excitations. These steps seem to shift slightly when measured in externally applied magnetic fields of up to 9 T in the out-of-plane direction. This suggests that Fe on Cu_2Cl might indeed be magnetic, although more research with stronger tools is needed to verify this hypothesis. If adatoms on the copper chloride surface turn out to behave magnetically, it becomes interesting to combine this with the vacancy manipulation techniques that we have shown earlier, providing a new template for future engineering on the atomic scale.

SAMENVATTING

In dit proefschrift wordt een techniek ontwikkeld om met grote precisie en op een grote schaal individuele atomen op een ionisch oppervlak te manipuleren, om zo de quantummechanische eigenschappen van atomaire samenstellingen op de nanoschaal te bestuderen. De rastertunnelmicroscoop, of *scanning tunnelling microscope* (STM), is de machine die dit voor ons mogelijk maakt, waarbij de scannende beweging van een ultradunne naald over een atomair vlak oppervlak ons de mogelijkheid geeft de enkele atomen te observeren die de structuren in ons oppervlak vormen, door gebruik te maken van de tunnelstroom tussen tip en sample. Door de aangelegde spanning te variëren en de tunnelstroom te meten is het mogelijk de lokale toestandsdichtheid (LDOS) te bepalen, die ons informatie geeft over de elektronische toestanden op de positie van de naald. Deze krachtige methode heet rastertunnelspectroscopie, ofwel *scanning tunnelling spectroscopy* (STS).

Om atomen te manipuleren, hebben we een met chlooratomen bedekt koperoppervlak gebruikt. Door Cu_2Cl-poeder, een zout, op te dampen op een schoon, atomair vlak Cu(100)-kristal, binden de chlooratomen ionisch met de koperatomen, waarbij ze een vierkante c(2 × 2)R45°-reconstructie vormen, die we hier aangeven als het Cu_2Cl-oppervlak. Wanneer er onvoldoende materiaal is opgedampt om een volledige monolaag van chloor te vormen, tonen de ontbrekende chlooratomen zich als enkele defecten in de Cu_2Cl/Cu(100)-laag: vierkante indeukingen van ogenschijnlijk 20-50 pm diep die we *vacancies* noemen. De vacancydichtheid na preparatie van het oppervlak kan aangepast worden door de opdamptijd te variëren.

Als we een vacancy benaderen met de tip van de STM naald, zodanig dat de tunnelstroom oploopt tot in de μA's, kan een naburig Cl-atoom overspringen naar de positie van de vacancy, waardoor de vacancy effectief in de tegengestelde richting beweegt. In Hoofdstuk 2 wordt de methode om vacancies nauwkeurig te manipuleren ontwikkeld: door de tiphoogte te beheersen met behulp van feedback op de stroom en de tip een klein beetje asymmetrisch te positioneren tussen vacancy en naburig Cl-atoom kunnen nauwkeurigheden van soms meer dan 99 % bereikt worden. Deze techniek is ongevoelig voor kleine variaties in de tip-sample-afstand die niet tegengegaan worden door de vibratieïsolatie, omdat de STM-feedback, die sneller is dan de meeste vibraties, altijd aan staat. Dit voorkomt ook ongewenste manipulaties, zodat een zeer snel (tot wel 1 manipulatie per seconde) en betrouwbaar manipulatieprotocol ontstaat.

De omvang van onze beheersing van het manipuleren van vacancies wordt duidelijk in Hoofdstuk 3, waar de procedure geautomatiseerd is om een geheugen van 1 kB met 1 atoom per bit te construeren. Een beeldherkenningsprogramma bepaalt de precieze locaties van alle vacancies in een rooster van Cl-atomen door te kijken naar de ogenschijnlijke hoogte van alle pixels in een gestandaardiseerd beeldvenster. Elke vacancy wordt vervolgens gekoppeld aan een specifieke bestemming, waarna een *path-finding*-algoritme de begin- en eindcoördinaten verbindt, zodanig dat de individuele

paden niet interfereren. Het programma instrueert de STM vervolgens om de gewenste structuur te bouwen. De dataopslag wordt in blokken van acht bytes opgebouwd, zodat een volledige kilobyte binnen een oppervlak van $\sim 100 \times 100$ nm^2 past. Als gevolg van incidentele defecten op het oppervlak moeten sommige van deze blokken vermeden worden om schade aan de tip te voorkomen, of zijn anderszins niet geschikt om functionele bits op te plaatsen. Elk blok heeft daarom een 5×5 markering op één hoek, om het verschil te kunnen maken tussen reguliere blokken, 'kapotte' blokken, en regeleindes en -beginmarkeringen, zodat door het geheugen automatisch genavigeerd kan worden. Nadat de dataopslag gebouwd is, kan de gehele tekst automatisch gelezen en herschreven worden met behulp van deze markeringen, in ongeveer een uur. De informatiedichtheid van de meer dan zestigduizend atomen, die precies op hun bestemde plaatsen zijn gepositioneerd, haalt daarom 502 terabits per vierkante inch, oftewel 0,778 bits/nm^2.

Wanneer slechts de schijnbare hoogte van het oppervlak wordt bekeken, zien vacancies eruit als inkepingen in de koperchlorideachtergrond, maar er is ook een verschil tussen vacancy en de achtergrond wanneer een $\mathrm{d}I/\mathrm{d}V$-spectrum wordt genomen. Een gelokaliseerde elektronische vacancytoestand kan worden waargenomen op net iets lagere energie dan het begin van de geleidingsband van koperchloride, die op 3.5 V is. In Hoofdstuk 4 hebben we één- en tweedimensionale periodieke structuren van vacancies geconstrueerd, om het elektronisch gedrag te meten wanneer vacancies aan elkaar gekoppeld worden. In het midden van ééndimensionale ketens beweegt het begin van de band naar lagere energie voor grotere lengtes. Dit effect is sterker als de vacancies dichter bij elkaar gepositioneerd zijn dan voor grotere afstanden. Echter, voor alle verschillende relatieve afstanden wordt de maximumverschuiving bereikt bij ketens vanaf acht vacancies lang, wat hiermee een indicatie voor de reikwijdte van de koppeling geeft, zoals beschreven door het *tight-binding model*. We hebben ook kunstmatige kristallen gemaakt in twee dimensies, in verschillende groottes en vacancydichtheden. Hier zien we een vergelijkbare verschuiving van het begin van de band, die verzadigt bij afmetingen groter dan 8×8. De verschuiving is het grootst voor structuren met de hoogste dichtheid en het kleinst voor de kristallen met grotere onderlinge afstanden.

We hebben kaarten van de lokale toestandsdichtheid (LDOS) gereconstrueerd uit $\mathrm{d}z/\mathrm{d}V$-metingen, omdat de structuurtjes te gevoelig zijn voor reguliere $\mathrm{d}I/\mathrm{d}V$-spectroscopie (die op 5 V meerdere nA's kan bereiken). In de LDOS-kaarten van de dichtste structuren (50 % en 33 % vacancies) zien we op bepaalde energieën een patroon van staande golven, met hogere modi op hogere spanningen. Het uitvoeren van een 2D-Fouriertransformatie zorgt ervoor dat we het golfgetal van de Bloch-golven van quasideeltjes kunnen uitrekenen, en dus de dispersie kunnen bepalen. Voor beide dichtheden zien we deze Bloch-golven in kristallen van verschillende oriëntaties (recht, 45° gedraaid) en groottes, met elke keer eenzelfde dispersierelatie. Door simulaties van een *tight-binding model* met koppeling naar het elektronenbad aan deze metingen aan te passen, vinden we een lagere effectieve elektronmassa voor het gestreepte rooster dan voor het schaakbordrooster. Dit betekent dat het mogelijk is elektronische eigenschappen zoals de dispersie af te stemmen door structuren op het atomaire niveau te bouwen met verschillende dichtheden, wat hiermee een nieuw testoppervlak biedt voor toekomstige ontwerpbare materialen.

In Hoofdstuk 5 verkennen we nader de *tight-binding*-koppeling tussen vacancies en hoe dit precies afhankelijk is van de onderlinge afstand. We hebben structuren gemaakt waarbij de geometrie en onderlinge koppeling lijken op die van aceenmoleculen, een groep moleculen die bestaan uit ketens van benzeenringen. We voeren rastertunnelspectroscopie uit op deze 'kunstmatige moleculen' om de bandenstructuur te vinden, evenals het openen en sluiten van de optische *band gap* dat hiervoor voorspeld is. *Tight-binding*-simulaties leiden tot een kwantitatieve vergelijking met metingen aan drie verschillende configuraties met toenemende koppelsterkte. Het effect wordt echter niet gevonden, aangezien het waarschijnlijk onder onze detectielimieten ligt.

In Hoofdstuk 6 onderzoeken we het voorkomen van resonanties in spectroscopiemetingen op het koperchlorideoppervlak, die soms leiden tot een negatieve differentiële geleiding. Deze resonanties verschuiven in energie wanneer de naald boven vacancies is gepositioneerd, of wanneer de tiphoogte aangepast wordt door middel van de richtwaarde voor de stroom. We verklaren dit door een *quantum dot* – mogelijk een chlooratoom – die zwak verbonden is met het uiterste puntje van de STM-naald, waar de resonante energieniveaus verschuiven door het ondervonden elektrische veld. Het aangebrachte elektrische veld is afhankelijk van de tip-sample-afstand en de lokale ladingsverdeling op het oppervlak. Om te onderzoeken in hoeverre deze resonanties afhankelijk zijn van de geometrie, hebben we verschillende vacancystructuren gemaakt, zoals vierkante stukken koper waar genoeg vacancies bijeen vergaard zijn om het kale koper te laten zien. Met een simulatie van het lokale elektrische veld in deze verschillende geometrieën kunnen we een kwalitatief inzicht bereiken, waarbij zelfs een aantal precieze waarden worden gesuggereerd voor de posities van de quantum dot – of soms meerdere dots – op de punt van de naald. Het aanpassen van deze simulaties aan onze metingen suggereert dat het mogelijk zou kunnen zijn om de daadwerkelijke ladingsverdeling op een oppervlak te reconstrueren. Dit betekent dat na kalibratie van de quantum dot aan een bekend oppervlak, deze methode gebruikt zou kunnen worden om de verdeling van het lokale elektrische veld van onbekende structuren af te tasten.

Nadat de atomen binnenin de Cu_2Cl/Cu(100)-monolaag zijn gemanipuleerd, onderzoeken we het gedrag van adatomen bovenop het koperchloride, dat zich gedraagt als een dunne isolerende laag. Op Cu_2N, een zeer vergelijkbaar substraat, werden magnetischespinexcitaties geobserveerd bij verscheidene atomen van overgangsmetalen, dankzij de ontkoppelende laag. In Hoofdstuk 7 hebben we enkele ijzer-, zilver- en nikkelatomen neergelegd op het oppervlak en bestuderen we de lokale geometrie, d.w.z. waar de adatomen aan het substraat binden, en of we inelastische tunnelexcitaties kunnen waarnemen in hun geleidingsspectra. Er zijn vier mogelijke roosterposities voor een adatoom om op te adsorberen: de *brug-*, *holte-*, en bovenop-posities op een volledig gechlorineerd substraat, of bovenop een chloor-vacancy. We gebruiken atoommanipulatie om aan te tonen dat sommige zilveratomen op vacancies liggen, en deze rudimentaire manipulatieprocedure suggereert dat het mogelijk zou moeten zijn om een betrouwbare verticale en horizontale adatoommanipulatietechniek te ontwikkelen, net zoals op vergelijkbare substraten al mogelijk is. IJzeradatomen op holte-posities laten kleine stappen zien in de spectra van de afgeleide geleiding, rondom de verwachte energie voor magnetischespinexcitaties. Deze stappen lijken een beetje te verschuiven wanneer het spectrum gemeten wordt in een extern aangebracht magnetisch veld van tot 9 T in de

loodrechte richting. Dit suggereert dat Fe op Cu_2Cl inderdaad magnetisch zou kunnen zijn, alhoewel meer onderzoek met betere middelen nodig is om deze hypothese te bevestigen. Als adatomen op het koperchlorideoppervlak zich magnetisch blijken te gedragen, wordt het interessant om dit te combineren met de eerder getoonde vacancy-manipulatietechnieken, waarmee dit een nieuw sjabloon kan worden voor toekomstige bouwwerken op de atomaire schaal.

Curriculum Vitæ

Floris Eduard Kalff

28-08-1989 Born in 's-Gravenhage, The Netherlands.

Education

2001–2007 Secondary school, gymnasium
Christelijk Gymnasium 'Sorghvliet', 's-Gravenhage, The Netherlands

2007–2011 Bachelor of Science (BSc) in Physics
Universiteit Leiden, The Netherlands

2011–2013 Master of Science (MSc) in Experimental Physics
Universiteit Leiden, The Netherlands
Thesis: Monolithic Magnetic Resonance Force Microscopy at low temperatures
Supervisor: Prof. dr. ir. T.H. Oosterkamp

2013 Internship
cosine Research BV, Leiden, The Netherlands

2014–2018 Doctorate (PhD) in Applied Physics
Kavli Institute of Nanoscience, Technische Universiteit Delft, The Netherlands
Thesis: Large-scale atom manipulation on an ionic surface and its prospects
Promotors: Prof. dr. A.F. Otte and prof. dr. ir. H.S.J. van der Zant

List of Publications

Publications

3. J. Girovsky, J. L. Lado, **F. E. Kalff**, E. Fahrenfort, L. J. J. M. Peters, J. Fernández-Rossier and A. F. Otte, *Emergence of quasiparticle Bloch states in artificial crystals crafted atom-by-atom*, SciPost Physics **2**, 020 (2017).

2. J. M. de Voogd, M. A. van Spronsen, **F. E. Kalff** , B. Bryant, O. Ostojić, A. M. J. den Haan, I. M. N. Groot, T. H. Oosterkamp, A. F. Otte, M. J. Rost, *Fast and reliable pre-approach for scanning probe microscopes based on tip-sample capacitance*, Ultramicroscopy **181**, 61-69 (2017).

1. **F. E. Kalff**, M. P. Rebergen, E. Fahrenfort, J. Girovsky, R. Toskovic, J. L. Lado, J. Fernández-Rossier and A. F. Otte, *A kilobyte rewritable atomic memory*, Nature Nanotechnology **11**, 926-929 (2016).

Patents

1. **F. E. Kalff**, M. P. Rebergen, E. Fahrenfort, J. Girovsky, R. Toskovic, and A. F. Otte, *Atomic scale data storage device by means of atomic vacancy manipulation*, Dutch patent application NL2016335, US patent application 16/080,990.

ACKNOWLEDGEMENTS

First of all, I would like to thank both my promotors and the members of the doctoral committee for taking the time and effort to read my thesis and propositions. It is an honour to have you on my committee.

I would like to thank our scientific collaborators, José Lado and Joaquín Fernández-Rossier from Braga, Portugal, for great discussions, but even greater simulations and calculations on the various vacancy configurations interspersed throughout this thesis. My thanks also goes to Peter Schmittekert and Ferdinand Evers from Regensburg, Germany for the inspiration and discussions on the expected behaviour in polyacenes.

To Sander, as my daily supervisor, I owe the most gratitude, for leading the way in this fascinating world at the nanoscale. I've learned a great deal, and enjoyed a lot being part of your group, as well as the great discussions, outings and Belvedèreborrels. Thank you for the great scientific discussions, often providing new insights and new directions. Your enthusiasm is very contagious, and I'm glad you granted me the wonderful opportunity to move atoms around on a daily basis. You created an inspiring atmosphere, with a close group that has had a lot of fun together. Sander, I wish you great success as a full professor with a growing lab, and I am confident the science will continue to be awesome!

Setting up an entire new lab, with a brand-new machine, was a great learning experience. Getting to know all details and gradually getting it to work was a very instructive enterprise where Ben's experience and instructions taught me a lot. Ben, thanks for explaining and teaching all the ins and outs of laboratory work, the detailed workings of the STM itself and the many strict procedures surrounding it; for your good sense of humour and your company in the first two years of my PhD. I wish you good luck with your career in Nijmegen and the SPM world!

The other great mentor I had, when starting in Delft more than four years ago, was Anna. As the senior PhD candidate, it was great having you as an example in the lab, and you were the one guiding me through my first atom manipulations! Even though we did not work together much, I enjoyed the many laughs and conversations at drinks and coffee times.

Ranko, together we started out on this adventure called a PhD, and (almost) together, we bring it to completion. Doubling the Otte-lab in size from the first day that we started, it was great having someone to share thoughts with in the same phase of the PhD, especially as we started out in the same office[1]. Ever the one in 'the other lab'[2], I could always rely on you for help – as a true Master of the Valve! I've enjoyed our many trips to conferences, your distinct sense of humour and the healthy doses of Dutch complaining. Thanks for taking on the glorious task of being my paranymph!

[1] This, however, was not meant to last for long.
[2] In this sense our progress truly was parallel.

Then on to the Otte-lab members that came after me, some of whom I had to train a little, but of whom I learned much as well. With Jan, I spent the most time: many hours in the lab, but also in the various conferences and the trips to Switzerland. We've had much fun experimenting and building things in the lab; I'm impressed by your drive at understanding things thoroughly, and asking keen questions. Thanks for the many amusing times, and I wish you and Zuzana good luck in England and with the rest of your career.

With David I spent a lot of time in the last part of my PhD, and I will certainly remember you as being very driven and innovative. You led some great progress in the lab, from the tinkering with solder and dremels[3], to the rapid building of many atomic structures. Thank you for the many great discussions and new insights, the uplifting encouragements and other fun times!

Mari joined us just in time to attend my wedding, thank you for being there! It was fun working with you, and thanks – as first of a wave of new Spanish influences – for the many great chats during coffees and borrels! To Jérémie the task of acting as senior PhD candidate, passing on the knowledge of the lab. You're already doing great things, and I wish you good luck with the last year of your thesis! Willeke and Robbie, it was great working with you both, for the brief time we were in the lab together. We had many fun times together and I wish you good luck in the rest of your careers!

A special thanks to all the students that I supervised. Nora, thanks for your quick wit and hard work in the many hours that we spent building kilobytes. Good luck in your future career at TNO! Marnix, thank you for the sharp thinking and clever solutions for complex problems. Hans, it was fun to have you around in the lab, building many different structures. I am sure you will find a good career that combines your two degrees. Thomas, Lucas, and Laurien, thank you for the brief but productive time in the Otte-Lab. To Lucinda, Marjolein, Bruno, Mitchel, Shang-Jen and the many other students that I did not formally supervise, but got to meet anyway: it was fun crossing paths with you.

A lot of my research would not have been possible without the technical support of Mascha and Tino. Thank you a lot for helping with the installation of the new lab, and the many technical challenges afterwards! A special thanks also to Maria, Erika, Etty, Dorine, for the administrative support, crucial at several occasions.

In my first office on the third floor – back when it was still MED – I initially shared the room with Ranko, Nandini and Giordano, and eventually Anastasia. It was great sharing an office with you and having the many conversations that make an office worthwhile to visit[4]. Later on, when MED merged into QN, I transferred to the first floor, where David, Clemens and Irina became my office-mates. In this office, I spent a larger portion of my time, and I would like to thank you as well for the pleasant times in the office.

The other people in the department I would like to thank as well, from the close group of MED researchers to the larger QN department, thank you all for the fun times at the Real Italian Coffee Machine, the borrels and other hallway encounters! Giordano, thanks for the great dancing parties and fun office gags. Santiago, thanks for your quick wit and enthusiastic nature. Nandini, thanks for the many intense and fun conversations! Rocco, please keep inspiring people. Dejan, always remember your style. Ignacio,

[3] Not at the same time, luckily.
[4] A rare event for me, as I spent most of my time down in the dungeons.

thanks for your cheerful presence! Vera, thanks for being my fellow Leiden influence in the barbarous lands down south. Emre, Max, Michele, Riccardo, Joshua, Mickael, Alexandra, Ben S., Ronald, Anastasia, Shun, Sal, and the others, thank you for being part of the now seemingly ancient, but not forgotten MED-community. To Mafalda, Dirk, João, Davide, Joeri, Nikos, Robin, Nicola, Miguel, Luigi, Holger, Matvey, Richard, Andreas, Dima, Felix, Yildiz, Igor, Maarten, Martijn, Thierry, Sabina, Marios, Iacopo, Moritz, Daniel, Jorrit, Mario, Mark, Ines, and the many others, it was fun meeting you in QN, and I wish you all good luck in your future. Thanks also to all the PI's, Kobus, Herre, Gary, Andrea, Peter, Simon, Sonia, Toeno, Teun, Gao, who essentially make the department what it is; I wish you good luck in all the interesting and promising research going on!

Marije, many thanks to you for your tireless coordination of all Casimir events, and – with Tjerk – the encouragement of us in the PhD platform. Bob, Julia, Orkide, Gesa, Elena, Sarah, Marios, Koen, and Kirsten, it was great getting to know you, organising and participating in the various social meetings and events together!

I would like to thank my many musical friends, from the Residentie Bachkoor, Sempre Crescendo and the various smaller ensembles with dubious names, for keeping me sane throughout these four years. A bimonthly dose of Bach is strongly recommended for a healthy state of mind, and a bit of polyphony really keeps the focus alive.

Thanks also to my new colleagues at TNO, for supporting me in the first months on the new job, while I was still finishing up the thesis. Hope to have more time for you now!

Verder nog veel dank aan mijn clubgenoten en andere Leidse vrienden, die oogluikend toestonden dat ik naar Delft vertrok (louter onder het mom van een beschavingsoffensief) en me daar zelfs in steunden. Dank aan ons bruidspersoneel, uiteraard voor de hulp in de organisatie, maar vooral ook voor de gezelligheid vooraf en de vele (gastronomisch verantwoorde) reünies en zomerborrels nadien.

Dank aan mijn leraren van het Sorghvliet, voor de inspiratie tijdens mijn schooltijd, maar ook voor het enthousiasme en de aansporing tijdens mijn studie- en promotietijd. Bernard, dank voor je tomeloze enthousiasme en de vele lange gesprekken over brede onderwerpen met diepe inzichten.

Aan mijn paranimfen, Ranko en Sierk, ook (alvast) veel dank, voor jullie steun de afgelopen jaren en het op jullie nemen van deze belangrijke taak!

Veel dank aan mijn familie en schoonfamilie, voor de brede steun, interesse, en soms zelfs enthousiasme, als ik mooie plaatjes kon laten zien. Lieve grootouders, veel dank voor jullie inspiratie en motivatie, vele goede gesprekken en jullie grootse vertrouwen in mijn toekomst. Helianne, Eveline en Leander, dank voor het geduldig tolereren van zoveel natuurkunde thuis, ik kan alleen helaas niet garanderen dat het veel minder zal worden. Heli, heel veel dank voor je hulp in het ontwerpen van de kaft! Papa en mama, veel dank natuurlijk voor hoe jullie mij groot hebben gebracht, dit maakt mij tot wie ik ben. Maar vooral veel dank voor alle steun tijdens mijn studie en promotie, ik kon altijd op jullie rekenen voor een luisterend oor en wijze raad; jullie enthousiasme en grote vertrouwen hebben mij zeer gesterkt. Tot slot, Mara, het zijn een bewogen viereneenhalf jaar geweest, ik ben blij dat ik die met jou heb mogen delen.

Finally, a word of thanks to the reader, who came this far to witness the end of an era. *Hora est.*

Den Haag, september 2018.